UNIVERSIDADE TECNOLÓGICA FEDERAL DO PARANÁ
PROGRAMA DE PÓS-GRADUAÇÃO EM ENGENHARIA CIVIL

ARY VINICIUS NERVIS FRIGERI

SENSITIVITY AND FRAGILITY ANALYSIS OF A RAILWAY TEMPERATURE PREDICTION MODEL

PATO BRANCO

2026

ARY VINICIUS NERVIS FRIGERI

SENSITIVITY AND FRAGILITY ANALYSIS OF A RAILWAY TEMPERATURE PREDICTION MODEL

Análise de sensibilidade e fragilidade de um modelo de predição de temperatura de trilhos ferroviários

Dissertação apresentada ao Programa de Pós-Graduação em Engenharia Civil da Universidade Tecnológica Federal do Paraná como requisito parcial à obtenção do grau de Mestre em Engenharia Civil.

Área de Concentração: Materiais e Engenharia de Estruturas

Orientador(a): Profª. Drª. Rúbia Mara Bosse

Coorientador(a): Prof. Dr. Paulo Piloto

PATO BRANCO

2026

Ministério da Educação
Universidade Tecnológica Federal do Paraná
Campus Pato Branco

UTFPR
UNIVERSIDADE TECNOLÓGICA FEDERAL DO PARANÁ

ARY VINICIUS NERVIS FRIGERI

SENSITIVITY AND FRAGILITY ANALYSIS OF A RAILWAY TEMPERATURE PREDICTION MODEL

Trabalho de pesquisa de mestrado apresentado como requisito para obtenção do título de Mestre Em Engenharia Civil da Universidade Tecnológica Federal do Paraná (UTFPR). Área de concentração: Materiais E Engenharia De Estruturas.

Data de aprovação: 01 de Abril de 2026

Dra. Rubia Mara Bosse, Doutorado - Universidade Tecnológica Federal do Paraná

Dr. Henrique Machado Kroetz, Doutorado - Universidade Federal do Paraná (Ufpr)

Dr. Paulo Piloto, Doutorado - Instituto Politécnico de Bragança

Dr. Paulo Rogerio Novak, Doutorado - Universidade Tecnológica Federal do Paraná

Documento gerado pelo Sistema Acadêmico da UTFPR a partir dos dados da Ata de Defesa em 27/05/2026.

ACKNOWLEDGEMENTS

This work is the result of the interaction and collaboration of many institutions and people. First, I thank Federal University of Technology (UTFPR), campus Guarapuava, which made this double degree program with the Polythecnic University of Bragança (IPB) possible in the first place. Both institutions provided me with great support and the environment, including tools and human resources, to make this work possible.

I thank my advisors, Professors PhD. Rubia Bosse, PhD. Manuel Minhoto, PhD. Paulo Piloto, and Msc. Dyorgge Alves, for helping me along the academic path and providing meaningful insights and guidance.

I thank my parents, Ivandra and Ari, and my sister Alicia, for always being there to help and support me during all my years of study. Thank you for always helping me overcome challenges and make decisions. Thank you also for understanding all the comings and goings and the distance. Nothing would have been possible without you. I also thank my wife Mariana for being by my side during and after graduation, giving me the necessary support to complete this work. Your support was essential during this time. I also thank all my friends who took part in this journey.

ABSTRACT

Rail temperature prediction is essential for railway safety, as extreme temperatures can lead to track buckling and structural instability. This study presents a comprehensive sensitivity analysis and probabilistic assessment of a validated physical rail temperature model implemented in MATLAB and integrated with the UQLab framework. Two sensitivity analysis approaches were employed: a global analysis treating all parameters as random variables, and a data-informed analysis using field measurements for weather variables. Results identify the convection coefficient as the most influential parameter when all variables are uncertain, while the solar absorption coefficient and area become critical when weather parameters are measured. Material properties such as density, specific heat, and volume exhibit negligible influence on predictions. Monte Carlo simulations comprising over 3.3 million scenarios were conducted for reliability assessment to calculate the probabilities of rail temperatures exceeding critical thresholds based on ambient air temperatures. Two approaches were employed: a hybrid approach using measured weather data and a synthetic approach with statistically generated weather scenarios. The synthetic approach enables probability estimation for extreme conditions beyond the measured dataset. Literature indicates that rail thermal buckling may occur at temperatures around $55\,^{\circ}$C to $60\,^{\circ}$C under certain track conditions. At $40\,^{\circ}$C ambient temperature, the synthetic approach estimates $10\,\%$ and $0.6\,\%$ probabilities for rail temperatures reaching or exceeding $55\,^{\circ}$C and $60\,^{\circ}$C, respectively, while the hybrid approach yields $51\,\%$ and approximately $0.6\,\%$ for the same thresholds. This discrepancy highlights the importance of comprehensive scenario coverage for robust probability estimation.

Keywords: railway; thermal buckling; monte carlo; sensitivity analysis; reliability analysis.

RESUMO

A previsão da temperatura do trilho é essencial para a segurança ferroviária, uma vez que temperaturas extremas podem levar à flambagem da via e instabilidade estrutural. Este estudo apresenta uma análise de sensibilidade abrangente e avaliação probabilística de um modelo físico validado de temperatura de trilho implementado em MATLAB e integrado com o framework UQLab. Duas abordagens de análise de sensibilidade foram empregadas: uma análise global tratando todos os parâmetros como variáveis aleatórias, e uma análise informada por dados usando medições de campo para variáveis meteorológicas. Os resultados identificam o coeficiente de convecção como o parâmetro mais influente quando todas as variáveis são incertas, enquanto o coeficiente de absorção solar e a área tornam-se críticos quando os parâmetros meteorológicos são medidos. Propriedades do material como densidade, calor específico e volume exibem influência negligenciável nas previsões. Simulações de Monte Carlo compreendendo mais de 3,3 milhões de cenários foram conduzidas para avaliação de confiabilidade para calcular as probabilidades de temperaturas do trilho excederem limites críticos com base nas temperaturas do ar ambiente. Duas abordagens foram empregadas: uma abordagem híbrida usando dados meteorológicos medidos e uma abordagem sintética com cenários meteorológicos gerados estatisticamente. A abordagem sintética permite a estimativa de probabilidade para condições extremas além do conjunto de dados medidos. A literatura indica que a flambagem térmica da via ocorrer a temperaturas em torno de $55\,^{\circ}$C a $60\,^{\circ}$C sob certas condições. A $40\,^{\circ}$C de temperatura ambiente, a abordagem sintética estima $10\,\%$ e $0.6\,\%$ de probabilidades para temperaturas do trilho atingindo ou excedendo $55\,^{\circ}$C e $60\,^{\circ}$C, respectivamente, enquanto a abordagem híbrida produz $51\,\%$ e aproximadamente $0.6\,\%$ para os mesmos limites. Esta discrepância destaca a importância da cobertura abrangente de cenários para estimativa robusta de probabilidade.

Palavras-chave: ferrovias; encurvadora térmica; monte carlo; análise de sensibilidade; análise de confiabilidade.

ILLUSTRATIONS LIST

Figure 1 – Railway cross-section 16
Figure 2 – Railway profiles 17
Figure 3 – Example of concrete sleepers 19
Figure 4 – Rigid fastening 19
Figure 5 – Elastic Pandrol fastening 20
Figure 6 – Fishplate joint 21
Figure 7 – Representative temperature measurement point 23
Figure 8 – Esveld correlations for air and rail temperatures 24
Figure 9 – Chapman's collected data 25
Figure 10 – Chapman's simplified rail geometry for heat transfer analysis 27
Figure 11 – Collected weather data and predicted rail temperatures using Zhang's model 30
Figure 12 – Improvements proposed by the CNU model 31
Figure 13 – *railtemp* package validation against FEM 32
Figure 14 – Lateral buckling examples 34
Figure 15 – Typical track response curve 35
Figure 16 – Typical track model for buckling analysis 36
Figure 17 – Fastener linear model 36
Figure 18 – Sleeper-ballast behavior 37
Figure 19 – Track misalignment 37
Figure 20 – Lim, Park and Kang (2003) cross-section model 38
Figure 21 – Ballast lateral and longitudinal behavior utilized by Lim, Park and Kang (2003) 38
Figure 22 – Variation of thermal buckling temperature 39
Figure 23 – Probability density of continuous variables 43
Figure 24 – Scheme of a device corresponding to Equation 23 44
Figure 25 – Reliability limit states and regions 46
Figure 26 – Methodology overview 48
Figure 27 – Validation results for single step solutions 55
Figure 28 – Validation results for continuous validation (single day) solutions 55
Figure 29 – Input parameter distributions used in the modeled sensitivity analysis 57
Figure 30 – Morris elementary analysis for **"w/ measured data"** 58
Figure 31 – Sobol sensitivity analysis results 58
Figure 32 – Extended class diagram for *railtemp* package 62
Figure 33 – Remote and local clusters diagram 65
Figure 34 – Fragility data for hybrid Monte Carlo approach 67
Figure 35 – Count of simulations for given T_{air}bins 68
Figure 36 – Sample of simulated and field measured values of rail temperatures for hybrid Monte Carlo approach 68
Figure 37 – Generated and measured ambient temperature distribution by month 70
Figure 38 – Generated and measured wind speed distribution by month 70
Figure 39 – Generated and measured solar radiation distribution by month 70
Figure 40 – Time series of generated and measured weather parameters for August 71
Figure 41 – Fragility curves for synthetic Monte Carlo approach 73
Figure 42 – Daily aggregated distribution of maximum simulated rail temperatures (T_{rail}) for different ambient temperature (T_{air}) thresholds. 74
Figure 43 – Count of simulations for given T_{air} bins 74
Figure 44 – Time series example of measured and scenario variations of simulated rail temperatures 75

Figure 45 – Boxplot of simulated and measured air and rail temperatures 76
Figure 46 – Generated and measured ambient temperature distribution by month. 86
Figure 47 – Generated and measured wind speed distribution by month. 87
Figure 48 – Generated and measured solar radiation distribution by month. 88
Figure 49 – Box plot of the generated and measured data for ambient temperature by month and 15-min intervals. 90

LIST OF TABLES

Table 1 – Railway gauges in some European countries 18
Table 2 – Comparison between rigid and elastic fastenings 20
Table 3 – Comparison between Jointed Track and Continuous Welded Rail (CWR) 22
Table 4 – Chapman's model sensitivity result 28
Table 5 – Statistical results for different models 31
Table 6 – Comparison of empirical and physical rail temperature models 33
Table 7 – Fastenings torsional resistance 36
Table 8 – Summary of input parameters for UQLab 50
Table 9 – Modelled parameters distributions for UQLab 56
Table 10 – Benchmark of Monte Carlo simulation on different cluster configurations 66
Table 11 – Expected duration (hours) of given simulation count for different set configurations 66
Table 12 – Summary of Monte Carlo simulations scenarios generation 72

LIST OF SOURCE CODE

Source Code 1 – Example of a UQLab input and sensitivity analysis modules 51

Source Code 2 – Example of monte carlo simulation using *railtemp* package 84

LIST OF ABBREVIATIONS AND ACRONYMS

AREMA	American Railway Engineering and Maintenance-of-way
CNU	Chungnam National University
CWR	Continuous Welded Rail
EDP	Engineering Demand Parameter
FEA	Finite Element Analysis
FEM	Finite Element Model
IPB	Bragança Polytechnic University
PBEE	Perfomance Based Earthquake Engineering
POE	Probability of Exceedance
STPT	Single tie push tests
UIC	International Union of Railways
UTFPR	Federal University of Technology - Paraná

LIST OF SYMBOLS

T_{air}	Air temperature
T_{rail}	Rail temperature
w_s	Wind speed
H	Relative humidity
SR	Solar radiation
A_s	Area exposed to solar radiation
A_c	Convection area
A_r	Radiation area
α_s	Solar absorptivity
C	Specific Heat capacity
h_{conv}	Convection coefficient
T_{sky}	Sky temperature
V	Volume
ϵ	Emissivity
ρ	Density
k_{sb}	Stefan-Boltzmann constant
σ	Standard deviation
p_f	Failure probability
S_i	Sobol sensitivity index
$\mathbb{E}(X)$	Expected value of the variable X
$\mathbb{V}(X)$	Variance of the variable X
$G(\mathbf{X})$	Limit state function

TABLE OF CONTENTS

1	**INTRODUCTION**	**12**
1.1	**Research Objectives**	**13**
1.2	**Structure of the Document**	**13**
2	**LITERATURE REVIEW**	**15**
2.1	**A brief history of railways**	**15**
2.2	**Technical aspects of railways**	**15**
2.2.1	Rails	16
2.2.2	Railway Gauges	17
2.2.3	Sleepers	18
2.2.4	Fastenings	18
2.2.5	Ballast	20
2.2.6	Jointed tracks	21
2.2.7	Continuous Welded Rail	22
2.3	**Rail temperatures**	**22**
2.3.1	Empirical models	24
2.3.2	Physical models	26
2.4	**Rail buckling**	**34**
2.4.1	Buckling parameters	35
2.4.2	Finite element method for buckling analysis	37
2.5	**Reliability assessment of the temperature prediction models**	**39**
2.5.1	Sensitivity analysis of models	39
2.5.2	Monte Carlo simulations	42
2.5.3	Reliability analysis	45
2.5.4	Fragility Curves	47
3	**METHODOLOGY OVERVIEW**	**48**
4	**SENSITIVITY ANALYSIS**	**50**
4.1	**Methods**	**50**
4.1.1	Considerations on UQLab	51
4.1.2	MATLAB implementation and validation	52
4.1.3	All parameters analysis	52
4.1.4	Hybrid approach using measured data: **"w/ measured data"**	53
4.1.5	Modeling input random variables for sensitivity analysis	53
4.2	**Results**	**54**
4.2.1	MATLAB validation	54
4.2.2	Parameters analysis	56
5	**FRAGILITY ANALYSIS**	**60**
5.1	**Methods**	**60**
5.1.1	Enabling *railtemp* package for Monte Carlo simulations	61
5.1.2	Hybrid approach: using collected data	61
5.1.3	Synthetic approach: using generated weather data	63
5.1.4	Synthetic weather data generation	63
5.2	**Results**	**64**
5.2.1	Challenges and learnings running Monte Carlo simulations with python	64
5.2.2	Hybrid approach	67
5.2.3	Synthetic dataset generation	69
5.2.4	Synthetic approach	72

6 CONCLUSION AND FUTURE WORKS 77
6.1 Future Works 77
BIBLIOGRAPHY 79
APPENDIX A CODE EXAMPLES 84
A.1 Example of *railtemp* monte carlo simulation 84
APPENDIX B COMPLEMENTARY PLOTS 86
B.1 Synthetic weather data generation 86

1 INTRODUCTION

Railway transport has evolved significantly since Industrial Revolution, when simple cast iron rails replaced earlier wood and stone surfaces to reduce friction and increase load capacity. Early rail systems consisted of short segments joined by bolts, which allowed partial thermal expansion of the rail. However, the numerous joints along the track caused mechanical impact damage to both the rails and rolling stock. These limitations motivated the development of Continuous Welded Rail (CWR) technology during World War 2, which enabled rail segments exceeding $240\,\mathrm{m}$ in length compared to the earlier 18 to 20 meter sections (Bonnett, 2005).

While CWR eliminates the problems associated with joints, it introduces new challenges related to thermal stress management. Unlike jointed tracks, CWR cannot freely expand or contract with temperature changes due to lateral constraints imposed by ballast, sleepers, and fastening systems. This restriction causes internal thermal stresses to develop in the rail, which can lead to track buckling under high compressive stress or brittle fracture under excessive tensile stress. Both failure modes pose serious safety risks, though buckling is particularly dangerous as it causes track misalignment that can result in derailment (Bonnett, 2005; Van, 1996).

Railways are continuously exposed to varying environmental conditions, including solar radiation, wind, and seasonal temperature fluctuations, resulting in significant temperature variations along the rail profile. These temperature-induced stresses are especially relevant for CWRs, which, due to the absence of expansion joints, are more susceptible to thermal instabilities compared to traditional jointed tracks (Van, 1996; Kerr, 1978). In Australia, for example, speed restrictions lasting 8 to 9 hours are imposed when air temperatures exceed $38\,^{\circ}\mathrm{C}$, representing significant financial and mobility impacts that may be exacerbated by climate change and extreme weather events (Wu *et al.*, 2010).

Various models have been developed to predict rail temperature under different weather scenarios. These models can be classified into two categories: empirical and physical models. Empirical models rely on fitted relationships derived from local data and tend to perform well within the conditions for which they were calibrated (Wu *et al.*, 2010). However, their applicability across different geographic regions is limited. In contrast, physical models are based on first principles of heat transfer and energy balance, allowing them to simulate rail temperature behavior under diverse and changing weather conditions.

This study focuses on the sensitivity analysis of a previously validated physical rail temperature prediction model proposed by Hong *et al.* (2019b) and Piloto *et al.* (2022). The model is implemented in MATLAB and integrated with the UQLab toolbox (Marelli *et al.*, 2022) to assess the influence of parameter uncertainties on reliability evaluation. Key parameters such as ambient temperature, convection coefficient, and solar radiation, whose values may vary significantly depending on location, surface properties, and weather conditions, are analyzed through both global and data-informed sensitivity methods. Additionally, Monte Carlo simulations are conducted to derive fragility curves for the system considering different threshold values for rail temperature and ambient air temperature. These curves quantify the probability of exceeding

specified thresholds and support risk-informed decision making. Rail temperature data from a segment of track located in the city of Mirandela, Portugal, are used for model validation and analysis. These data are provided by Piloto *et al.* (2022).

The findings contribute to improving the robustness of temperature-based risk assessments, particularly in applications related to thermal buckling prediction and operational safety planning and maintenance practices while minimizing the risk of buckling-related accidents.

Lastly, this work is a continuation of the double degree agreement between Bragança Polytechnic University (IPB) and Federal University of Technology - Paraná (UTFPR), campus Guarapuava.

1.1 Research Objectives

The primary objective of this work is to develop probabilistic fragility curves for railway temperatures through numerical simulations based on a validated prediction model, enabling enhanced thermal buckling risk assessment. Concurrently, this study quantifies how the various input parameters of the simulation model influence the output through comprehensive sensitivity analysis.

Specifically, the research objectives are:

- Estimate the uncertainty associated with input parameters;
- Perform a sensitivity analysis of a physical railway temperature prediction model;
- Conduct Monte Carlo simulations to characterize the temperature output across a wide range of input spectrum;
- Perform a reliability assessment using the data obtained from these simulations.

1.2 Structure of the Document

This document is organized into six chapters. Chapter 1 presents the historical context of railway development, the thermal challenges in continuous welded rail systems, and the research objectives. Chapter 2 reviews the existing literature on rail temperature prediction models, thermal buckling phenomena, sensitivity analysis methods, and reliability assessment methods. Chapter 3 provides an overview of the methodology and analysis framework, establishing the foundation for the two major analyses that follow.

Chapter 4 presents a comprehensive global sensitivity analysis using Sobol indices and Morris methods, identifying the most influential input parameters affecting rail temperature predictions under two scenarios: an all-parameters approach and a hybrid approach incorporating field measurements. Chapter 5 details the fragility analysis conducted through extensive Monte Carlo simulations using both hybrid and synthetic weather generation approaches, quantifying

the probability that rail temperatures reach or exceed critical thresholds relevant to thermal buckling assessment. Finally, Chapter 6 summarizes the main findings, discusses methodological limitations, and presents directions for future research.

2 LITERATURE REVIEW

2.1 A brief history of railways

According to Branco (2008), the concept of tracks dates back to the Roman Empire, where grooves guided carts used for transporting raw materials. Similar principles appeared in the Greek *Diolkos* and in mining, such as in *Trêsminas*, in Portugal, with tracks carved into rock and a gauge of $1.2\,\mathrm{m}$ (Lewis, 2001). Wooden tracks were also used, but left fewer traces. In medieval Europe, transportation was mainly on foot, on horseback, or by carts on poor roads, which highlighted the need for more durable surfaces (Bonnett, 2005).

From the 16th century onwards, there are records of wooden tracks in Germany and in manuscripts from 1480 (Branco, 2008; Lewis, 2001). With the Industrial Revolution, wood was replaced by iron plates and profiles, enabling the use of flanged wheels (Bonnett, 2005). In 1776, iron tracks permanently replaced wood (Branco, 2008), and in 1825 the Stockton and Darlington Railway in England established the modern standard with tracks suitable for steam locomotives, initiating global railway expansion.

In the United States, railways developed rapidly starting in 1828, reaching $9500\,\mathrm{km}$ within twenty years and about $300\,000\,\mathrm{km}$ by the end of the 19th century, driven by mining and westward expansion. An important milestone was the transcontinental railway, completed in 1869 (Hallberg, 2009).

2.2 Technical aspects of railways

The railway system aims to ensure safe, economic, reliable, and comfortable transport of passengers and goods. It is composed of interacting elements subject to varying loads and environmental conditions, requiring proper understanding for secure operations and durability (Fortunato, 2005). Forces coming from rolling stock are transferred downward through rails, sleepers, ballast, and soil. These elements can be categorized into superstructure (rails, fasteners, sleepers) and the substructure (ballast, sub-ballast, roadbed, natural soil), as shown in Figure 1 (Fortunato, 2005).

According to American Railway Engineering and Maintenance-of-way Association (2010), the superstructure comprises rails, sleepers, and track materials, while the substructure consists of granular layers that provide drainage, anchorage and load distribution. Furthermore, it protects the roadbed from climatic forces and allows fine adjustment of alignment.

Historically, railway performance was linked mainly to the superstructure, with limited attention to the substructure. Later studies highlighted the substructure's economic importance due to its influence on maintenance costs (Fortunato, 2005). As noted by Bonnett (2005), early engineers underestimated the role of ballast, often using unsuitable local materials such as ashes or clay.

Figure 1 – Railway cross-section

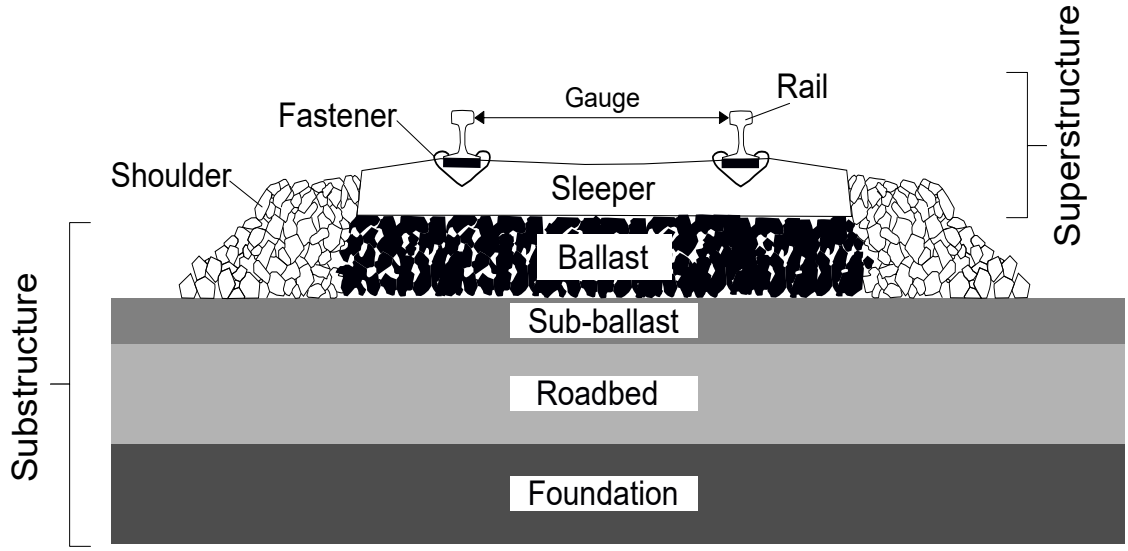

Source: Adapted from Frigeri (2021), Fortunato (2005) and AREMA American Railway Engineering and Maintenance-of-way Association (2010)

To explain stress dissipation of forces originated from rolling stock, this section follows the load path: rails, sleepers, ballast, sub-ballast, and soil. Loads originate from rolling stock, which transmits vertical, horizontal, and longitudinal forces through wheels and rails. Examples include locomotives, freight wagons, passenger coaches, trams, and maintenance vehicles (Bonnett, 2005). In addition, loads derived from weather changes are discussed further in Section 2.3.

2.2.1 Rails

Modern railways employ steel rails due to their well-known strength, fatigue resistance, endurance, and corrosion resistance. Rails act as beams, transmitting concentrated wheel loads to the sleepers without permanent deformation, while also guiding wheel alignment (Bonnett, 2005; Fortunato, 2005; Moreira, 2014).

Rail profiles have evolved since the early bull head or double-head design (Fig. 2a), which proved impractical. The dominant profile today is the *Vignole* or flat-bottom rail (Fig. 2b), composed of head, web, and foot. Profiles are usually designated by weight per unit length, e.g., UIC54 ($54.43\,\mathrm{kg\,m^{-1}}$) and UIC60 ($60.34\,\mathrm{kg\,m^{-1}}$) (Profillidis, 2016). Standardization is ensured by EN 13674 in Europe and American Railway Engineering and Maintenance-of-way (AREMA) AREMA in the USA.

Rail geometry and material properties strongly influence track behavior. Taller profiles increase inertia, distributing loads over more sleepers and reducing stresses on lower layers. Conversely, imperfections in rails or wheels may cause misalignment and damage to track components (Fortunato, 2005).

Figure 2 – Railway profiles

(a) Bull head or double-head (b) Vignole or flat-bottom

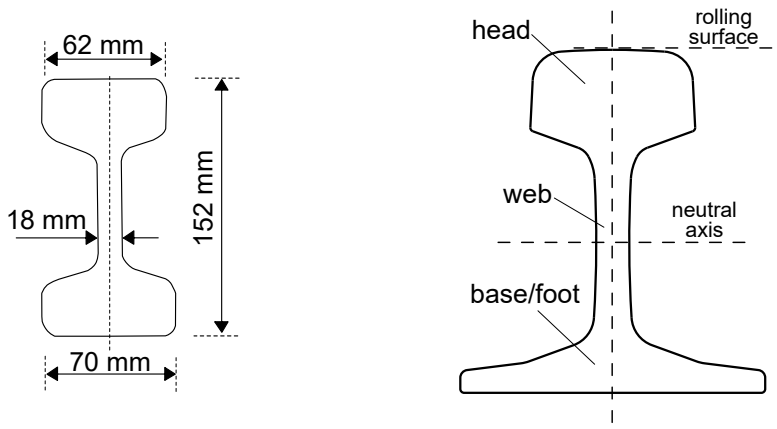

Source: Adapted from Frigeri (2021) and Profillidis (2016)

Steel manufacturing has shifted from ingot to continuous casting, improving production quality. Modern rails are produced using oxygen or electric arc furnaces. Tensile strength has risen from 490 MPa in 1882 to 690 MPa to 1180 MPa today. However, excessive strength reduces ductility and may lead to brittle failure. According to Profillidis (2016), steel quality is classified as:

- Normal quality: ultimate tensile strength 690 MPa to 880 MPa;
- Hard quality: used mainly in curves and crossings, tensile strength 880 MPa to 1180 MPa.

2.2.2 Railway Gauges

Track gauge is defined as the distance between the inner sides of rail heads, measured 14 mm below the rolling surface (Profillidis, 2016). The original English gauge of 1435 mm, later adopted worldwide, is now known as the standard or International Union of Railways (UIC) gauge. Other gauges are also in use and are generally classified as:

- Standard: 1435 mm;
- Metric: 1000 mm;
- Broad: 1520 mm, 1524 mm, 1668 mm, 1676 mm and 1600 mm;
- Narrow: 914 mm and 760 mm.

Globally, $57.5\,\%$ of railways use standard gauge, $26.5\,\%$ broad, $15.5\,\%$ metric, and $0.5\,\%$ narrow, totaling $1\,028\,723$ km of track (Profillidis, 2016). In Europe, most lines are standard gauge, though some countries employ different ones, complicating network integration (Table 1).

Table 1 – Railway gauges in some European countries

Country	Gauge
DE	1435 mm
ES	1000 mm, 1435 mm and 1668 mm
FR	1000 mm and 1435 mm
PT	1000 mm and 1668 mm
UK	1435 mm and 1600 mm

Source: Adapted from Directorate-General for Mobility and Transport (2019).

Portugal and Spain mainly use the Iberian broad gauge of 1668 mm, while many secondary lines adopt metric gauges (Leite, 2017).

Gauge choice significantly influences railway performance. Narrower gauges reduce curvature radius, earthwork, and rolling stock cost, while broader gauges allow higher loads and speeds. The decision must balance technical and economic factors.

2.2.3 Sleepers

Sleepers (or *ties* in North America) are elements placed between rails and ballast (Fig. 1), typically spaced 60 cm. They distribute loads, maintain rail spacing, and constrain vertical and horizontal displacements. Sleepers must provide sufficient mechanical resistance, with wood and concrete being the most common materials (Fortunato, 2005).

Timber sleepers, the first technology used, are adaptable, resilient, and electrically insulating, but limited by high cost, short lifespan, and scarcity. They remain useful where ballast quality is poor, as their flexibility improves load distribution. Lifetimes vary from 25 to 50 years depending on treatment (Bonnett, 2005; Fortunato, 2005; Profillidis, 2016)

Since the 1950s, prestressed-concrete sleepers have largely replaced timber. They offer greater lateral resistance due to weight, better gauge retention, and lifespans of around 50 years. Two main types exist:

- **Mono-block**: good load distribution but lower lateral resistance;
- **Twin-block**: high transverse resistance, suitable for high-speed lines, but less effective in load distribution and requiring reinforcement maintenance (Profillidis, 2016).

The choice between timber and concrete depends on economic and technical factors such as cost, fastening type (see Section 2.2.4), maintenance, and lifetime (Profillidis, 2016).

2.2.4 Fastenings

Fastenings connect rails to sleepers and are classified as rigid or elastic. According to Profillidis (2016), they must:

Figure 3 – Example of concrete sleepers

(a) Mono-block

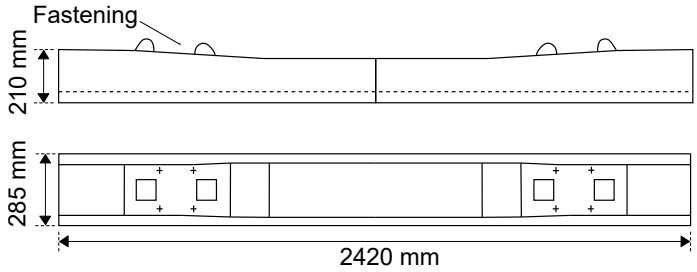

(b) Twin-block

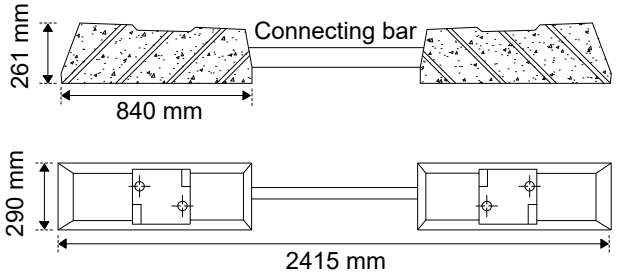

Source: Adapted from (Profillidis, 2016)

- Maintain track gauge and rail inclination;
- Transfer loads to the sleeper;
- Dampen vibrations;
- Allow easy installation and maintenance;
- Provide insulation, durability, and reasonable cost.

They must also withstand vertical, lateral, longitudinal, torsional, and thermal stresses (Fortunato, 2005).

Rigid fastenings, used mainly with timber or steel sleepers, rely on bolts or nails (Fig. 4). Over time, plastic deformations in the sleeper create gaps that loosen the fastening, reducing safety and increasing derailment risk. They also perform poorly under high-frequency vibrations, accelerating wear. Seating plates are therefore recommended (Profillidis, 2016).

Elastic fastenings, required for concrete sleepers, include systems such as *Vossloh*, *Nabla*, and *Pandrol* (Fig. 5). They reduce vibrations and friction, provide insulation, and maintain tightness over time (Fortunato, 2005; Profillidis, 2016).

2.2.5 Ballast

Ballast is a layer of crushed stone that supports the sleepers and fills the space between and beyond them, forming the ballast shoulder (Fig. 1). With a typical thickness of

Figure 4 – Rigid fastening

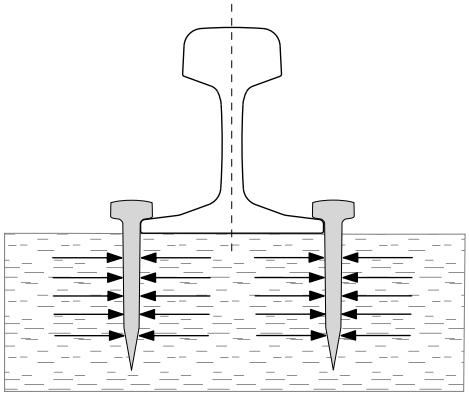

Source: Adapted from (Profillidis, 2016)

Figure 5 – Elastic Pandrol fastening

Source: Marcus Wong on Pandrol (2020)

Table 2 – Comparison between rigid and elastic fastenings

Aspect	**Rigid Fastenings**	**Elastic Fastenings**
Typical use	Timber or steel sleepers	Concrete sleepers
Vibration damping	Poor	Good
Maintenance	Frequent, prone to loosening	Low, long-term tightness
Safety risk	Gaps may lead to derailments	Reliable under dynamic loads
Installation cost	Lower	Higher
Service life	Shorter, affected by wear	Longer, matches sleeper lifespan

Source: Adapted from Profillidis (2016)

20 cm to 40 cm, it provides high vertical compressive strength but relatively low lateral resistance, as stability relies only on friction between particles (Moreira, 2014; Profillidis, 2016). Initially underestimated, the importance of ballast became evident in the early 20th century through experimental research. Today, railway companies pay close attention to its behavior, performance and quality (Fortunato, 2005). The main functions of ballast, according to Profillidis (2016), are:

- Distribute stresses from sleepers to the foundation soil;

- Attenuate train-induced vibrations;
- Resist track shifting (transverse and longitudinal);
- Facilitate drainage;
- Allow restoration of track geometry using maintenance equipment.

Some requirements of ballast are conflicting. For example, high compaction increases load-bearing capacity and stability but reduces drainage efficiency and complicates maintenance. Fortunato (2005) suggests using coarse granular materials (not less than $63\,\text{mm}$) to ensure permeability and ease of maintenance, while other authors argue that finer particles improve stability and compaction.

The behavior of ballast depends not only on its mechanical and hydraulic properties but also on the superstructure, traffic loads, and maintenance practices, making it difficult to establish universal standards (Fortunato, 2005).

2.2.6 Jointed tracks

So far, several components were presented to ensure track stability and stress dissipation through the layers. From a top-view perspective, another essential element is the **rail joint**, which provides continuity between rail bars. Tracks using these elements are classified as *Jointed Tracks*, the earliest type of railway, where rails are connected by fishplates (Fig. 6).

Figure 6 – Fishplate joint

Source: Author (2021)

Rails are typically manufactured in $18\,\text{m}$ segments, welded into lengths of $36\,\text{m}$ or $54\,\text{m}$, and then joined by fishplates using bolts and nuts in pre-bored holes. Each rail profile requires a specific fishplate design. A deliberate expansion gap is left between aligned rails to accommodate thermal expansion, which is the defining feature of jointed tracks (Profillidis, 2016).

While the gap prevents excessive internal stresses in the rail, it introduces drawbacks such as wheel and joint wear, increased noise, reduced passenger comfort, and high maintenance costs (Bonnett, 2005; Profillidis, 2016).

The elimination of joints marked a major improvement, significantly reducing maintenance needs. This became feasible after World War II with the advancement of welding techniques, enabling the development of Continuous Welded Rail (CWR) (Bonnett, 2005).

2.2.7 Continuous Welded Rail

Continuous Welded Rail (CWR) is achieved by welding discrete rail segments. Depending on the country, production lengths vary: 18 m, 24 m, 30 m and 36 m in the UK, 60 m in Germany, and up to 108 m in Austria. In Portugal, rails are welded up to 144 m from 18 m bars, while in the UK lengths reach 240 m. Final welds are carried out in the field to form continuous rail segments (Bonnett, 2005; Leite, 2017; Profillidis, 2016). Before CWR became the standard technology, several challenges had to be solved, particularly the behavior of welded joints under dynamic loads and fatigue, as well as the introduction of elastic fastenings (see section 2.2.4), which are essential for CWR performance.

The main advantages of CWR are (Leite, 2017):

- Reduced deterioration of track components;
- Lower vibration and oscillation of rolling stock.

Unlike jointed tracks, CWR has no expansion gaps, meaning that thermal elongations induce stresses along the rail. This raised concerns about structural stability and buckling, which were addressed through mechanical studies of ballast resistance and by increasing track weight (Profillidis, 2016).

Additionally, numerous models have been developed to predict rail temperatures and assess the risk of thermal buckling. These aspects will be further discussed in the following sections.

Table 3 – Comparison between Jointed Track and Continuous Welded Rail (CWR)

Aspect	**Jointed Track**	**CWR**
Rail length	18 m to 54 m, joined by fishplates	Between144 m to 240 m, continuously welded
Expansion gaps	Present, allow thermal elongation	Absent, thermal stresses distributed along the rail
Ride comfort	Lower, due to noise and vibrations at joints	Higher, smoother and quieter ride
Maintenance	Frequent, fishplates and joints prone to wear	Lower, less deterioration of track components
Safety	Gaps may cause wear and risk of derailments	More reliable under dynamic loads
Cost	Higher long-term due to maintenance	Higher initial, lower lifecycle costs

Source: Adapted from Bonnett (2005) and (Leite, 2017).

2.3 Rail temperatures

Railways are exposed to open weather conditions such as rain, snow, humidity, wind and solar radiation, all varying seasonally. These factors affect the mechanical behavior of rails and may lead to buckling or tensile failures. This section focuses on temperature effects on rails, though other impacts should be noted: rain may cause floods or settlement of tracks after long dry periods, snow leads to drifting, poor adhesion and braking issues, wind can destabilize vehicles or fell trees, while lightning may damage signalling equipment or cause fires (Chapman *et al.*, 2008).

Temperature extremes are critical. High temperatures can cause thermal buckling, often leading to speed restrictions to reduce derailment risk. Conversely, very low temperatures induce contraction and may cause tensile failures. Both jointed and CWR tracks are vulnerable, but welded rails are more prone due to their mechanical constraints. Originally, joints allowed thermal expansion (see section 2.2.6), but with the shift to CWR, this expansion space no longer exists (Chapman *et al.*, 2008).

Research on thermal buckling has advanced since the introduction of CWR. Today, track behavior under high temperatures is well understood through analytical models and Finite Element Analysis (see section 2.4). The current challenge is predicting the onset of critical temperatures, enabling early detection of instability (Wu *et al.*, 2010). For this, models have been developed using field/laboratory data, physical relationships, and computational solvers. They fall into two categories: *empirical models*, which derive correlation equations from observed data, and *physical models*, which apply heat conduction equations, material properties and weather data (Wu *et al.*, 2010). Details are discussed in sections 2.3.1 and 2.3.2.

An important issue is the choice of a representative measurement point, since rail temperature is not uniform across the section. Several studies have addressed this. Hong *et al.* (2019a) conducted experiments on a KS-50N rail segment ($500\,\mathrm{mm}$ long), instrumented with 16 K-type thermocouples across the surface and interior. The ends were insulated to simulate an infinite rail. Over 10 months (Aug 2016–May 2017) of data collection and Finite Element Analysis (FEA) simulations, they identified a representative point $74\,\mathrm{mm}$ above the rail base for buckling studies (Figure 7).

Similarly, Marmash and Ryan (2006) confirmed that surface temperature corresponds closely to bulk rail temperature. The study also warned that measuring at the rail base may underestimate bulk temperature, and reported up to $2\,^{\circ}\mathrm{C}$ difference between the hot and cool sides of the web.

2.3.1 Empirical models

Empirical models rely on field-measured data to approximate rail temperature. Since these relations are site-dependent, variations in local microclimate can limit their general ap-

Figure 7 – Representative temperature measurement point

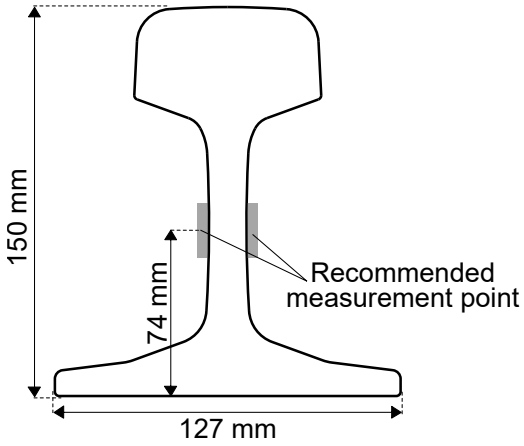

Source: Adapted from Hong *et al.* (2019a)

plicability. Key contributions include those of Hunt (1994), Esveld (2001), and Munro (2009), as reviewed by Wu *et al.* (2010) and Chapman *et al.* (2008).

- Hunt's model

A simple and practical method is to correlate rail and air temperatures, although wind, solar radiation, and humidity also influence rail heating (Chapman *et al.*, 2008). Hunt proposed two relations: Eq. 1 for sunny days and Eq. 2 for cloudy conditions (Wu *et al.*, 2010).

$$T_{rail} = 1.5 \cdot T_{air} \tag{1}$$

$$T_{rail} = T_{air} + 17 \tag{2}$$

- Esveld's model

Esveld (2001) proposed another empirical relation between air and rail temperature for both sunny and cloudy days, valid over a limited temperature range. These correlations are illustrated in figure 8.

Chapman *et al.* (2008) evaluated these models through a 12-month experiment (June 2003–June 2004) at two UK sites, Winterbourne and Leominster, collecting rail temperatures with K-type thermocouples. At Winterbourne, sensors were placed on the rail base, web, and head; at Leominster, data were obtained only from the base of a live line. Although the primary aim was to develop a physical model (section 2.3.2), Chapman first assessed Hunt's and Esveld's correlations, as shown in figure 9.

Large differences in accuracy were found. Equations 1 and 2 give only approximate rail temperatures, as other weather factors (e.g., wind, humidity, solar radiation) influence results. Esveld's model performs better for high temperatures, though figure 9 suggests a non-linear correlation, implying that a look-up chart may outperform simple linear equations (Chapman *et al.*, 2008).

Figure 8 – Esveld correlations for air and rail temperatures

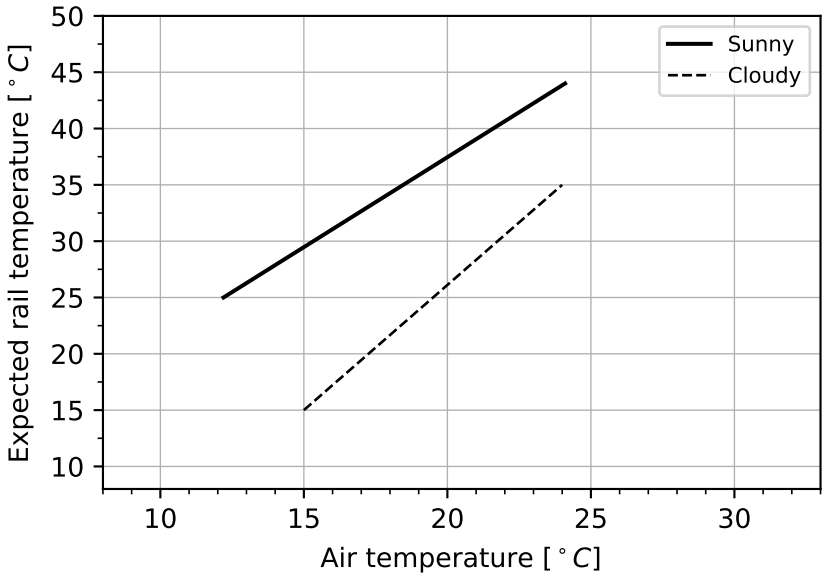

Source: Adapted from Esveld (2001)

Figure 9 – Chapman's collected data

(a) Winterbourne site (b) Leominster site

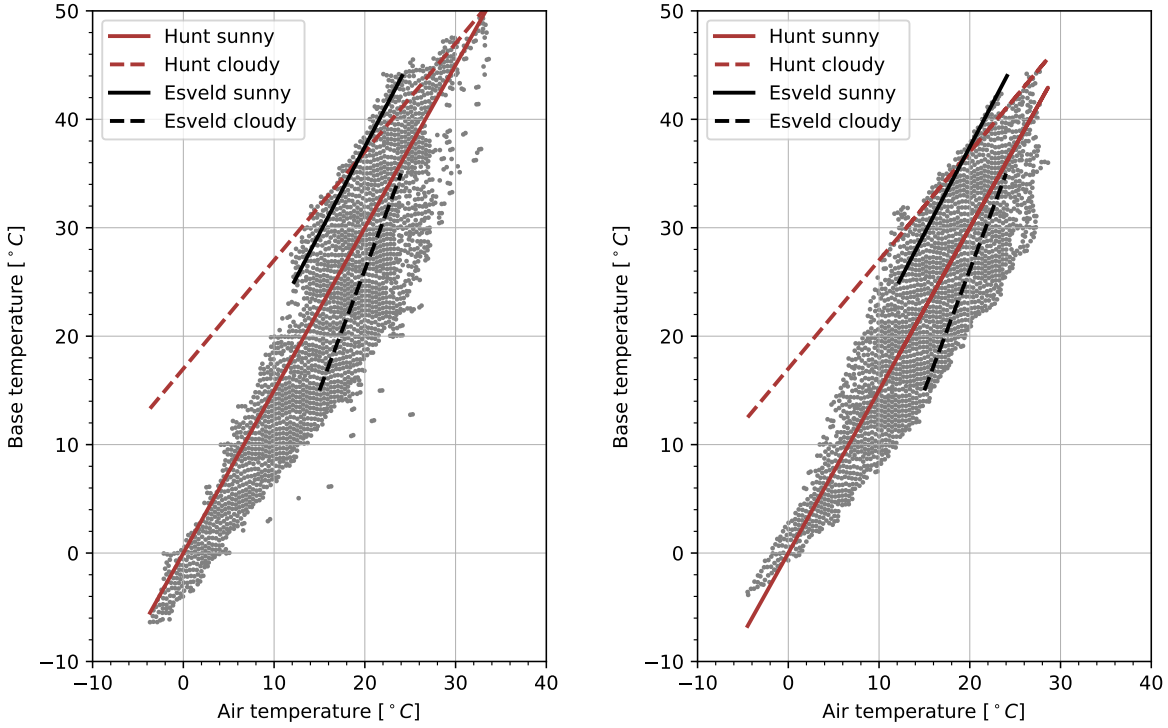

Source: Adapted from (Chapman *et al.*, 2008)

- Munro's model

Munro (2009) extended empirical research to Australian conditions by instrumenting six sites across regional Victoria from July 2008 to February 2010. Using rail stress modules and

nearby weather stations, the author developed equations 3 and 4 to correlate rail temperature with meteorological variables (Wu *et al.*, 2010).

$$T_{rail} = a \cdot T_{air} \tag{3}$$

$$T_{rail} = a \cdot T_{air} + b \cdot SR + c \cdot w_s + d \cdot H \tag{4}$$

T_{air} = Air temperature (°C)

T_{rail} = Rail temperature (°C)

SR = Solar radiation (MJ m^{-2})

w_s = Wind intensity (km h^{-1})

H = Relative humidity ($\%$)

a, b, c, d = Experimentally determined coefficients

Munro found that rail elevation had little influence, though N–S oriented tracks tended to be hotter than E–W ones. Relative humidity had minimal effect, while sleeper material influenced temperature: rails on timber sleepers were 7–15% hotter than those on concrete. Wind effects were highly non-linear, and overall correlations ranged from 0.796 to 0.918 (Wu *et al.*, 2010).

Although these empirical models offer useful insight into rail temperature behavior, they are site-specific and difficult to extrapolate. Future work may benefit from data-driven approaches, such as machine learning or neural networks, to improve generalization and prediction accuracy.

2.3.2 Physical models

Physical models predict rail temperature through heat conduction and energy balance equations based on material and environmental properties. Once the governing variables are known, they can be applied universally. Accurate meteorological forecasts are essential to achieve good predictive performance. According to Chapman *et al.* (2008), such models should outperform empirical ones. Three notable examples are those of Chapman *et al.* (2008), and (Zhang; Lee, 2008–Nineteenth century) Hong *et al.* (2019b); the latter underpins the simulations in this work.

- Chapman's model

Chapman *et al.* (2008) adapted the road surface temperature model of Thornes (1984), originally designed to predict ice formation, to rail applications. This "zero-dimensional" energy balance approach determines equilibrium surface temperature by balancing conductive, convective, and radiative heat exchanges.

The rail geometry was simplified, neglecting minor fillets and slopes, and divided into four regions governed by boundary conditions (figure 10).

Figure 10 – Chapman's simplified rail geometry for heat transfer analysis

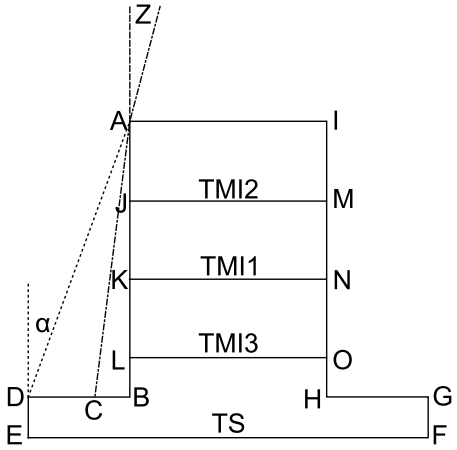

Source: Adapted from (Chapman *et al.*, 2008)

Three surface energy balance equations (Eq. 5) were defined for the head, sun-exposed web, and shaded web, considering net radiation (RN), sensible heat (H), latent heat (LE), and conduction (QS). These terms were calculated through a combination of empirical and analytical relations from Thornes (1984). The surfaces were thermally linked to internal nodes via the 2D heat conduction equation 6.

$$\begin{aligned} \pm RN_H \pm H_H \pm LE_H \pm QS_H &= 0 \\ \pm RN_{W_{sun}} \pm H_{W_{sun}} \pm LE_{W_{sun}} \pm QS_{W_{sun}} &= 0 \\ \pm RN_{W_{shade}} \pm H_{W_{shade}} \pm LE_{W_{shade}} \pm QS_{W_{shade}} &= 0 \end{aligned} \tag{5}$$

$$\frac{\partial T}{\partial t} = K_s \left(\frac{\partial^2 T}{\partial x^2} + \frac{\partial^2 T}{\partial y^2} \right) \tag{6}$$

The model assumed the rail foot was adiabatic with no heat exchange from below. The net heat storage (Eq. 7) allowed solving for foot temperature over time. Simulations used hourly forecast meteorological inputs to predict temperatures up to 24 hours ahead.

$$\partial Q = V \cdot C_s \frac{\partial T_s}{\partial t} \tag{7}$$

Sensitivity tests under constant humidity, wind, and cloud conditions identified solar radiation and air temperature as dominant parameters (table 4). The model achieved an RMSE of $2.5\,^{\circ}\mathrm{C}$ and bias of $0.2\,^{\circ}\mathrm{C}$ over 200 days of data, with a 44-minute lag in predicting peak temperature. Despite simplifications, accuracy was acceptable for practical use (Chapman *et al.*, 2008).

Chapman's model thus provides a practical 1D engineering solution. Extending it to 3D could enhance accuracy but at significant computational cost. The author also notes that foot temperature may not best represent bulk rail temperature for buckling studies (section 2.3). Con-

tinuous monitoring of rail and weather conditions is therefore recommended for local management of thermal stresses.

Table 4 – Chapman's model sensitivity result

Parameter	**Influence**
Latitude	Is not a dominant parameter in relation to maximum temperatures on the longest day. The greatest impact occurs on the shortest day, decreasing the predicted rail temperature towards higher latitudes.
Rail orientation	Affects the timing of the maximum rail temperature. Slightly higher temperatures occur in the N-W/S-E (similar result to Munro's findings (see section 2.3.1). This is explained by the fact that the time in which the rail at this orientation will receive direct beam radiation will coincide with timing of the maximum air temperatures for the day.
Air temperature	Increasing or decreasing the air temperature, will always cause the rail temperature to go higher or to drop, respectively.
Relative humidity	An increase (decrease) in relative humidity results in a small increase (decrease) in forecasted rail temperatures
Wind speed	The effects of wind are greatest during summer, by decreasing rail temperatures. Lowest temperatures tend to occur at low wind speeds. The wind speed affects the convection coefficient and will affect the rail temperature.
Precipitation	When the rail is wet, there is a significant rail temperature decrease during the day.

Source: Adapted from (Chapman *et al.*, 2008)

- Zhang's model

Zhang and Lee (2008–Nineteenth century) and Kesler and Zhang (2007) proposed an energy-balance-based physical model that incorporates weather forecasts to predict rail temperature up to nine hours ahead. Unlike Chapman, temperature measurements were taken on the rail web. Experimental validation preceded large-scale application.

The model uses the energy balance equation 8, reformulated in 9, incorporating solar absorption, convection, and radiation losses. The convection coefficient (h_{conv}) is related to wind speed (Eq. 10) (Kesler; Zhang, 2007).

$$\dot{E}_{in} - (\dot{E}_{conv} + \dot{E}_{rad}) = \dot{E}_{st} \tag{8}$$

$$SR \cdot \alpha_s A_s - [h_{conv} A_c (T_{rail} - T_{air}) + \epsilon k_{sb} A_r (T_{rail}^4 - T_{sky}^4)] = \rho C V \frac{dT_{rail}}{dt} \tag{9}$$

$$h_{conv} = \begin{cases} 5.6 + 4w_s, & w_s \leq 5 \text{ m/s} \\ 7.2(w_s)^{0.78}, & w_s > 5 \text{ m/s} \end{cases} \tag{10}$$

SR = Solar radiation (W m^{-2});

α_s = Solar absorptivity of rail (-);

A_s = Area of rail surface exposed to the sun (m^2);

h_{conv} = Convection coefficient (W m^{-2} K^{-1});

A_c = Area of rail subject to convection (m^2);

T_{rail} = Rail temperature (K);

T_{air} = Ambient air temperature (K);

ϵ = Emissivity of rail (-);

k_{sb} = Stefan-Boltzmann constant (W m^{-2} K^{-4});

A_r = Area of the rail subject to radiation heat transfer (m^2);

T_{sky} = Atmospheric sky temperature (K);

ρ = Density of rail material (kg m^{-3});

C = Specific heat of rail material (J kg^{-1} K^{-1});

V = Volume of rail segment (m^3);

w_s = Wind speed (m s^{-1}).

Key parameters—solar radiation, wind, and air temperature—were obtained from weather stations, while sky temperature was approximated as $20\,^{\circ}$C below ambient. Absorptivity and emissivity of steel were set to 0.75. Figure 11 demonstrates the model's strong correlation between predicted and measured temperatures, particularly on sunny days. Errors mainly stemmed from simplified assumptions for h_{conv} and T_{sky}. The approach effectively generalizes across locations when supplied with appropriate meteorological data.

- CNU model

Hong *et al.* (2019b) at Chungnam National University (CNU) extended Chapman's framework by incorporating the sun's relative position, which dynamically alters the solar absorption area (A_s). Sun geometry was computed via Michalsky's method (Michalsky, 1988), enabling projection of the rail's shadow to estimate the effective irradiated area (figure 12).

The model was validated at Chungnam National University (Korea) between August 2016 and May 2017 using a 500 mm rail segment instrumented with 16 K-type thermocouples. It achieved a correlation of 0.93 and RMSE of $3.8\,^{\circ}$C.

The method projects rail geometry onto the ground to determine the shadow area (S_{shadow}) and correlates the area subject to solar absorption (S_{sun}) via equations 11–12. These values are iteratively input into the energy balance equation 9, solved using MATLAB's ODE45 routine.

$$S_{shadow} = \frac{1}{2}\sum_{i=1}^{n}(x_i + x_{i+1})(y_i - y_{i+1}) \tag{11}$$

Figure 11 – Collected weather data and predicted rail temperatures using Zhang's model

(a) January

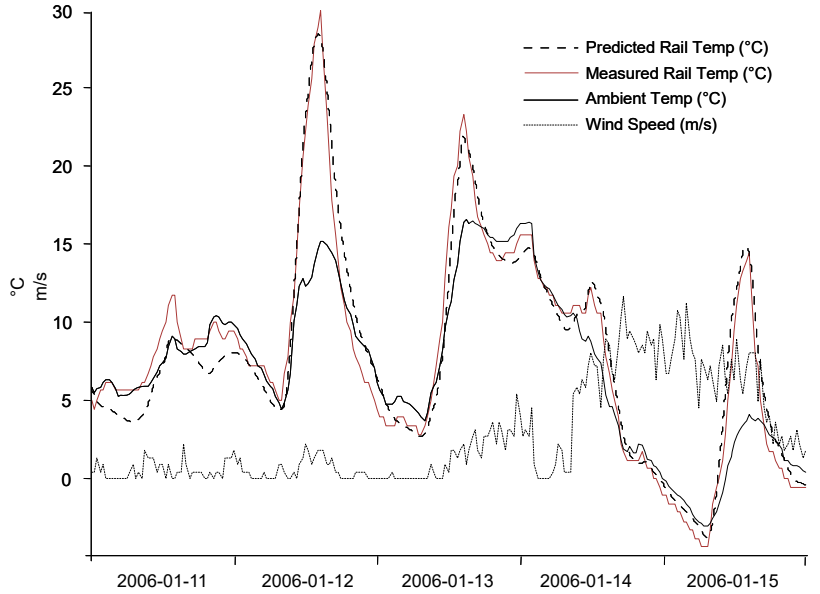

(b) July

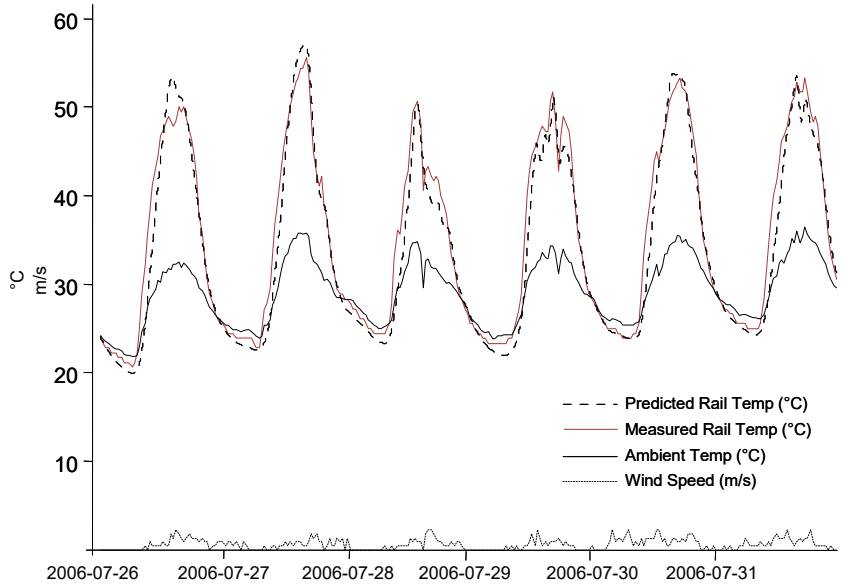

Source: Adapted from Zhang and Lee (2008–Nineteenth century)

$$A_s = S_{sun} = S_{shadow} \sin \alpha_{sun} \tag{12}$$

Reflectance tests determined the rail's absorptivity (unused: 0.984; used: 0.811), confirming the latter for simulations. Table 5 summarizes the model's performance, demonstrating improvement over Hunt's formulations.

In summary, Hong *et al.* (2019b) introduced a refined, geometry-aware physical model capable of accurately simulating rail temperature under varying solar conditions. The authors recommend further validation across different sites, and this model is the basis for simulations in the present study.

Figure 12 – Improvements proposed by the CNU model: (a) Relation between shadow and sun areas; (b) Axes definitions; (c) Example of shadow area projection; (d) Simplified rail 3D geometry

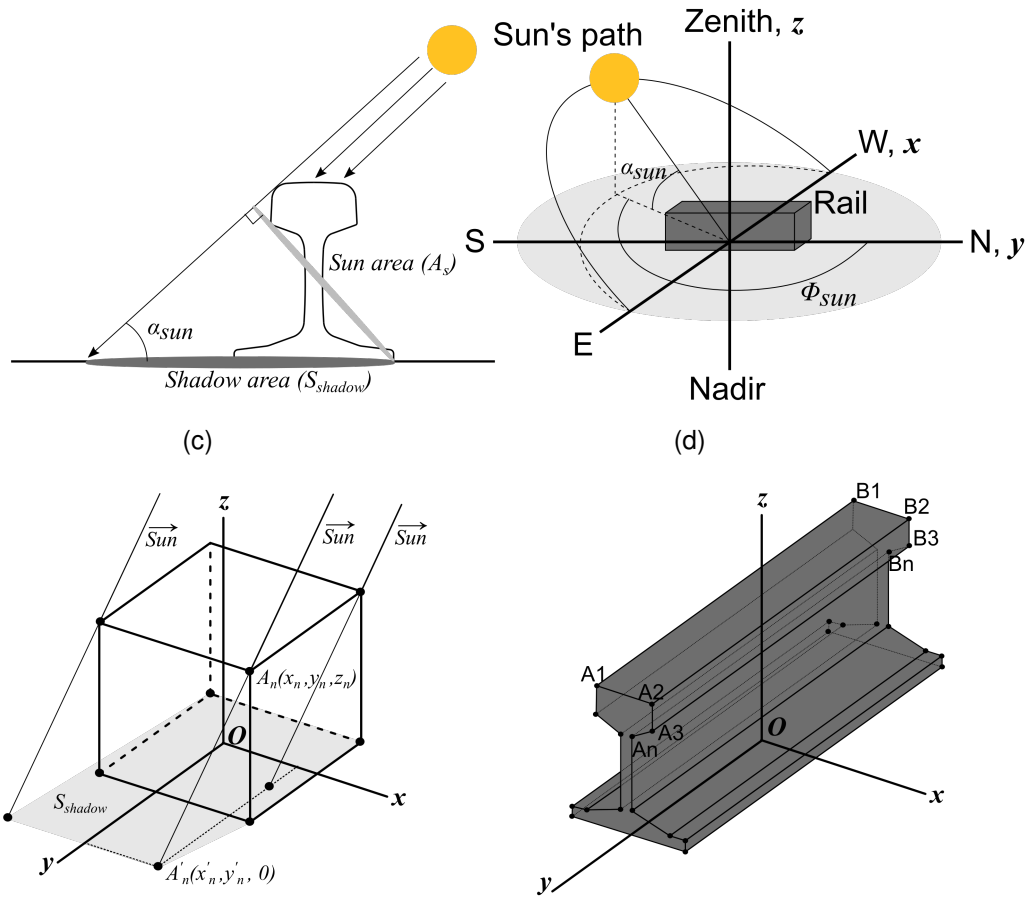

Source: Adapted from Piloto *et al.* (2022) and Hong *et al.* (2019b)

Table 5 – Statistical results for different models

Model	**R^2**	**RMSE**	**Independent variable**
Hunt1	0.90	5.87 °C	Air temperature
Hunt2	0.90	15.11 °C	Air temperature
CNU1	0.93	4.21 °C	Air temperature, solar radiation and wind speed
CNU2	0.93	3.80 °C	Air temperature, solar radiation, wind speed, sun's azimuth and elevation

Source: Adapted from Hong *et al.* (2019b)

- *railtemp* model - CNU improvement

Piloto *et al.* (2022) and Frigeri (2021) developed *railtemp*, an improved version of the CNU model that addresses some of the original model's limitations while maintaining its core energy balance framework. The primary enhancement focuses on refining the method to calculate the area exposed to solar radiation (A_s), building upon the shadow projection approach introduced by Hong *et al.* (2019b). To facilitate reproducibility, the model was implemented as an open-source Python package, providing an easy-to-use, adaptive environment for simulating rail temperatures based on weather conditions.

The *railtemp* model was validated using experimental data collected in Mirandela, Portugal, where a UIC54 profile rail with metric gauge was instrumented with K-type thermocouples welded in the middle of the rail's web. Weather data, including air temperature, solar radiation, and wind velocity, were collected continuously since July 2020 using an automatic weather station. To verify the computational implementation, a Finite Element Model (FEM) was developed using ANSYS for comparison with the Python package results (Figure 13). The temperature history obtained from the finite element analysis showed good agreement with the lumped thermal model implementation, demonstrating that the solving process of the *railtemp* package is correct. Furthermore, the FEM results revealed nearly uniform temperature distribution across the rail section (maximum difference of $0.2\,^{\circ}\mathrm{C}$), validating the lumped thermal model assumption of uniform temperature at each time step. This verification suggests that the Python package can effectively replace FEA for this application, offering a simpler and less time-consuming alternative.

When compared against the original CNU model, *railtemp* demonstrated slightly better performance, achieving a correlation factor (R^2) of 0.947 and a RMSE of $2.689\,^{\circ}\mathrm{C}$ (Piloto *et al.*, 2022). Despite these improvements, the model retains some limitations identified in the CNU framework, including lag in predicting maximum rail temperature and the assumption that sleepers behave adiabatically. Future enhancements could include deeper assessment of parameters such as solar absorptivity, emissivity, and convection coefficient, as well as developing theory to account for thermal interaction between rails and sleepers. Validation across additional geographic locations are suggested to further improve the model's confidence

Figure 13 – *railtemp* package validation against FEM

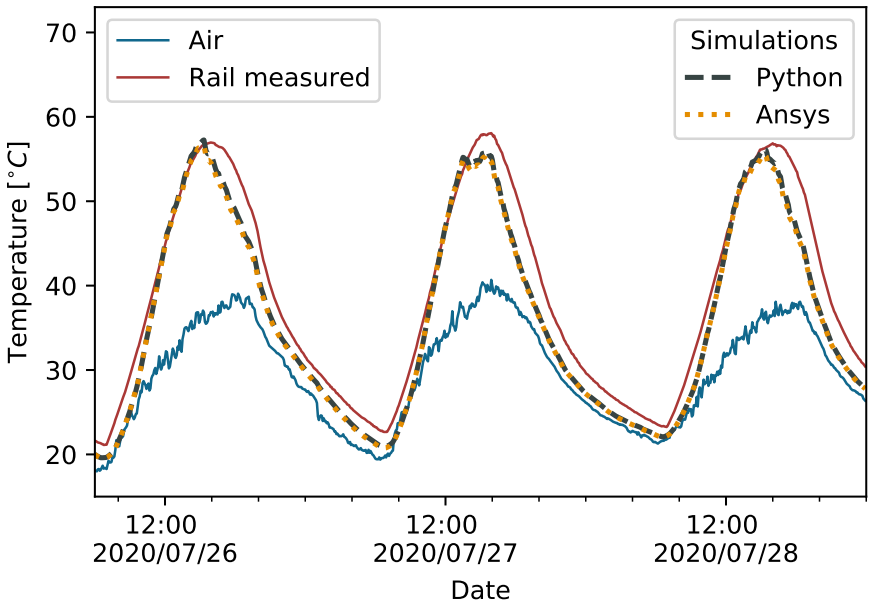

Source: Adapted from Frigeri (2021)

Table 6 – Comparison of empirical and physical rail temperature models

Model	Type	Approach	Validation	Limitations
Hunt (1994)	Empirical	Linear correlation between air and rail temperature, with separate equations for sunny and cloudy days.	Provides approximate estimates only; significant deviation under varying wind, humidity, or radiation.	Accuracy affected by unaccounted meteorological factors (wind, humidity, radiation).
Esveld (2001)	Empirical	Empirical correlation for sunny and cloudy conditions, valid over a limited temperature range.	Performs better for high temperatures; experimental evaluation by Chapman (2008).	Limited range; nonlinear relation suggests lookup chart may be superior.
Munro (2009)	Empirical	Includes solar radiation, wind, and humidity in regression; derived from Australian field data.	Correlation $R = 0.796$–0.918; timber sleepers found to increase temperature by 7–15%.	Site-specific; nonlinear wind effects; limited generalization across climates.
Chapman (2008)	Physical	Zero-dimensional energy balance model adapted from Thornes (1984); divides rail into 4 regions for heat exchange.	RMSE = 2.5°C; bias = 0.2°C; 44 min lag in peak prediction; validated over 200 days.	Simplified geometry; assumes adiabatic rail foot; limited spatial representation (1D).
Zhang (2008)	Physical	Energy balance model incorporating solar absorption, convection, and radiation; convection coefficient depends on wind.	Strong correlation with measured data, particularly on sunny days.	Simplified assumptions for h_{conv} and T_{sky}.
Hong / CNU (2019)	Physical	Extension of Chapman's model including sun position and dynamic solar absorption area; solved using MATLAB ODE45.	RMSE = 3.8°C; $R = 0.93$; validated over 10 months at CNU.	Requires further validation across different sites.
railtemp (2022)	Physical	Improved CNU model with refined solar radiation area calculation; open-source Python package implementation.	RMSE = 2.689°C; $R^2 = 0.947$; validated with field data and FEM in Mirandela, Portugal.	Lag in predicting maximum temperature; assumes adiabatic sleepers; requires additional geographic validation.

Source: Author (2026)

2.4 Rail buckling

Buckling is the sudden change in deformed shape of a structure due to loading, highly dependent on boundary conditions, imperfection levels, and applied loads. Railways are subject to thermal and mechanical loads that, under certain circumstances, may induce buckling. Continuous Welded Rail (CWR) is more susceptible to this phenomenon than jointed tracks because longitudinal movement is restricted. In the presence of thermal loads, deformation cannot occur freely and is instead converted into internal stresses. When the stability limit is reached, the rail releases energy through sudden lateral displacement, transitioning to a new deformed configuration (Fig. 14).

This process can occur through thermal loads alone, *thermal* or *static buckling*, when temperature increases provide sufficient energy to initiate displacement. Alternatively, the combination of elevated temperature and mechanical loads from moving trains can trigger failure at lower temperatures than static buckling, since train loads contribute additional compressive forces. This is known as *dynamic buckling*, which is more prevalent than static buckling due to the uplift tendency of the track between wheel trucks, reducing lateral resistance and creating conditions favorable for buckling initiation (Kish; Samavedam, 2013).

Figure 14 – Lateral buckling examples

(a) (b)

Source: Adapted from Kish and Samavedam (2013)

Buckling poses significant concern in the railway industry, as it can cause train derailments and accidents. Between 1993 and 2003, the annual average of track buckling-induced derailments in the United States was 34, with costs peaking at $17\,\text{million}\text{USD}$ in 2002 (Kish; Samavedam, 2013). Meanwhile, the United Kingdom reported 445 buckling occurrences between 2000 and 2009, six resulting in derailments (Carvalho, 2010).

2.4.1 Buckling parameters

A variety of parameters influence buckling behavior, including track geometric characteristics (tangent and curved sections), material properties (rail steel and ballast), and environmental factors (temperature). According to Kish and Samavedam (2013) and Van (1996), the most important parameters are sleeper-ballast lateral resistance, rail fastener longitudinal and torsional resistance, CWR neutral temperature, track misalignment, and track curvature.

The typical track response can be described using three characteristic temperatures: neutral, buckling, and safe temperatures. The neutral temperature is that at which the track is free of thermal stress, typically the temperature at which the track was laid. The buckling temperature is the threshold at which buckling occurs. The safe temperature is the limit below which buckling cannot occur, regardless of available energy. These concepts are illustrated in Figure 15 (Lim; Park; Kang, 2003; Van, 1996).

Figure 15 – Typical track response curve

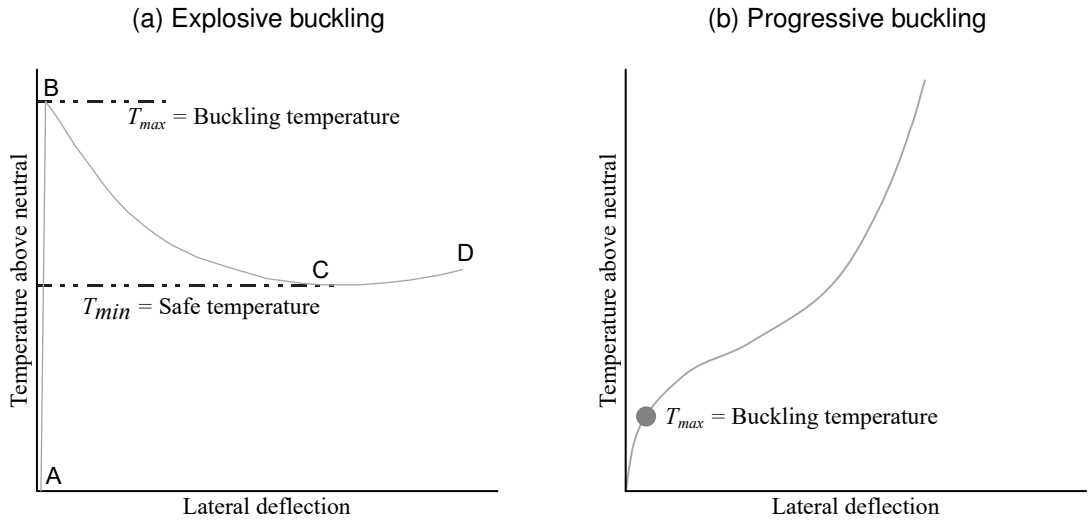

Source: Adapted from Lim, Park and Kang (2003) and Kish and Samavedam (2013)

Figure 15a shows that the buckling response can be divided into three branches: AB, BC, and CD. Branches AB and CD represent stable configurations before and after buckling, while BC contains the unstable configuration where the track shape changes rapidly until reaching the post-buckling deformed shape (Lim; Park; Kang, 2003). Track quality significantly affects buckling response. High-quality tracks exhibit well-defined T_{max} and T_{min} values, producing explosive buckling with sudden snap-through behavior (Fig. 15a). Low-quality tracks show no distinction between these temperatures, experiencing progressive buckling without snap-through (Fig. 15b) (Kish; Samavedam, 2013).

The governing parameters of track buckling can be modeled as shown in Figure 16. Rails are connected to sleepers through torsional springs, while sleepers have lateral and longitudinal displacements restricted by linear springs representing ballast action. For dynamic buckling analysis, vertical springs modeling ballast resistance must be included.

Figure 16 – Typical track model for buckling analysis

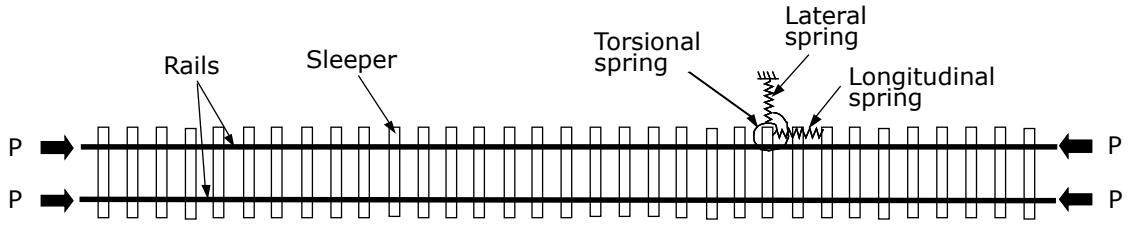

Source: Adapted from Kish and Samavedam (2013)

Table 7 – Fastenings torsional resistance

Sleeper	Type	kN m rad^{-1}	Std
Wood	**Pandrol**	568	221
	8 spikes	245	67
	4 spikes	135	43
	2 spikes	43	16
Concrete	**Pandrol**	32	18
	McKay	39	9

Source: Adapted from Samavedam *et al.* (1993).

The thermal force P due to temperature changes is calculated using Equation 13, where A is the rail profile area, E is Young's modulus, α is the thermal expansion coefficient, T is the current rail temperature, and T_0 is the neutral (stress-free) temperature.

$$P = AE\alpha(T - T_0) \tag{13}$$

Fasteners resist rail rotation and longitudinal slip relative to sleepers, with behavior highly dependent on fastener type and sleeper material. Experiments demonstrate linear torsional behavior, as shown in Figure 17. Table 7 presents torsional resistance values and standard deviations for different fastening methods and sleeper materials (Samavedam *et al.*, 1993).

Figure 17 – Fastener linear model

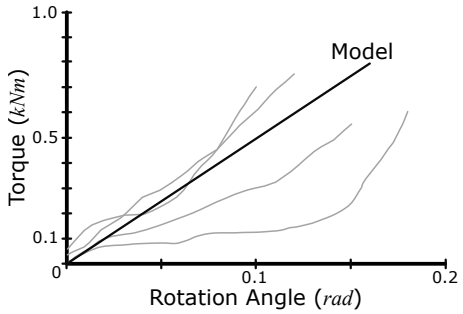

Source: Adapted from Van (1996)

Ballast resistance opposes sleeper displacement in both longitudinal and lateral directions, measured through Single tie push tests (STPT). Typical results are shown in Figure 18. Consolidation from passing trains increases resistance in both directions. Longitudinal resistance is modeled as bi-linear (Fig. 18a), while lateral resistance exhibits a peak value followed by a distinct drop in consolidated track, whereas freshly tamped track maintains peak resis-

tance (Fig. 18b). Lateral resistance correlates linearly with T_{max} and T_{min}—increased resistance elevates temperature thresholds—whereas longitudinal resistance has minimal influence (Van, 1996; Kish; Samavedam, 2013).

Figure 18 – Sleeper-ballast behavior

(a) Typical longitudinal resistance (b) Typical lateral resistance

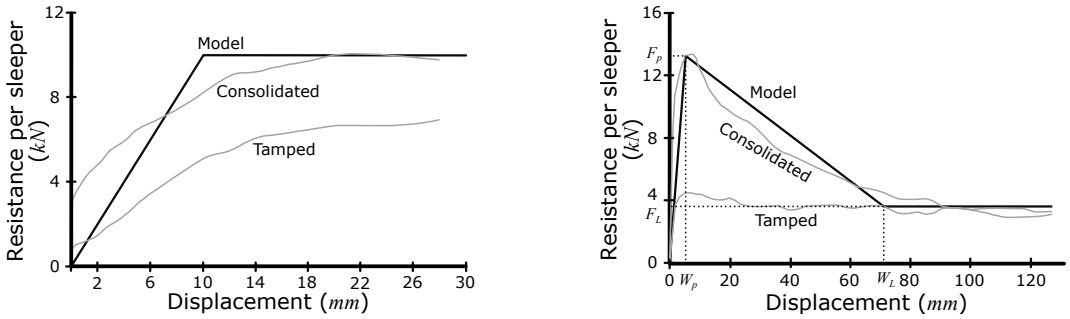

Source: Adapted from Van (1996)

Track misalignment significantly influences buckling temperature (T_{max}), while safe temperature (T_{min}) is less affected (Van, 1996). Imperfections increase due to initial construction tolerances, localized poor ballast conditions, train movement, elevated thermal loads, and excessive vertical loads. Maximum allowable misalignment values have been established: δ_0 (1 mm to 4 mm) after construction, δ_m (4 mm to 8 mm) before maintenance, and δ_c (critical misalignment requiring immediate intervention) (Carvalho, 2010). Misalignment is typically modeled as a sinusoidal wave function with specified amplitude and wavelength (Fig. 19).

Figure 19 – Track misalignment

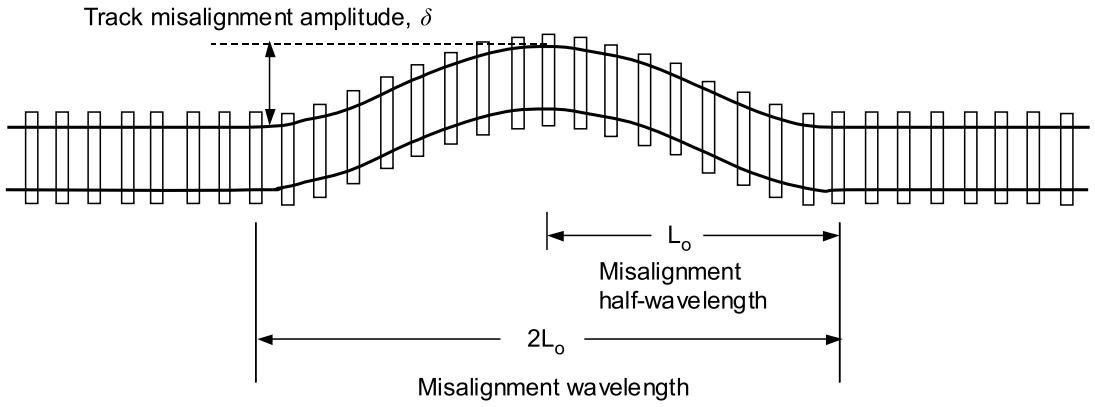

Source: Adapted from Kish and Samavedam (2013)

The stress-free temperature (SFT) is the value at which no thermal stresses exist in the rail, established during welding. In Europe, common design values range from $23\,^{\circ}$C to $27\,^{\circ}$C, though extreme conditions may require $5\,^{\circ}$C to $35\,^{\circ}$C (Carvalho, 2010). Ideally, SFT should fall halfway between the hottest and coldest anticipated rail temperatures (Bonnett, 2005).

2.4.2 Finite element method for buckling analysis

Many models have been developed to study buckling, employing analytical solutions and finite element analysis (FEA). Solutions are classified into beam models (using single equivalent beams) and rail-tie models (treating rail-sleeper interaction separately) (Carvalho, 2010). Notable analytical models include those by Kish and Samavedam (2013), who developed the CRW-safe software for buckling probability assessment, and Van (1996), supported by the European Railway Research Institute.

Lim, Park and Kang (2003) developed a three-dimensional finite element model to obtain full track response (pre- and post-buckling), concluding that 3D models better represent buckling behavior while 2D models overestimate track stability. Figure 20 shows the cross-section and elements used: rail elements following Euler-Bernoulli hypothesis, sleepers modeled as solid beams on elastic foundation (Winkler), fasteners as 3D spring elements with six degrees of freedom, and ballast as nonlinear springs with bi-linear plastic behavior (Fig. 21).

Figure 20 – Lim, Park and Kang (2003) cross-section model

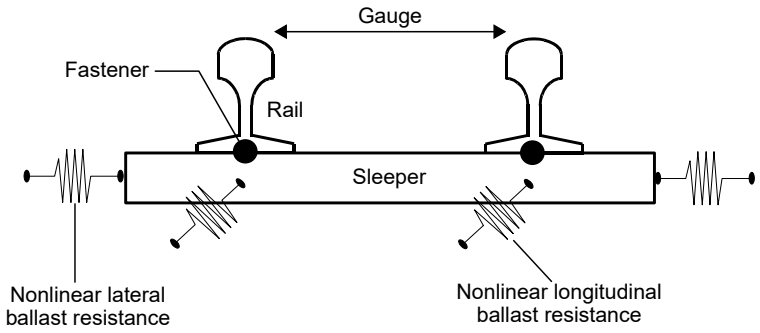

Source: Adapted from Lim, Park and Kang (2003)

Figure 21 – Ballast lateral and longitudinal behavior utilized by Lim, Park and Kang (2003)

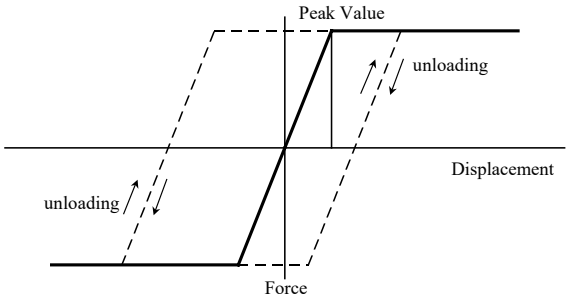

Source: Adapted from Lim, Park and Kang (2003)

Carvalho (2010) utilized ANSYS software to solve rail buckling problems, comparing results with Lim, Park and Kang (2003)'s model. However, available solvers could not resolve full buckling response. Newton-Raphson and arc-length methods are available for iterative solutions, but arc-length—suitable for snap-through problems—failed to converge when handling thermal loads. Consequently, Carvalho (2010) proposed an indirect method combining analytical and finite element models to determine full buckling response for tracks exhibiting explosive buckling behavior.

Piloto, Frigeri and Minhoto (2022) used Finite Element Analysis to study the thermal buckling on railway sections with timber sleepers and different misalignment (imperfections). The analysis reveals that both lateral ballast resistance and track misalignment significantly influence buckling temperature. As shown in Figure 22a, the relationship between lateral ballast resistance and buckling temperature exhibits linear behavior, where the misalignment acts as the angular coefficient. Consequently, tracks with lower imperfections experience a steeper increase in buckling threshold temperature as lateral resistance improves. In contrast, Figure 22b demonstrates non-linear behavior when examining the effect of misalignment on buckling temperature. These results, summarized in Figure 22, demonstrate that lateral ballast resistance and track misalignment are influential parameters in determining thermal buckling temperature. In summary, in the case of poor ballast quality, these results shows that buckling may occur around $60\,^{\circ}$C, which raises concern given that the maximum registered temperature (T_{rail}) in the Portuguese city of Mirandela was near $60\,^{\circ}$C during a summer day (refer to Fig. 13) (Piloto; Frigeri; Minhoto, 2022).

Figure 22 – Variation of thermal buckling temperature

(a) Effect of the lateral ballast resistance (b) Effect of the misalignment

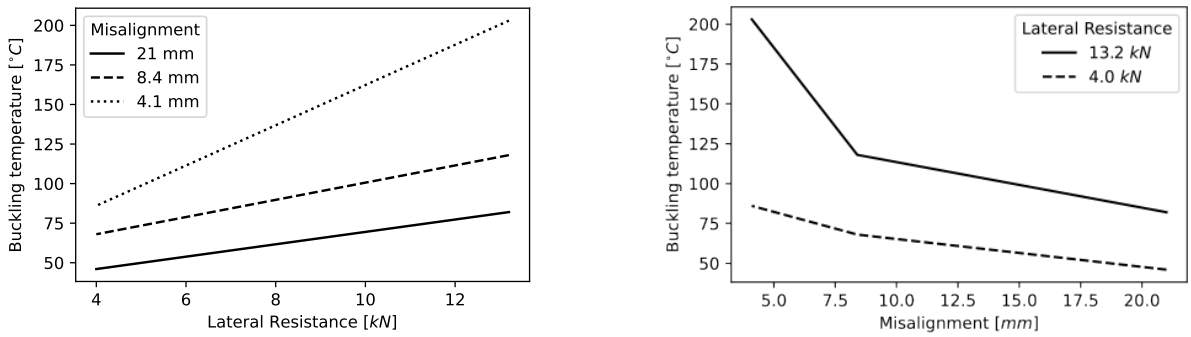

Source: Adapted from Piloto, Frigeri and Minhoto (2022)

2.5 Reliability assessment of the temperature prediction models

Sensitivity analysis, Monte Carlo simulation, and reliability analysis are fundamental tools in modern engineering practice for managing uncertainty and assessing system performance under variable conditions. In the context of railway infrastructure, where temperature-induced thermal stresses can lead to track buckling and subsequent safety hazards, these methods provide a framework for evaluating the reliability of temperature prediction models and quantifying buckling risk. This section presents a brief explanation of these tools, that will be used to assess the CNU and *railtemp* models: sensitivity analysis is employed to identify the most influential input parameters (e.g., solar radiation, wind speed, material properties) that govern rail temperature predictions; Monte Carlo simulation enables the propagation of input uncertainties through the physical models to generate probabilistic temperature forecasts; and reliability analysis translates these temperature distributions into quantitative estimates of critical temperature

thresholds exceedance. Together, this framework support informed decision-making for railway maintenance and operation under uncertain environmental conditions.

2.5.1 Sensitivity analysis of models

Multiple models can reproduce the same observations while maintaining fundamentally different structures, a phenomenon known as equifinality or model indeterminacy. This reality underscores the importance of sensitivity analysis as a systematic approach to quantify how uncertainty in model inputs propagates to model outputs. According to Saltelli *et al.* (2008), sensitivity analysis addresses the question: *how does uncertainty in model parameters influence the reliability and precision of model predictions?*. Furthermore, the goal of sensitivity analysis is to determine which factors within the total set of factors in the model should be the focus of attention; that is, which factors have really important effects on the output (Groenendaal; Kleijnen, 2002).

Sensitivity analysis can be broadly categorized into local and global approaches, which differ fundamentally in scope and methodology. Local sensitivity analysis examines the effect of small perturbations around a nominal parameter value, typically computing derivatives of model outputs with respect to individual inputs. This approach is fundamentally deterministic and does not require the assignment of probability distributions to model inputs, which can be advantageous when the state of knowledge is insufficient to confidently specify input distributions. However, local methods may fail to capture the full behavior of complex models where parameters vary over wide ranges or exhibit nonlinear interactions (Saltelli *et al.*, 2008).

In contrast, global sensitivity analysis explores the entire input parameter space and quantifies the contribution of each parameter (or combination of parameters) to the total output variance. These probabilistic methods require the assignment of probability distributions to model inputs but offer a more comprehensive analysis framework, accounting for the full range of input uncertainties and their propagation through the model. Global methods provide variance-based sensitivity indices that quantify the contribution of each input to the total output uncertainty, making them particularly valuable for uncertainty quantification and priority setting, enabling researchers to identify which factors most require improved characterization and which model components propagate the greatest uncertainty to predictions (Saltelli, 2007; Borgonovo; Plischke, 2016; Groenendaal; Kleijnen, 2002).

Setting priority is one of the applications of this tool, indeed, application of sensitivity analysis depends on the problem setting and the objectives of the investigation. Saltelli *et al.* (2008) distinguish four principal settings: *Factor Prioritization (FP)*, which aims to identify the most important factors whose determination would lead to the greatest reduction in output variance; *Factor Fixing (FF)*, which seeks to identify non-influential factors that can be fixed at any value within their uncertainty range without significantly affecting output variance; *Factor Mapping (FM)*, which categorizes model realizations into groups (e.g., acceptable versus non-acceptable outcomes) and identifies which factors are most responsible for producing realiza-

tions in a specific region of interest; and *Variance Cutting (VC)*, which determines the smallest subset of factors that must be fixed to reduce output variance from its unconditional value to a pre-established threshold. Each setting addresses different decision-making needs and requires appropriate sensitivity measures and interpretation frameworks.

In the context of the present work **global sensitivity** methods are employed, to understand which variables of prediction model, such as, solar radiation, air temperature, wind speed, material properties or geometric constraints, exert the strongest influence on predicting rail temperatures, in other words, aiming for the factor prioritization setting. By identifying the most influential parameters, sensitivity analysis guides calibration procedures and reveals which model assumptions require the most careful validation.

- Sobol Index

Sobol's indices can be used for the setting of parameter prioritization, and it measures the relative impact on the variance of the model response when some factor (input variable) is fixed. Because these indices decompose variance contributions, they are classified as variance-based sensitivity measures, building upon analysis of variance (ANOVA) decomposition principles. Consider the function $Y = f(\mathbf{X})$, where $f : \mathbb{R}^m \to \mathbb{R}$ is the mathematical model and $\mathbf{X} \in \mathbb{R}^m$ is the vector of input variables, Sobol's first order index is defined in Equation 14 (Sobol′, 2001; Torii *et al.*, 2023; Saltelli *et al.*, 2008).

$$S_i = \frac{\mathbb{V}_i(Y)}{\mathbb{V}(Y)} = \frac{\mathbb{V}\left[\, E\left(Y \mid X_i\right)\right]}{\mathbb{V}(Y)} \tag{14}$$

The second order index is demonstrated in Equation 15. It captures how the variance output happens due to the interaction of these two parameters.

$$S_{ij} = \frac{\mathbb{V}_{ij}(Y)}{\mathbb{V}(Y)} = \frac{\mathbb{V}\left[\, E\left(Y \mid X_i, X_j\right)\right] - \mathbb{V}_i - \mathbb{V}_j}{\mathbb{V}(Y)} \tag{15}$$

In order to account for higher order influences, meaning the interaction between the input variables, the sobol total index can be calculated using Equation 16.

$$S_i = 1 - \frac{\mathbb{V}\left[\, E\left(Y \mid X_{\sim i}\right)\right]}{\mathbb{V}(Y)} \tag{16}$$

Where

$\mathbb{E}$ = Expected value

$\mathbb{V}$ = Variance

$\mathbb{E}\left[Y \mid X_i\right]$ = Expected value of Y conditioned to X_i

$\mathbb{E}\left[Y \mid X_{\sim i}\right]$ = Expected value of Y conditioned to all inputs **except** X_i

- Morris analysis

The elementary effects (EE) method, introduced by Morris in 1991, is a computationally efficient screening technique designed to identify important input factors in models with many parameters. Morris' method computes multiple local sensitivity measures—termed elementary effects—across a discretized input space and averages them to provide a global assessment of factor importance. The method produces sensitivity measures (such as μ^* and σ^*) that approximate total sensitivity indices. By examining each factor individually rather than in groups, the method avoids cancellation effects where factors with opposing influences might mask each other's importance, making it particularly suitable when variance-based techniques are computationally prohibitive, but individual factor screening is still feasible (Saltelli, 2007; Saltelli *et al.*, 2008).

Assuming the input parameters $\mathbf{X}$ vary in a *M*-dimensional unit hypercube, i.e. $X_i \in [0,1]$ $i = 1, \ldots, M$, which in real use cases, can be rescaled to the real input space. A grid of *p* values is created for each parameter, consisting the set described in Equation 17.

$$\mathcal{G}_i = \left\{0, \frac{1}{p-1}, \frac{2}{p-1}, \ldots, 1\right\}. \tag{17}$$

Assume Δ as a perturbation parameter and for a given value of $x = \{x_1, \ldots, x_M\}^T$, such that $x_i + \Delta \leq 1$, the elementary effect of the variable x_i is defined in Equation 18.

$$d_i(x) = \frac{\mathcal{M}(x_1, \ldots, x_i + \Delta, \ldots, x_M) - \mathcal{M}(x)}{\Delta} \tag{18}$$

Where $\mathcal{M}(x)$ is the first-order expansion of the model around the mean value, with details discussed by (Marelli *et al.*, 2022; Morris, 1991). Once the elementary effects of each variable are calculated ($d_i(x)$), the mean and standard deviation are analyzed and plotted graphically. A high mean value, indicates that the variable is important, and the input values causes variability on the outputs of the model. Meanwhile, a high standard deviation indicates that the effect of the variable X_i is significant, either due to nonlinear behavior with respect to this variable of due to integrations with other input variables (Marelli *et al.*, 2022).

2.5.2 Monte Carlo simulations

The Monte Carlo method is a numerical technique that solves mathematical problems through the simulation of random variables. As described by Sobol (1994), this approach became practical as a universal numerical tool only with the advent of computers, since manual simulation of random variables is laborious. The method is characterized by two key features: first, a simple computational algorithm structure based on repeated independent trials (hence also called the method of statistical trials), where results are averaged over N realizations; second, a calculation error proportional to $\sqrt{D/N}$, where D is a constant an$N$ is the number of trials. This implies that reducing the error by a factor of 10 requires increasing the computational effort by a factor of 100. The Monte Carlo method is particularly suitable for simulating processes

influenced by random factors and for constructing probabilistic models of deterministic problems where uncertainty quantification is needed. In the context of this work, within rail temperature prediction models, Monte Carlo simulations enable the propagation of input uncertainties (e.g., weather data, material properties) through the physical models to quantify the reliability of temperature forecasts and assess buckling risk under uncertain conditions.

To apply this method, it is necessary to define key terms and premises. A random variable, from a mathematical perspective, has a precise definition: while its value in any given trial is unknown, the set of possible values and their associated probabilities are known. Consequently, a single trial using this random variable cannot precisely predict a phenomenon. However, when numerous trials are conducted, the prediction becomes increasingly reliable. As the number of trials increases, prediction accuracy improves proportionally (Sobol, 1994).

The random variable can be discrete, in this case, there is a table associating a given value with its probability. Similarly, the variable can be continuous and expressed with a function. In fact, a continuous random variable ξ is defined by specifying an interval containing all its possible values (a and b), and a function $p(x)$, that is called *probability density* of the variable, or the *distribution density*. In fact, this function takes various forms, such as: normal, uniform and many others. The definition of these functions is detailed by Sobol (1994).

Figure 23 – Probability density of continuous variables

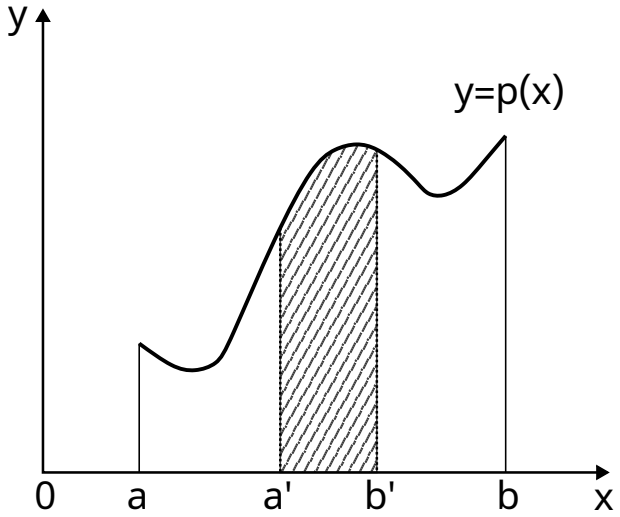

Source: Adapted from (Sobol, 1994)

From Figure 23, the probability that ξ falls in the interval (a',b') is defined in Equation 21. The set of values can be any interval, including cases $a = -\infty$ and/or $b = \infty$.

$$P\{a' < \xi < b'\} = \int_{a'}^{b'} p(x)dx \tag{19}$$

The density $p(x)$ must satisfy these conditions

- $p(x) \geq 0$ inside (a,b);
- $\int_a^b p(x)dx = 1$.

Also, it is possible two define two numbers: expected value (Eq. 20) and variance of the variable ξ (Eq. 21).

$$\mathbb{E}_\xi = \int_a^b xp(x)dx \tag{20}$$

$$\mathbb{V}_\xi = \mathbb{E} \cdot ([\xi - \mathbb{E}\xi]^2), \tag{21}$$

where $\mathbb{E}$ is the expected value operator.

For multiple random variables $\xi_1, \xi_2, \ldots, \xi_n$, the concept extends to a joint probability density function $p(x_1, x_2, \ldots, x_n)$, which characterizes their simultaneous behavior. The probability that the vector of random variables falls within a specific region $\mathcal{D}$ in the n-dimensional space is given by Equation 22.

$$P\left\{(\xi_1, \xi_2, \ldots, \xi_n) \in \mathcal{D}\right\} = \int \cdots \int_{\mathcal{D}} p(x_1, x_2, \ldots, x_n)\, dx_1\, dx_2 \cdots dx_n \tag{22}$$

With these definitions established, a simple example illustrating the general application of the method is presented. Consider the problem of estimating the reliability of an electrical device composed of different components denoted by C_k. The components are connected in a mixed series-parallel configuration, as shown in Figure 24. Assuming that the breakdown time is a constant known value (for now), the breakdown time for the entire device can be expressed by Equation 23. In this configuration, if components are connected in series, the system fails when the first component fails. Conversely, if components are in parallel, the system continues operating as long as at least one branch remains functional (Birolini, 1999).

Figure 24 – Scheme of a device corresponding to Equation 23

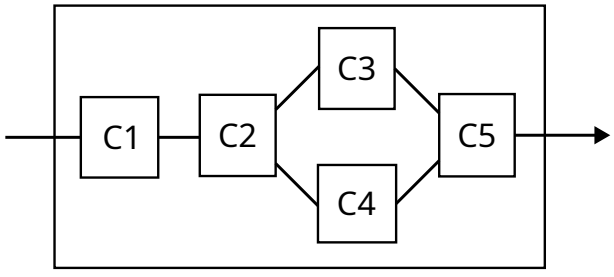

Source: Adapted from Sobol (1994)

$$t = \min(t_1; t_2; \max(t_3; t_4)); t_5) \tag{23}$$

Now, assume that each component has its own breakdown time distribution denoted by θ_k. The Monte Carlo simulation proceeds by generating independent pseudo-random numbers from each component's distribution and evaluating Equation 23. By repeating this trial N times, an approximation of the expected breakdown time for the entire device θ_{dev} can be obtained. Applying Equation 20, this yields:

$$\mathbb{E}_{\theta_{dev}} \approx \frac{1}{N} \sum_{j=1}^{N} t_j,$$

Where t_j is the value of the t obtained in the tth numerical experiment.

This example, detailed by Sobol (1994), demonstrates how the Monte Carlo method can be used to estimate the combined behavior of multiple inputs, each with its own probability distribution. Despite its conceptual simplicity, the method provides powerful insights into system behavior. Beyond computing expected values and variances, analyzing all generated trial results enables the construction of histograms that serve as approximations to the unknown probability density of the entire device.

In the context of this work, the Monte Carlo method is applied to Equation 9 to estimate rail temperature behavior by treating input parameters as random variables and performing computational experiments. This application is discussed in detail in Section 5.1.

2.5.3 Reliability analysis

Reliability engineering is a discipline whose purpose is to develop methods and tools to predict, evaluate, and demonstrate reliability, maintainability, and availability of components, equipment, and systems, as well as to support development and production engineers in building reliability and maintainability (Birolini, 1999). According to (Birolini, 1999), reliability is a characteristic of an item, expressed by the probability that the item will perform its required function under given conditions for a stated time interval, or more simply, the ability of an item to remain functional. Failure occurs when an item stops performing its required function. Safety, another critical aspect, is the ability of an item not to cause injury to persons nor significant material damage.

Kaufmann, Grouchko and Cruon (2010) proposes hypotheses to establish the reliability of a system. A system is considered to be in a "good state" when the following conditions are fulfilled:

- The system has only two possible states: functioning well OR failed;
- The system may be decomposed into *r* components in such a way that each component, at a given instant, is either in a good OR failed state;
- Each of the components of the system has a random lifetime denoted by T_i;
- The random variables T_i are independent.

The concepts defined above apply to systems in general. However, these definitions can be adapted and further specified to address civil and mechanical engineering problems.

In this context, Ditlevsen and Madsen (1996) defines what is a deterministic and probabilistic structural analysis. Deterministic structural analysis as the art of formulating a mathemati-

cal model that answers the question: "How does a structure behave when its material properties, geometric properties, and actions are all uniquely given?". However, in many practical situations, material properties, geometric dimensions, and applied loads are not precisely known but rather exhibit random or incompletely characterized behavior. Probabilistic structural analysis extends the deterministic framework to address such uncertainty. It formulates a mathematical model that answers the question: "What is the probability that a structure behaves in a specified manner when one or more of its material properties, geometric dimensions, or applied actions are of a random or incompletely known nature?". This extension from deterministic to probabilistic methods enables quantitative assessment of structural reliability under uncertainty (Ditlevsen; Madsen, 1996).

In addition, according to (Melchers; Beck, 2018) and (Morales, 2013), the fundamental structural reliability considers a Load S and a strength resistance R, for example a rope with a weight tied to it, S is the total weight and R is the limit capacity of the rope to keep integrity. From this statement, is possible to derive the limit state equation for the system (Equation 24)

$$G(\mathbf{X}) = R - S = G_r(X_1, \ldots, X_n) - G_s(X_1, \ldots, X_n) \tag{24}$$

Where **X** is the vector of n input random variables. Based on this equation, three regions can be defined:

- Limit state: $G(\mathbf{X}) = 0$;
- Safe region: $G(\mathbf{X}) > 0$;
- Fail region: $G(\mathbf{X}) < 0$.

These definitions are illustrated in Figure 25.

Figure 25 – Reliability limit states and regions

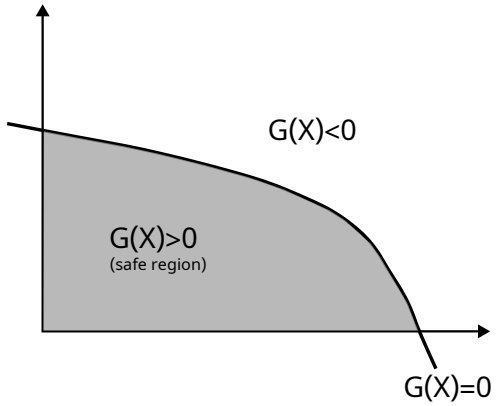

Source: Adapted from Morales (2013)

The failure probability can then be calculated using Equation 25:

$$p_f = P(G(\mathbf{X}) \leq 0) = \int \int_{G(\mathbf{X}) \leq 0} f_x(x) dx \tag{25}$$

Where $f_x(x)$ is the joint probability density function of the vector **X**. Further mathematical details are provided by Ditlevsen and Madsen (1996), Morales (2013), Melchers and Beck (2018) and Iantas (2021).

However, Equation 25 cannot be solved analytically in general. Melchers and Beck (2018) suggests two approaches: either transforming the input variables into approximated multi-normal distributions or employing numerical methods such as Monte Carlo simulation (discussed in Section 2.5.2).

In the context of the present work, sensitivity and reliability analysis are applied in conjunction with Monte Carlo simulation and temperature prediction model (particularly CNU and *railtemp*) to perform probabilistic analysis of thermal buckling risk. For example, given a binary failure criterion: the railway system is assumed to enter critical operational condition when the rail temperature reaches or exceeds a critical threshold (e.g., $60\,^{\circ}\mathrm{C}$), meaning the system state is either operational or failed. This methodology is further discussed in Section 5.1.

2.5.4 Fragility Curves

Fragility curves are probabilistic tools developed within the Perfomance Based Earthquake Engineering (PBEE) methodology framework, which revealed that structures complying with traditional seismic codes still experienced unacceptably high damage and economic losses. The PEER methodology establishes a probabilistic cascade that explicitly accounts for uncertainties in hazard intensity, structural response, physical damage, and consequences (Günay; Mosalam, 2013). Within this framework, fragility curves establish the relationship between an Engineering Demand Parameter (EDP), such as interstory drift, floor acceleration, or peak ground motion, and the Probability of Exceedance (POE) of specific damage states, which ultimately inform a decision variable meaningful to stakeholders, including economic losses, downtime, and casualties. Unlike deterministic design approaches that rely on single threshold values, fragility curves explicitly capture inherent uncertainty in component capacity, loading variability, and damage progression, providing a probabilistic framework where a specific EDP value corresponds to multiple damage states with associated probabilities. The construction of fragility curves typically relies on experimental testing, finite element simulations, empirical data from observed failures, or expert judgment, enabling engineers to quantify system reliability under uncertain conditions (Bosse, 2022; Günay; Mosalam, 2013).

In the context of railway thermal buckling, rail temperature is the primary engineering demand parameter that governs the thermal stress state and buckling potential in continuous welded rail systems. When rail temperature reaches or exceeds critical thresholds—influenced by parameters such as lateral ballast resistance, track misalignment, fastener properties, and neutral temperature (Piloto; Frigeri; Minhoto, 2022)—the probability of buckling increases. The present work adapts this fragility curve methodology by developing probabilistic relationships between ambient air temperature (as the primary hazard intensity measure) and the probability of exceeding critical rail temperatures corresponding to different damage states. Through

Monte Carlo propagation of weather uncertainties via the CNU and *railtemp* temperature prediction models, combined with sensitivity analysis, fragility curves are constructed that quantify the conditional probability of rail temperature exceeding critical buckling thresholds for given atmospheric conditions.

These curves serve as a foundation for, or may be integrated within, an in-depth probabilistic buckling assessment framework, enabling comprehensive performance-based evaluation. This probabilistic approach allows railway infrastructure managers to quantify the risk of service disruption, speed restrictions, or derailment under uncertain environmental and material conditions, thereby supporting informed maintenance scheduling and operational decision-making. The complete performance-based buckling assessment framework, however, extends beyond the scope of the present work.

3 METHODOLOGY OVERVIEW

This chapter presents an overview of methodology for the analysis of the *railtemp* model through systematic sensitivity analysis and extensive Monte Carlo simulations for a fragility assessment. The framework is structured in two major components: first in Chapter 4, a global sensitivity analysis using Sobol indices to identify the most influential input parameters affecting rail temperature predictions; second in Chapter 5, fragility analysis via Monte Carlo simulations to quantify the probability that rail temperatures will reach or exceed critical thresholds under various ambient air temperatures scenarios. These probabilistic analyses provide essential insights for railway infrastructure risk assessment, particularly concerning thermal buckling hazards.

The *railtemp* package employs Equations 9 and 10, incorporating the improvements regarding solar absorption area calculation discussed in Section 2.3.2. The sensitivity analysis is conducted using two approaches: an **"all parameters"** scenario treating all inputs as random variables, and a **"hybrid"** approach incorporating field measurements for weather parameters while randomizing material and geometric properties. The Fragility analysis via Monte Carlo simulations similarly adopts **"hybrid"** and **"synthetic"** strategies, with the latter utilizing synthetically generated weather data to extend coverage beyond historically observed conditions and enable extreme event analysis.

An overview of the methodologies and their generated outputs is presented in Figure 26.

Figure 26 – Methodology overview

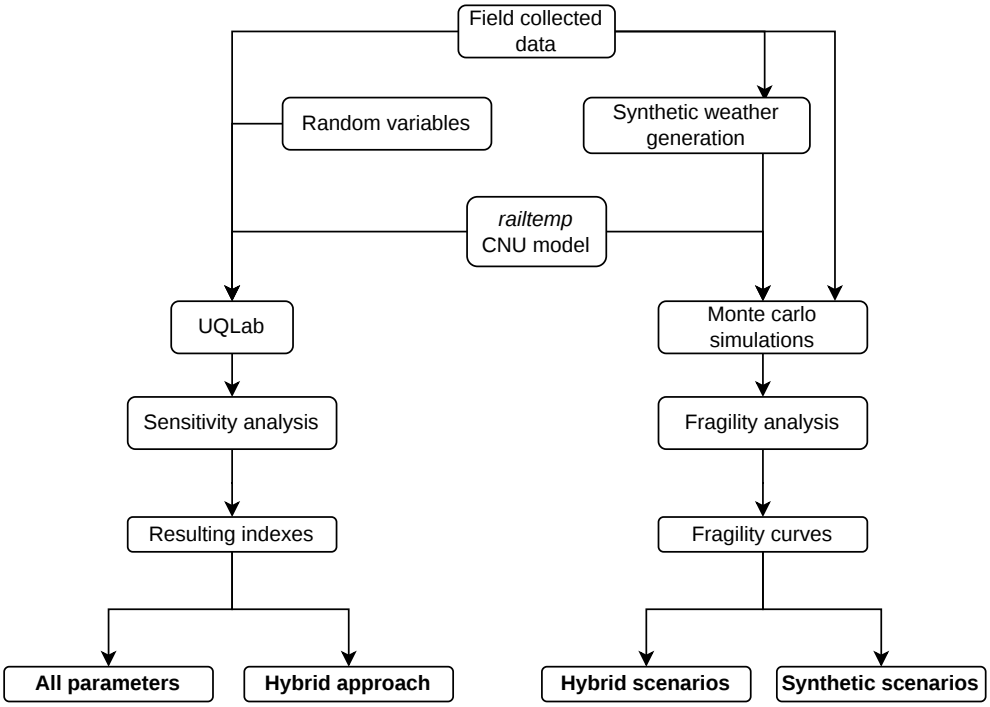

Source: Author (2026)

Field data used throughout this study were collected from a railway line in Mirandela, Portugal (latitude 41.482628, longitude -7.183741), with the rail oriented at an azimuth of 93° and

a UIC54 rail profile. Temporal coverage extends from August 2020 until February 2021, with data being collected at 5 minutes interval, yielding 192 days worth of data. Weather data was collected using a commercial weather station and railway temperature measured using thermocouples connected to a data logger. Further details regarding the data collection process and railway location are provided by Frigeri (2021) and Piloto *et al.* (2022).

Furthermore, tt is important to acknowledge the following methodological limitations:

- The uncertainty of some input parameters is not precisely characterized due to limited experimental data across diverse conditions and scarcity of data in the literature;
- The limited time span of the measured dataset constrains the statistical robustness of the results;
- Weather parameters exhibit mutual dependencies, which are **virtually** captured through independent regression models for each parameter due to it being measured simultaneously. However, synthetic weather data generation process remains independent and stochastic and is constrained to temporal variations based on time of day and month. This approach is discussed in Section 5.1.4.

4 SENSITIVITY ANALYSIS

4.1 Methods

As previously discussed in section 2.5.1, sensitivity analysis is a systematic technique for quantifying how individual input parameters influence model outputs. Given the large number of parameters involved in the rail temperature simulation model, this analysis is essential to identify which inputs most significantly affect the model's predictions. In this study, a global sensitivity analysis was performed using Sobol indices, which are widely adopted for their ability to quantify both individual and interaction (total-order) effects of input variables on output variance. These indices are based on ANOVA decomposition and assume independent input variables, with values ranging from 0 to 1, where higher values indicate greater influence. According to Cannavó (2012), variables can be classified as very important ($0.8 < S_i \leq 1$), important ($0.5 < S_i \leq 0.8$), unimportant ($0.3 < S_i \leq 0.5$), and irrelevant ($0 < S_i \leq 0.3$). The sensitivity analysis was conducted in MATLAB using the UQLab package (Marelli *et al.*, 2022), in conjunction with the MATLAB implementation of the physical model provided by *railtemp*.

To account for the availability of field-collected data and the fact that some parameters can be directly measured, the sensitivity analysis was structured into two main approaches. In the first approach, all model parameters were treated as random variables, involving single-step solutions. This scenario is referred to as **"all parameters"**. In the second approach, actual field measurements were incorporated for key parameters, referred to as **"w/ measured data"**. These approaches are detailed in Sections 4.1.3 and 4.1.4, respectively. As reference, a summary of the input parameters is presented in table 8.

Table 8 – Summary of input parameters for UQLab

Parameter	Description	Parameter	Description
α_s	Solar absorptivity of rail	ϵ	resultant emissivity
$\boldsymbol{SR}$	Solar radiation	$h_{\textbf{conv}}$	Convection coefficient
A_s	Area of rail subject to incoming radiation	ρ	Rail density
A_r	Area of rail subject to radiation heat transfer	C	Specific heat of rail
A_c	Area subject to convection	V	Volume of rail segment
$T_{\textbf{sky}}$	Atmospheric sky temperature	$T_{\textbf{air}}$	Ambient air temperature

Source: Author (2026)

To enable these analyses, two preliminary steps are required. First, the *railtemp* model must be reimplemented in MATLAB to ensure compatibility with UQLab, as presented in Section 4.1.2. Second, model parameters must be characterized as random variables with known statistical distributions, which is a prerequisite for UQLab to perform sensitivity analysis. This statistical modeling is discussed in Section 4.1.5.

4.1.1 Considerations on UQLab

UQLab is a powerful toolbox that offers not only sensitivity analysis but a comprehensive suite of reliability analysis methods. Its modular architecture allows different modules to be chained together to perform various types of analysis. Specifically for sensitivity analysis, the *Input Module* must be used to define parameters using built-in statistical distributions, along with their details depending on the chosen model. After defining all parameters as inputs, these can be passed to the *sensitivity module,* where many options are available, including Sobol indices, Morris methods and others. For this work, Sobol and global sensitivity methods are employed.

Source code 1 demonstrates how UQLab can be used through a code snippet. The typical workflow is as follows: create a model object (line 2), where a MATLAB file is provided as input containing a function definition that takes an array **X** as argument. The length of the array must match the number of *InputOpts* objects defined in line 6. It is important to note that UQLab may use different notations and inputs for common statistical distributions; therefore, it is necessary to provide the inputs accordingly. The user manual (Marelli *et al.*, 2022) describes all formal definitions and this is discussed also in section 4.1.5. Thus, at line 13, calculations are performed to match the expected inputs for the Gamma distribution in this case. Lastly, the analysis type is defined (line 21) along with its parameters, and the analysis is executed (line 26).

Source Code 1 – Example of a UQLab input and sensitivity analysis modules

```
1  % Create a MODEL object from the function file:
2  ModelOpts.mFile = 'railtemp_all_wrapper';
3
4  myModel = uq_createModel(ModelOpts);
5  ii=1;
6  InputOpts.Marginals(ii).Name = 'SA';
7  InputOpts.Marginals(ii).Type = 'Beta';
8  InputOpts.Marginals(ii).Parameters = [5 2 0 1];
9
10 ii=2;
11 InputOpts.Marginals(ii).Name = 'SR';
12 a=0.9414; b=312.4924;
13 k=a; g=a/b; %g=0.003 %k=0.9414
14 InputOpts.Marginals(ii).Type = 'Gamma';
15 InputOpts.Marginals(ii).Parameters = [g k];
16 InputOpts.Marginals(ii).Bounds = [0 1100];
17
18 % Create an INPUT object based on the specified marginals:
19 myInput = uq_createInput(InputOpts);
20
21 SobolOpts.Type = 'Sensitivity';
22 SobolOpts.Method = 'Sobol';
23 SobolOpts.Display = 'verbose';
24 SobolOpts.Sobol.Order = 2;
25 SobolOpts.Sobol.SampleSize = 1e4;
26 SobolAnalysis = uq_createAnalysis(SobolOpts);
27
```

Source: Author (2026)

4.1.2 MATLAB implementation and validation

To enable sensitivity analysis using the UQLab package, the CNU model employed in *railtemp* (see Eq. 9 and Section 2.3.2) was reimplemented as MATLAB functions. This MATLAB implementation was then validated against the original *railtemp* Python package to ensure computational equivalence. Minor numerical differences between implementations are expected due to variations in the underlying mathematical solvers used by Python and MATLAB.

Two validation approaches were adopted: single-step and continuous. The single-step validation compares individual time-step solutions with a fixed 300-second interval. All parameters were held constant except the initial rail temperature, which was randomly sampled from $20\,^{\circ}\mathrm{C}$ to $50\,^{\circ}\mathrm{C}$. This approach comprised 1000 independent simulations to assess solver consistency.

The continuous validation evaluates model performance over extended periods using field-collected weather data. This approach mimics typical *railtemp* usage: given a day's worth of measured weather conditions (wind velocity, solar radiation, and ambient temperature) along with defined material, geometry, and geographical parameters, the model predicts rail temperature evolution. The validation dataset contains 17 hours of measurements at 5-minute intervals, with the initial rail temperature randomly sampled for each simulation. A total of 100 continuous simulations were conducted.

One important distinction between the implementations should be noted: while the *railtemp* package offers the flexibility to either dynamically calculate the rail surface area exposed to solar radiation (A_s) based on sun position or use a fixed value, the MATLAB implementation uses only a fixed A_s value. Since the objective is sensitivity analysis rather than model validation, this simplification is assumed. Consequently, for consistency during validation, both implementations were configured to use a constant A_s parameter.

The results are discussed in section 4.2.1

4.1.3 All parameters analysis

In this analysis, all model parameters (see Tab. 8) are treated as random inputs, with calculations performed for a single time step following the same approach as the single-step validation described in Section 4.1.2. This analysis aims to identify the most influential model parameters under the assumption that no field measurements are available, representing a scenario where all inputs must be estimated from their respective uncertainty distributions.

The analysis was configured with a time step interval of 300 seconds and an initial rail temperature of $30\,^{\circ}\mathrm{C}$. Sobol indices up to second order were computed using 1×10^4 samples, a sample size selected to balance computational cost with the number of input parameters and the desired analysis order. The specific input parameter distributions and corresponding results are presented in Section 4.2.2.

4.1.4 Hybrid approach using measured data: **"w/ measured data"**

In this approach, actual field measurements are incorporated into the analysis and are therefore not modeled as random inputs as in the previous approach. These parameters include solar radiation (*SR*), wind speed (w_s), and ambient temperature (T_{air}). The wind speed is used to calculate the convection coefficient (h_{conv}) using Eq. 10. All other parameters remain defined as random inputs.

Unlike the previous analysis, which solved single time steps to estimate the Sobol indices, this approach simulates an entire day (from 5:00 to 22:00) and uses the maximum simulated rail temperature for the day (T_{rail}) as the output for UQLab to estimate the model sensitivity. The time step between each data point remains 300 seconds. This approach provides a realistic assessment because weather data are readily measurable, thereby eliminating their variability from the sensitivity analysis and enabling identification of which other parameters exert significant influence beyond those that can be easily measured. Specific parameter distributions and corresponding results are presented in Section 4.2.2.

4.1.5 Modeling input random variables for sensitivity analysis

The statistical distribution notation used throughout this work follows UQLab conventions, which may differ from other sources. These differences are purely notational. Below are the notations for common distributions employed in this study:

- Beta: $\mathrm{Beta}(\alpha\colon 5.0, \beta\colon 2.0, [0\ \ 1])$;
- Gamma: $\mathrm{Gamma}(\lambda\colon 0.0030, k\colon 0.9414, [0\ \ 1100])$;
- Weibull: $\mathrm{Weibull}(a\colon 0.1540, b\colon 5.4147, [0\ \ 0.19])$;
- Normal: $\mathcal{N}(\mu\colon 7850, \sigma^2\colon 78.5)$;
- Clipped-normal: $\mathcal{N}(\mu\colon 0.43046, \sigma^2\colon 0.05, [0\ \ 0.43046])$;
- Log-normal: $\mathcal{LN}(\lambda\colon 5.6643, \zeta\colon 0.0312, [\ \ ])$;
- Uniform: $\mathcal{U}(a\colon 439, b\colon 487)$.

Note that UQLab allows the specification of hard bounds even for distributions that typically have infinite support, denoted using bracket notation $[min\ max]$, making them truncated distributions.

Accurately characterizing model parameter behavior is challenging without extensive experimental data across diverse conditions. Therefore, the probabilistic models used in this present work are approximations informed by available literature where possible, or based on engineering judgment when empirical data are unavailable. This section explains the approaches for determining the statistical modeling of the parameters listed in Table 8 and Table 9.

The convection coefficient (h_{conv}), ambient air temperature (T_{air}), and solar radiation (*SR*) were modeled using their best-fit distributions derived from 192 days of field measurements collected at 5-minute intervals, as described by Frigeri (2021). These distributions are used for the **"all-parameters"**. These parameters exhibit significant variability depending on season, location, and geographical position. However, modeling them using measured data from a specific location provides the necessary spread and randomness for the analysis, while inherently introducing some bias due to the site-specific nature of the collected data. This limitation should be acknowledged when interpreting the results.

Dynamically determining the solar absorption area (A_s) represents a key advancement of the CNU model as implemented in the *railtemp* package, which calculates this parameter based on sun position, rail geolocation, and orientation. However, for the sensitivity analysis requiring a statistical representation, A_s was modeled by fitting a distribution to data calculated using the *railtemp* package, considering the same railway location and rail orientation specified by Piloto *et al.* (2022) over the period of 192 days, covering a good range of solar variation across different seasons.

Regarding geometrically constrained parameters, such as the areas subject to convection (A_c) and radiation (A_r), these are bounded by the geometric properties of the rail profile. These parameters have values equivalent to the length of the profile cross-section excluding the bottom (see Fig. 2). Therefore, they are modeled using half-normal distributions to reflect these geometric constraints, ensuring that they cannot exceed physically permissible values.

The specific heat of the rail material (C) is represented by a uniform distribution with bounds based on values for temperatures between $0\,^{\circ}$C to $60\,^{\circ}$C provided by Frigeri (2021).

The solar absorptivity coefficient is modeled using a gamma distribution following typical values reported by Zhang and Lee (2008–Nineteenth century), Hong *et al.* (2019b), Joint Commitee On Structural Safety (2001) and Lichte (2004). The gamma distribution is particularly suitable for this coefficient since it naturally constrains values between 0 and 1. Similarly, the emissivity (ϵ) is modeled as the combination of two beta distributions, namely the ambient emissivity (ϵ_{amb}) and the rail emissivity (ϵ_{rail}). Finally, rail density (ρ) and volume (V) are modeled using normal distributions with $10\,\%$ coefficients of variation around typical values for steel.

The specific parameter values and distributions adopted for this analysis are presented in Section 4.2 alongside the corresponding results.

4.2 Results

4.2.1 MATLAB validation

The single-step validation results are presented in Figure 27. Figure 27a illustrates that most error values fall between 2.0×10^{-3} and 3.0×10^{-3}, with an average (μ) of 2.6×10^{-3}. Additionally, Figure 27b demonstrates the distribution of errors across the simulation run number, highlighting a random spread of data points throughout the simulation runs.

Figure 27 – Validation results for single step solutions

(a) Histogram of errors

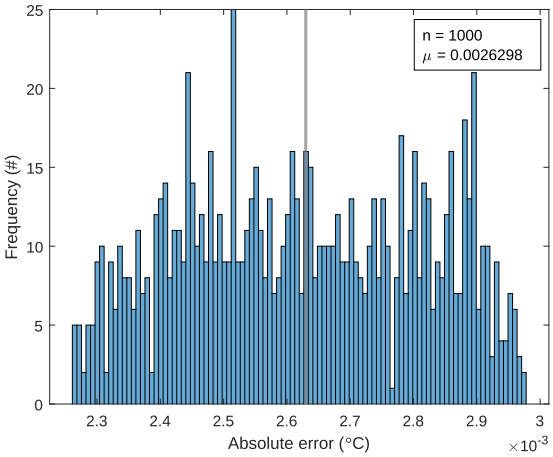

(b) Scatter plot of absolute errors

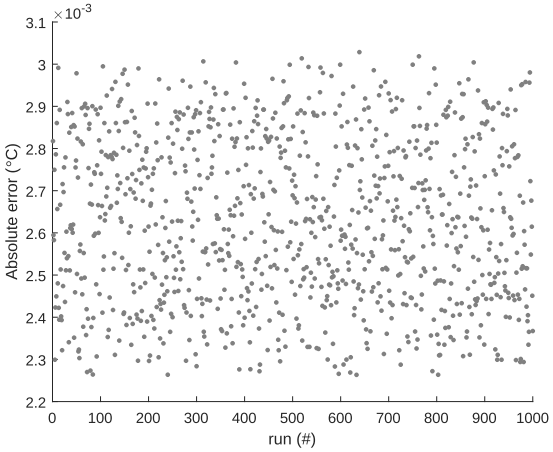

Source: Author (2026)

The single-day validation results are illustrated in Figure 28. The histogram (Fig. 28a) of the absolute errors shows a highly skewed distribution to the right, with a large concentration of low-error instances and few higher-error outliers, demonstrating that both MATLAB and the Python package are in accordance. The average absolute error for the continuous validation is within an acceptable value of $4.0 \times 10^{-2}\,^{\circ}$C. Figure 28b shows the error distribution along the simulation time for all runs.

Figure 28 – Validation results for continuous validation (single day) solutions

(a) Histogram of errors

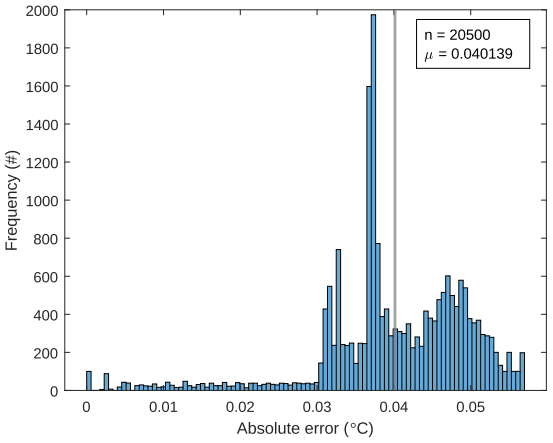

(b) Scatter plot of absolute errors over simulation time

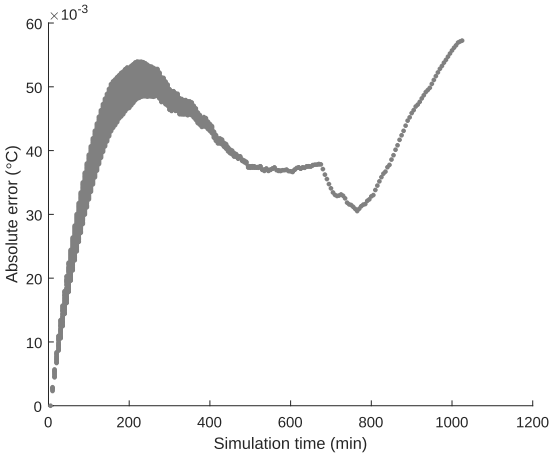

Source: Author (2026)

These validation results demonstrate that the MATLAB implementation achieves computational equivalence with the *railtemp* Python package. The low average errors observed in both single-step (2.6×10^{-3}) and continuous validation ($4.0 \times 10^{-2}\,^{\circ}$C) confirm that both implementations solve the underlying energy balance model consistently, despite differences in their numerical solvers. This equivalence establishes confidence in using the MATLAB imple-

mentation with UQLab for sensitivity analysis, ensuring that the sensitivity indices calculated will accurately reflect the behavior of the original *railtemp* model.

4.2.2 Parameters analysis

This section discusses the results of the parameter analysis following the methods described in Section 4.1. In addition to the two approaches mentioned (**"all parameters"** and **"w/ measured data"**). The results are presented below.

The modeled analysis, employs the methods described in Section 4.1.5 to characterize the sensitivity of the input parameters using their respective statistical distributions. The input parameters for the distributions and their types are presented in Table 9. Figure 29 shows the histograms extracted from UQLab for each parameter input. The physical units for the numeric values of the distributions follows the ones explained in Section 2.3.2, in Equations 9 and 10.

Note that the emissivity (ϵ) is obtained as the combined distribution of the following:

- ϵ_{rail}: $\mathrm{Beta}(\alpha\colon 14.7, \beta\colon 6.3, [0\ \ 1])$;
- ϵ_{amb}: $\mathrm{Beta}(\alpha\colon 14.4, \beta\colon 9.6, [0\ \ 1])$.

Table 9 – Modelled parameters distributions for UQLab

Param.	Definition	Param.	Definition
α_s	$\mathrm{Beta}(\alpha\colon 5.0, \beta\colon 2.0, [0\ \ 1])$	ϵ	$\mathrm{Beta}(\alpha\colon 12.0246, \beta\colon 16.6057, [0\ \ 1])$
SR	$\mathrm{Gamma}(\lambda\colon 0.0030, k\colon 0.9414, [0\ \ 1100])$	A_r	$\mathcal{N}(\mu\colon 0.43046, \sigma^2\colon 0.05, [0\ \ 0.43046])$
A_s	$\mathrm{Weibull}(a\colon 0.1540, b\colon 5.4147, [0\ \ 0.19])$	ρ	$\mathcal{N}(\mu\colon 7850, \sigma^2\colon 78.5)$
$h_{\textbf{conv}}$	$\mathrm{Gamma}(\lambda\colon 0.1409, k\colon 0.9110, [\ ])$	C	$\mathcal{U}(a\colon 439, b\colon 487)$
A_c	$\mathcal{N}(\mu\colon 0.43046, \sigma^2\colon 0.05, [0\ \ 0.43046])$	V	$\mathcal{N}(\mu\colon 7.16\times10^{-3}, \sigma^2\colon 0.0716\times10^{-3})$
$T_{\textbf{sky}}$	$\mathcal{LN}(\lambda\colon 5.6643, \zeta\colon 0.0312, [\ ])$	$T_{\textbf{air}}$	$\mathcal{LN}(\lambda\colon 5.6643, \zeta\colon 0.0312, [\ ])$

Source: Author (2026)

The Morris method, also known as the Elementary Effects method, evaluates parameter importance using two metrics: μ^*, the mean absolute elementary effect, and σ, the standard deviation of the elementary effects. The former quantifies the overall influence of a parameter on the model output, whereas the latter reflects interactions with other parameters and possible nonlinear effects. Figure 30 presents these Morris sensitivity indices for the model parameters.

The Morris analysis reveals that the solar absorption area (A_s) exhibits the highest μ^* value (39.669), confirming it as the most influential parameter when weather conditions are held constant. This is followed by the convection area (A_c) with $\mu^* = 24.556$ and the radiation area (A_r) with $\mu^* = 12.311$. The solar absorptivity coefficient (α_s) shows moderate influence ($\mu^* = 5.025$), while material properties such as density (ρ), specific heat (C), and volume (V) demonstrate negligible effects ($\mu^* < 0.35$).

In addition, Figure 31 summarizes the total Sobol indices provided by the UQLab module for the input parameters discussed in this section. Analysis of Figure 31a reveals clusters of

Figure 29 – Input parameter distributions used in the modeled sensitivity analysis

(a) Solar absorptivity (α_s)

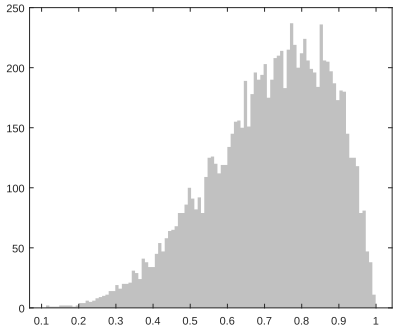

(b) Emissivity (ϵ)

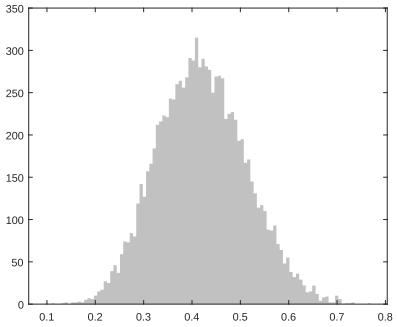

(c) Solar radiation (*SR*)

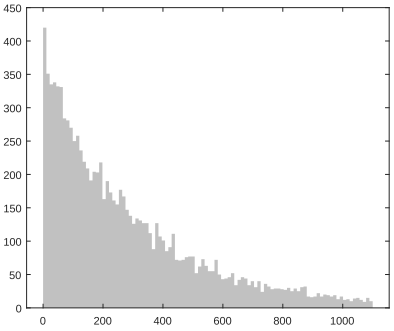

(d) Radiation area (A_r)

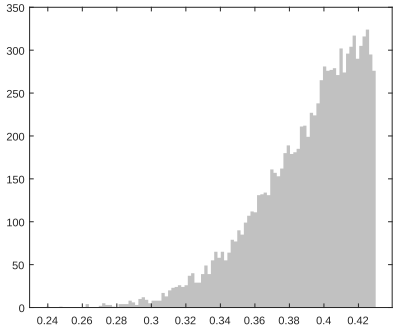

(e) Solar absorption area (A_s)

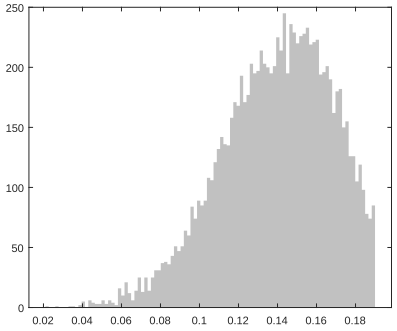

(f) Density (ρ)

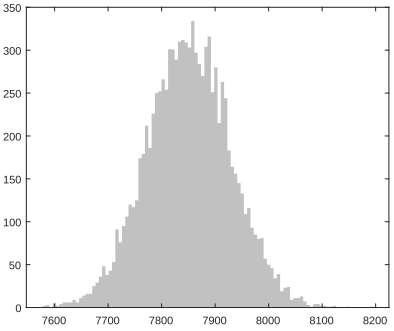

(g) Convection coefficient (h_{conv})

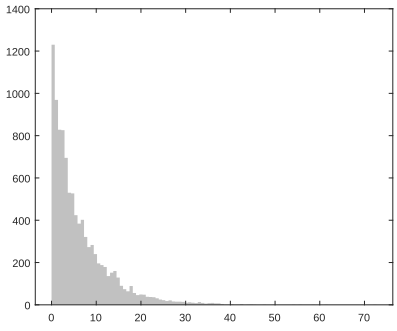

(h) Specific heat (C)

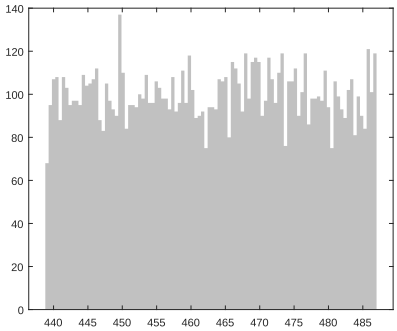

(i) Convection area (A_c)

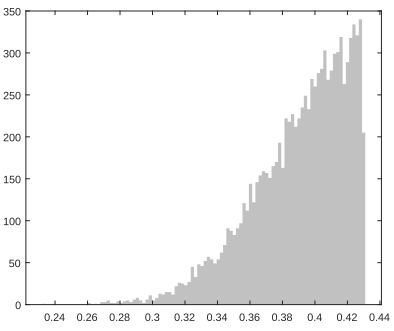

(j) Volume (V)

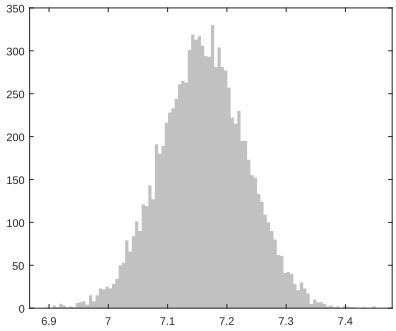

(k) Sky temperature (T_{sky})

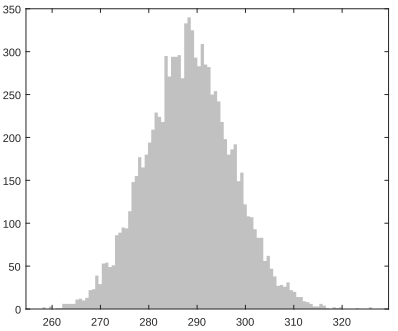

(l) Ambient temperature (T_{air})

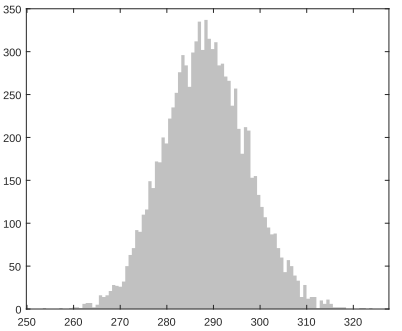

Source: Author (2026)

Figure 30 – Morris elementary analysis for **"w/ measured data"**

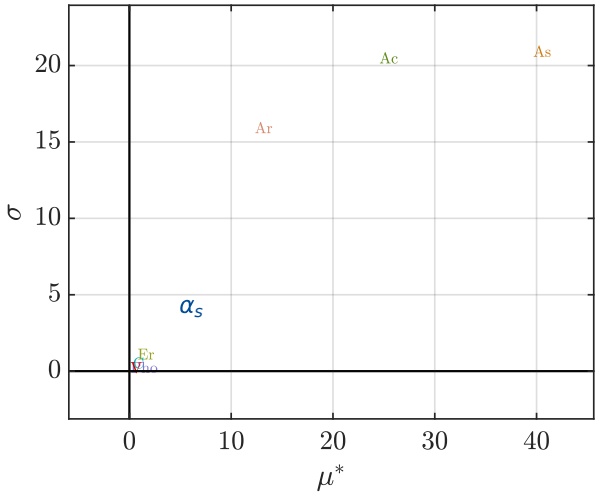

Source: Author (2026)

influential parameters. When varying all model parameters, the ones with the highest impact according to the Sobol indices are the convection coefficient (h_{conv}), ambient temperature (T_{air}), and incoming solar radiation (*SR*). This result indicates that convective heat exchange (first term of Eq. 9) exerts the strongest influence on rail temperature, followed by solar radiation absorption (second term of Eq. 9).

Figure 31 – Sobol sensitivity analysis results

(a) All Parameters

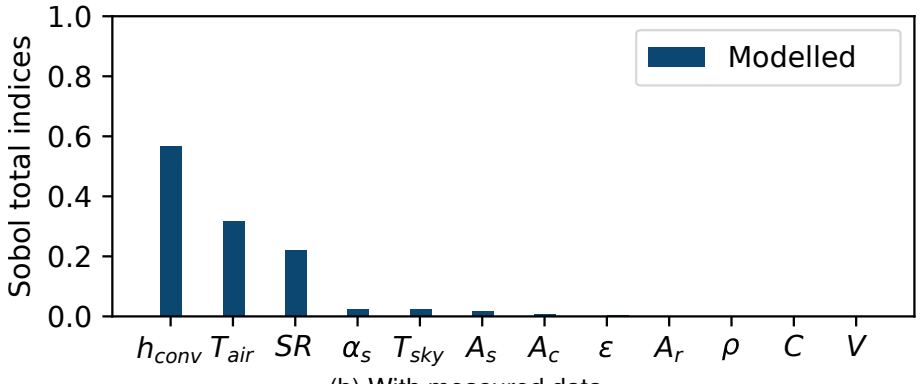

(b) With measured data

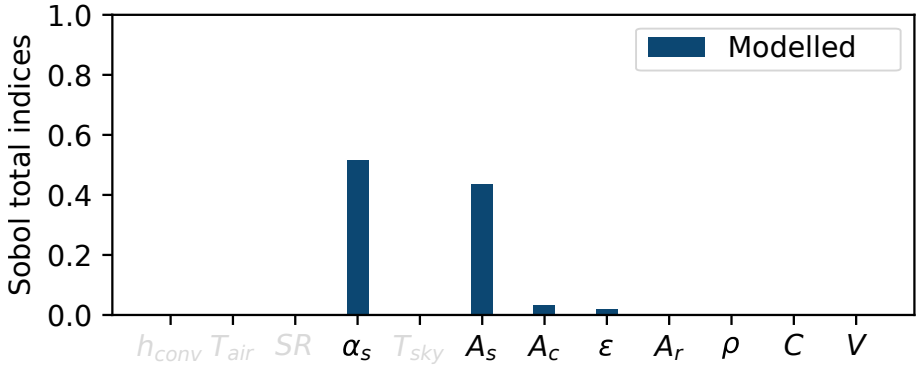

Source: Author (2026)

By excluding the readily measurable parameters from the analysis (h_{conv}, T_{air}, *SR*, and T_{sky}), the relative impact of the remaining variables becomes more apparent. This is illustrated in Figure 31b. Beyond the previously mentioned parameters, the other factors influencing the model are, in descending order of importance: the solar absorption coefficient of the rail material (α_s), the solar absorption area (A_s), and the convection exchange area (A_c). This analysis confirms that the second most influential heat exchange mode is solar radiation absorption. These findings support the improvements made by Hong *et al.* (2019b) and Piloto *et al.* (2022), who enhanced the estimation of A_s by making it time- and location-dependent, which is justified given its high influence when readily measurable weather parameters are excluded from the sensitivity analysis.

The σ values provide insight into parameter behavior. The high σ values for A_s (20.822), A_c (20.390), and A_r (15.822) indicate significant interaction effects or nonlinear behavior, suggesting that their influence varies depending on the values of other parameters. In contrast, material properties exhibit low σ values, indicating consistent, primarily linear effects across the parameter space.

Morris' indexes corroborate the Sobol analysis results and emphasize that geometric parameters related to heat exchange surface areas exert the most significant influence on rail temperature predictions. The Morris method efficiently identifies A_s, A_c, and A_r as critical parameters requiring careful characterization, while confirming that uncertainties in material properties have minimal impact on model predictions.

Meanwhile, following the classification suggested by Cannavó (2012) (see Section 4.2), using the sobol analysis in a scenario where weather data can be easily measured, the parameters α_s and A_s can be considered **important**, while all others are **irrelevant**.

In summary, given a scenario where weather parameters are easily measurable and reliable with standard equipment, both sensitivity analyses consistently demonstrate that focusing on improving the estimation of parameters related to incoming solar radiation absorption (A_s and α_s) and convective heat exchange surface areas can enhance the overall accuracy of the model.

Conversely, when analyzing the sensitivity of **all parameters** (Fig. 31a), the convection coefficient (h_{conv}) emerges as the most influential parameter in the model. This coefficient is derived from Eq. 10, which itself constitutes a sub-model that estimates the coefficient based on wind velocity measurements. The previous findings confirm that convective heat transfer plays a crucial role in rail temperature prediction and suggests that refining the convection coefficient estimation could yield substantial improvements in model accuracy.

5 FRAGILITY ANALYSIS

5.1 Methods

The purpose of the Monte Carlo simulation, in the context of this work, is to provide a statistical perspective on the potential outcomes of rail temperature, accounting for the stochastic nature of the input parameters as defined in Section 4.1. This simulation technique enables estimation of the probability that rail temperature will, in this situation, **reach** or **exceed** specific critical thresholds. For example, in the context of buckling analysis (refer to Section 2.4), this phenomenon may occur when temperatures reach or exceed the range $50\,°\text{C}$ to $60\,°\text{C}$, depending strongly on track conditions such as geometric deviations and ballast maintenance (Piloto; Frigeri; Minhoto, 2022).

This section presents two main approaches: **hybrid** and **synthetic**, which are discussed in detail in Sections 5.1.2 and 5.1.3, respectively. Briefly, the first approach uses collected weather data combined with the modeled random inputs from Section 4.1.5, executes thousands of simulations, and then calculates probabilities from the results. The second approach extends this by using synthetic weather data (including weather data) and executing thousands of simulations to calculate the same metrics.

The primary metric targeted in this analysis is the probability that rail temperature (T_{rail}) potentially reaches or exceeds a given threshold in a specific scenario. These threshold probabilities are denoted as *P* values; for instance, *P60* represents the probability that the model predicts a rail temperature equal to or greater than $60\,°\text{C}$. This probability can be calculated by counting the number of simulations (also referred to as unique variations or simulation runs) in which the rail temperature equals or exceeds the threshold and dividing it by the total number of simulations. This approach is already useful counting scenarios regardless of any other variable condition, however, it is also useful to correlate this probability with another parameter and compute a conditional probability, in this case based on the ambient air temperature (T_{air}), which will be denoted as intensity parameter.

Equation 26 defines the conditional probability of the rail temperature in respect to ambient air temperature. The analysis consists of three steps. First, it filters simulation runs where the maximum ambient air temperature satisfies $T_{\text{air}}^{\text{max}} \in B_i$, establishing a subset of N simulations from the total dataset, where B_i is defined as $B_i = [T_{\text{air},i}^{\text{central}} - \Delta, T_{\text{air},i}^{\text{central}} + \Delta]$, representing a discrete temperature bin centered at $T_{\text{air},i}^{\text{central}}$. The Δ is set to $1\,°\text{C}$.

Second, for each simulation run i within this subset (N), the maximum rail temperature $T_{\text{rail},i}^{\text{max}}$ is extracted (simulation result is aggregated by the maximum daily value). Lastly, the conditional probability is then computed as the ratio of the number of simulations where $T_{\text{rail},i}^{\text{max}} \geq T_{\text{rail}}^{\text{threshold}}$ is satisfied, to the total number of filtered simulations N.

This metric quantifies the likelihood that rail temperature will reach or exceed a critical threshold given that the maximum daily ambient temperature is inside the bin interval. The maximum daily ambient air temperature is taken as the environmental intensity measure, in terms of

which the probability of the rail buckling is calculated. The aforementioned approach is referred to as the **bin probability**.

$$P\left(T_{\text{rail}}^{\text{max}} \geq T_{\text{rail}}^{\text{threshold}} \mid T_{\text{air}}^{\text{max}} \in B_i\right) = \frac{\#\left\{T_{\text{rail}}^{\text{max}} \geq T_{\text{rail}}^{\text{threshold}}\right\}}{\#\left\{T_{\text{air}}^{\text{max}} \in B_i\right\}} \tag{26}$$

5.1.1 Enabling *railtemp* package for Monte Carlo simulations

The *railtemp* package originally lacked **native** support for Monte Carlo simulations, accepting only constant numerical values for material and rail properties rather than random parameters sampled from statistical distributions. While manual loop-based approaches could handle parameter variations and object creation, such implementations would be cumbersome for large-scale analyses. To address this limitation and facilitate execution of thousands of simulations efficiently, the package was extended to support parameters defined as statistical distributions and to provide a *Montecarlo* object for managing simulation configurations. These enhancements have been made publicly available[1], with a usage example provided in Appendix A.1.

Figure 32 presents the extended class diagram of the package, including class relations and key attributes and methods. Classes with gray background represent the additions introduced in the new version. The *AbstractParameterValue* class serves as an abstraction for all parameter values, whether constant or random, and is the expected value type for classes such as *RailMaterial* and *Rail*. As an abstract class, it requires concrete implementations, which are satisfied by the *ConstantParameterValue* class and all statistical distribution wrapper classes through inheritance. It is worth noting that the statistical distribution classes utilize *scipy.stats* as the underlying distribution provider (SciPy 1.0 Contributors *et al.*, 2020). These modifications preserve backward compatibility by continuing to accept constant values (integers or floats) as input, which were the only available options previously, while extending functionality to support random values. Furthermore, custom distributions can be implemented by inheriting from the *RandomParameterValue* class.

5.1.2 Hybrid approach: using collected data

This approach combines field-measured weather data with randomly sampled model parameters (specific distributions are discussed in Section 4.2.2). Each simulation covers a single day from 5:00 to 20:00 using a time step of $15\,\text{min}$. This larger time step, compared to previous analyses, enables a greater number of parameter variations (increasing the number of simulations) while maintaining comparable computational cost. The simulation initialization at 5:00 exploits thermal equilibrium conditions typically observed in the early morning, where convection is virtually the only heat transfer mode, allowing the assumption that rail temperature (T_{rail}) and ambient air temperature (T_{air}) are approximately equal. This initial rail temperature serves

[1] https://github.com/aryvini/railtemp

Figure 32 – Extended class diagram for *railtemp* package

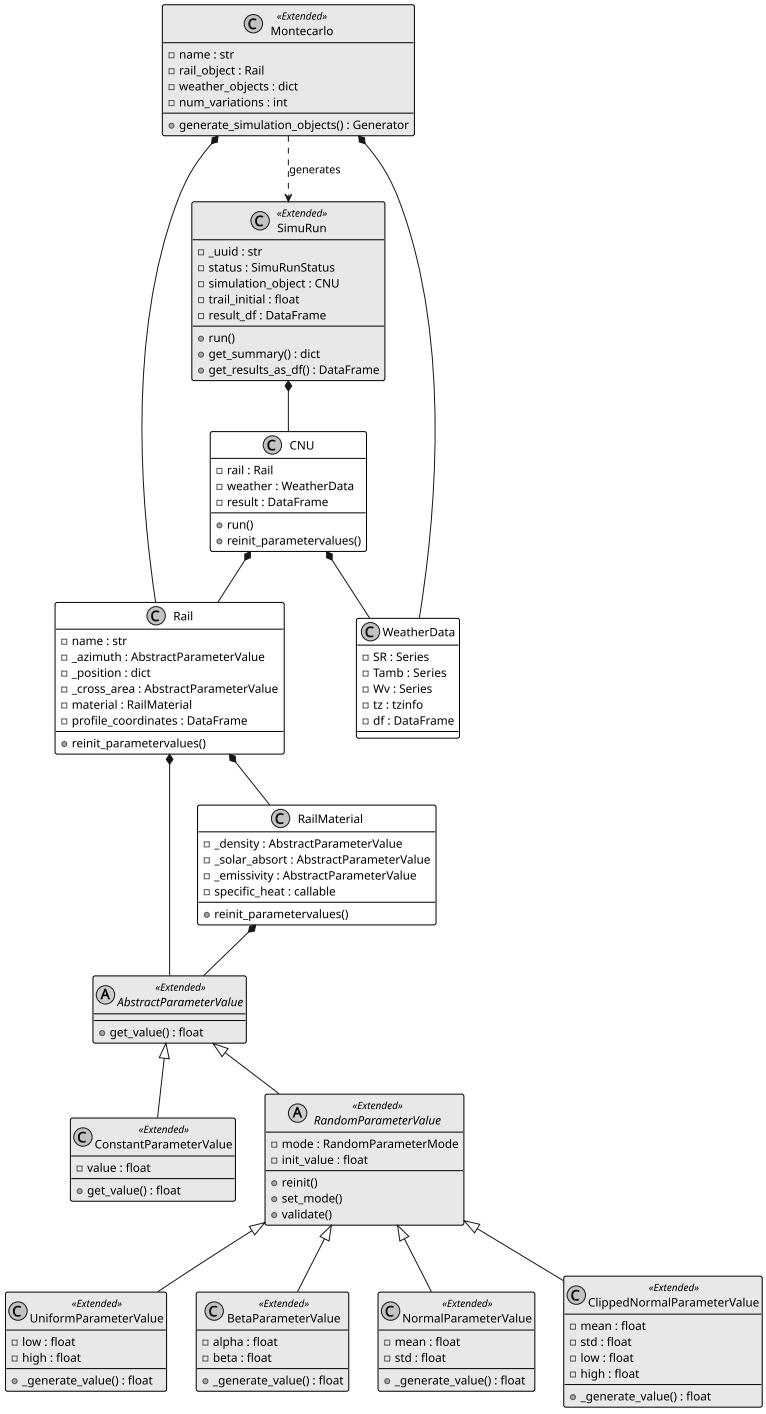

Source: Author (2026)

as the starting condition for the numerical solver to compute subsequent time steps. Empirical data from Piloto *et al.* (2022) support this equilibrium assumption for the chosen initialization time. In total, 192 days of collected weather data are simulated with every single day having 500 variations, spanning from July to February.

In summary, referring to Equation 9, the following parameters are derived from measured data: solar radiation (*SR*), convection coefficient (h_{conv})—computed using wind speed (w_s) via Equation 10—and ambient air temperature (T_{air}). All other parameters are modeled as random inputs. However, this method is constrained by the weather scenarios present in the measured

dataset. Since no extreme events occurred during the measurement period, estimating probabilities (*P* values) for such conditions is limited. Consequently, the following approach treats all inputs as random variables and employs synthetically generated weather data.

5.1.3 Synthetic approach: using generated weather data

In this approach, field-measured weather data are replaced with synthetically generated weather inputs, while all remaining model parameters are treated as random variables following specified statistical distributions. The primary challenge involves generating synthetic weather data that enables coverage of extreme events not captured in the historical measurement record. The methodology for synthetic weather data generation is discussed in Section 5.1.4. This synthetic approach differs fundamentally from the sensitivity analysis described in Section 4.1.3, where only single time steps were solved in a time-independent manner. In contrast, these Monte Carlo simulations evolve temporally throughout the day, similar to the hybrid approach. Beyond the use of synthetic weather data, two key differences distinguish this approach: the simulation time range and the determination of initial rail temperature (T_{rail}).

The simulation time range is reduced to manage computational costs and analysis duration. While increasing the number of parameter variations improves likelihood estimation accuracy, the combinatorial nature of independent random inputs yields a virtually infinite simulation space. Given finite computational resources, the analysis restricts the time range from 10:00 to 19:00. This reduction in temporal scope decreases the computational effort per simulation, enabling a larger number of unique parameter combinations to be explored. Computational considerations and resource allocation are discussed in Section 5.2.1.

Additionally, the initial rail temperature requires a different treatment compared to the hybrid approach, which assumed thermal equilibrium at the 5:00 start time. At 10:00, rail temperature typically exceeds ambient temperature due to accumulated solar radiation heating throughout the morning. To characterize this initial condition, the analysis leverages historical measured data: for each month, all observed rail temperatures at 10:00 are fitted to a statistical distribution. This distribution model is then sampled to assign initial rail temperature values for each simulation run, capturing the seasonal variability inherent in early-to-mid-morning thermal conditions.

5.1.4 Synthetic weather data generation

Synthetic weather series are generated monthly to extend the range of plausible conditions beyond the measured dataset. To achieve this, measured weather data are aggregated by month and time of day. For each month m and each 15-minute time group t_k ($k = 1, \ldots, K$, with $K = 36$ covering 10:00–19:00), all observations at that specific time are collected. For example, all measurements recorded at 10:00 across all days in a given month are grouped together. Univariate distributions are then fitted to these aggregated values for solar radiation (*SR*), wind

speed (w_s), and ambient temperature (T_{air}). The fitted models are denoted by $\hat{F}_{X,m,k}(\hat{\theta}_{X,m,k})$ for $X \in \{$ *SR*, w_s, T_{air} $\}$, where $\hat{\theta}_{X,m,k}$ represents the estimated parameters at time step t_k.

$$SR_j^{(m)}(t_k) \sim \hat{F}_{\text{SR},m,k}\left(\hat{\theta}_{\text{SR},m,k}\right) \tag{27}$$

$$w_{s_j}^{(m)}(t_k) \sim \hat{F}_{w_s,m,k}\left(\hat{\theta}_{w_s,m,k}\right) \tag{28}$$

$$T_{\text{air},j}^{(m)}(t_k) \sim \hat{F}_{T_{\text{air}},m,k}\left(\hat{\theta}_{T_{\text{air}},m,k}\right) \tag{29}$$

From Equations 27, 28, and 29, for a given month (m) and synthetic day (j), each weather component is independently sampled from its time- and month-specific distribution at a specified confidence interval value, forming a stochastic process. This stochastic generation ensures that each synthetic weather scenario represents a unique realization of the underlying probability distributions. These synthetic data provide diverse weather scenarios, including extreme events absent from the historical record, and serve as inputs to the Monte Carlo simulations explained in Section 5.1.2. This procedure follows Salazar-Peña, Tabares and González-Mancera (2023) for solar radiation and is extended here to the other parameters; the authors also provide a Python package implementing the solar radiation calculations.

For ambient air temperature (T_{air}), a differential approach is adopted: instead of modeling absolute values at each time stamp, the differences between consecutive time groups t_i and t_{i+1} are computed and fitted. This treatment helps maintain smooth and more realistic gradients between time groups.

The candidate distribution families considered are normal, generalized extreme value, Weibull, and gamma. A comparison of the measured and generated dataset is discussed in Section 5.2.3.

The underlying stochastic process samples from each distribution independently, which to some extent excludes correlations between weather parameters. However, by fitting distributions separately for each parameter, time group and month, these correlations are partially captured indirectly through the temporal and seasonal segmentation. A more robust approach that explicitly models inter-parameter correlations could further improve the synthetic data generation.

5.2 Results

5.2.1 Challenges and learnings running Monte Carlo simulations with python

The Monte Carlo analysis described in Section 5.1 requires many simulations across multiple parameter combinations. Executing these simulations within a reasonable timeframe demands substantial computational resources. The first challenge is to distribute the workload across multiple cores in the same machine, which is not achieved automatically when using Python. To accomplish this, one must specify independent tasks so that the scheduler can dele-

gate them to the cores, thus running the simulations in parallel. These tasks should not depend on each other's results. Since each Monte Carlo run must be independent, this challenge is easily solvable with common Python libraries, enabling the parallelization of the whole simulation batch.

However, single machines become insufficient to run numerous simulations; consequently, distributing the workload across a computing cluster further reduces overall execution time. Nevertheless, cluster management and task orchestration are inherently complex; consequently, specialized frameworks are beneficial. This work employs *Ray*, a distributed computing framework that, despite its primary focus on artificial intelligence applications, provides unified scheduling and cluster management capabilities suitable for parallel execution of independent tasks. Additionally, Ray integrates seamlessly with major cloud providers, enabling deployment on either local networks or cloud infrastructure (Moritz *et al.*, 2018).

To evaluate computational efficiency across different cluster configurations, a benchmark study was conducted comparing consumer-grade and cloud-optimized CPUs. Figure 33 shows the remote and local cluster topology. Table 10 presents the results across five configurations, specifying the head and worker node types (W1 and W2), total cluster core count, execution time, and performance for both single and multicore. The results are based on running the same simulations amounting on 1×10^6 processed lines. Three machine types were evaluated: PC (consumer-grade laptop with 4 or 8 cores, serving as the control baseline), n1 (standard cloud instance), and c2d (compute-optimized cloud instance). Cloud instance selections respected provider constraints, for example the maximum count of CPU cores is 32.

Figure 33 – Remote and local clusters diagram

(a) Remote (b) Local

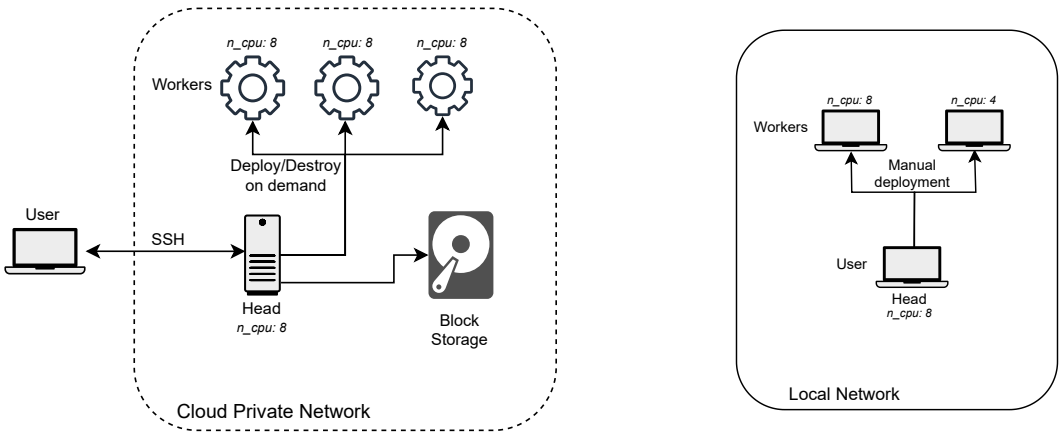

Source: Author (2026)

Analysis of Table 10 reveals that all sets have similar performance on the single core, achieving 40 lines per second per core on average. Comparing set 1 and 2, which are simply a single node and a cluster of 2 nodes of consumer-grade laptops respectively, the improvement

happens on the multicore level, since adding more cores elevates the processing power almost linearly.

Table 10 – Benchmark of Monte Carlo simulation on different cluster configurations

Set	Head		W1		W2		Cores	Duration	Performance (lines/second)	
	type	cores	type	cores	type	cores		(hh:mm:ss)	Single core	Multi core
1	PC	8	-	-	-	-	8	00:55:42	37	299
2	PC	8	PC	4	-	-	12	00:37:44	37	442
3	c2d	16	c2d	16	-	-	32	00:12:58	40	1284
4	n1	8	c2d	12	c2d	12	32	00:12:46	41	1305
5	c2d	32	-	-	-	-	32	00:12:19	42	1352

Source: Author (2026)

Sets 3 to 5 are cloud setups, with a total of 32 cores, differentiating only in head and worker distribution. The idea was to test whether splitting the workload across different workers would significantly influence the performance, which did not occur. The slight difference might arise from network overhead, since *Ray* needs to distribute task objects across the cluster. When comparing set 5 with sets 3 and 4, we can conclude that processing on a single 32-core machine has the best multicore performance; however, this introduces a single point of failure, meaning that if the machine goes down, the entire simulation will be interrupted. Comparing sets 3 and 4, they differ in head node type. The reason for using a n1 type machine as head and c2d type machines as workers lies in their cost. Based on the fact that the head machine can provision worker machines on demand, and that n-type machines are cheaper, once the simulation stops, the head destroys the workers, thereby reducing costs that would occur even when machines are idle.

Based on this analysis, set 4 was chosen for running the Monte Carlo simulations using cloud providers. It offers good multicore performance and also distributes the workload across different machines, increasing cluster robustness while minimizing costs when workers are not needed.

Based on these observations, Table 11 was created as a reference guide for determining how many simulations are feasible and how much time they would take on each configuration. A standard simulation with 36 input lines was used.

Table 11 – Expected duration (hours) of given simulation count for different set configurations

# Simulations	Configuration Set				
	1	2	3	4	5
10.000	0.33	0.23	0.08	0.08	0.07
100.000	3.34	2.26	0.78	0.77	0.74
1.000.000	33.43	22.64	7.79	7.66	7.40
3.500.000	116.99	79.25	27.25	26.81	25.89

Source: Author (2026)

The primary finding from this benchmark study is that local network clusters composed of consumer-grade machines achieve throughput constrained primarily by aggregate CPU core count, without incurring the internode latency overhead of cloud deployments. Conversely, cloud clusters offer superior scalability: core count can be provisioned on demand, enabling linear increases in simulation throughput. This fundamental trade-off—local clusters optimized for per-core efficiency versus cloud clusters optimized for flexibility and elasticity—should guide infrastructure selection based on workload requirements and resource constraints.

5.2.2 Hybrid approach

Based on the methods described in Section 5.1.2, for each day of available data, a total of 500 variations were generated, with data spanning 192 days. Random values for each parameter were sampled at every time step, using the distributions parameters described in Table 9, except the weather parameters. In total, $96\,000$ simulations were executed using a cloud compute engine, supported by the Python framework *Ray* for parallel task processing as described in Section 5.2.1.

Figure 34 shows the probability of rail temperature reaching or exceeding threshold values, conditioned on the day's maximum ambient air temperature intensity, calculated using Equation 26. Figure 35 shows the simulation histogram and the ambient air temperature bins. Figure 36 displays a sample of 1000 simulated rail temperature trajectories compared with measured rail temperatures for the same day, demonstrating the range of variability introduced by parameter uncertainty.

Figure 34 – Fragility data for hybrid Monte Carlo approach

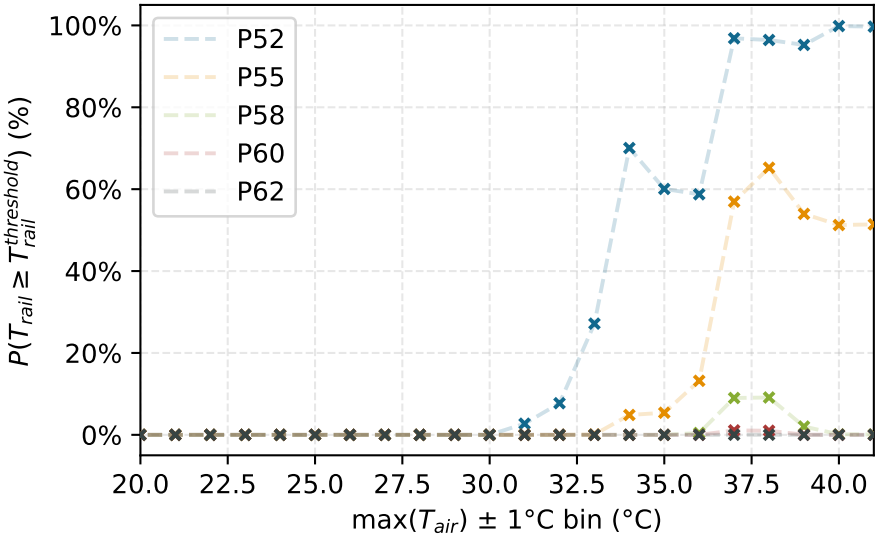

Source: Author (2026)

When interpreting the probabilities shown in Figure 34, it is essential to consider the number of simulations (N) available for each ambient temperature bin ($\max(T_{\text{air}})$ bin) after filtering. As expected, the number of days meeting the conditions decreases with increasing intensity

Figure 35 – Count of simulations for given T_{air}bins

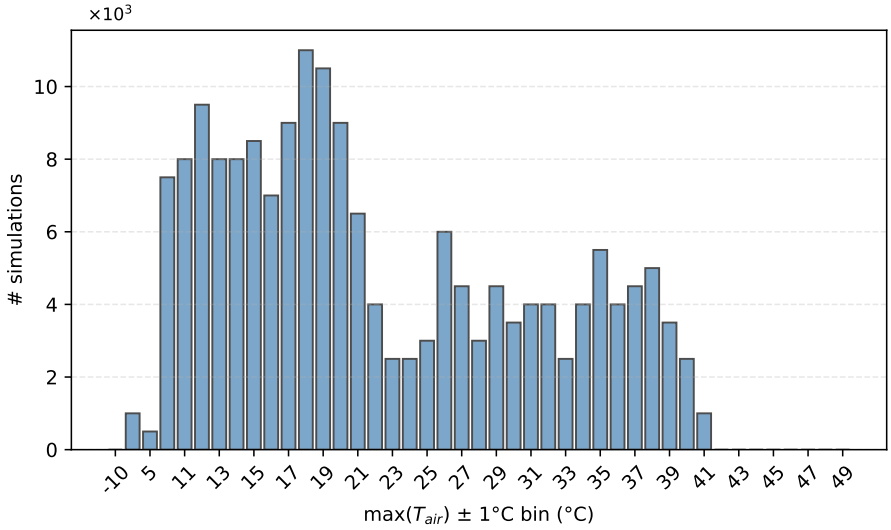

Source: Author (2026)

values. For instance, 18 days fall into the $10\,^{\circ}$C bin, whereas only 11 days on the $35\,^{\circ}$C, 5 days into $40\,^{\circ}$C, and no days ($N = 0$) meet $42\,^{\circ}$C. This non-uniform sample size across bin temperatures directly affects the reliability of estimated *P* values at higher intensities where limited observed data constrains statistical inference. This limitation is addressed by the synthetic approach, discussed in Section 5.2.4. This phenomenon is illustrated in Figure 35, where the count of simulations for each ambient air temperature bin is shown.

Within the available dataset, *P60* reaches a maximum of $1\,\%$ at $38\,^{\circ}$C, representing 50 simulations out of 5000 total simulations from 10 qualifying days. The sharp variation of *P* values at higher ambient temperature thresholds indicates insufficient sample size for robust probability estimation. Similarly, *P55* peaks at $65\,\%$ for $38\,^{\circ}$C ambient temperature before declining to $51\,\%$ at $40\,^{\circ}$C. These fluctuations underscore the sensitivity of failure probability estimates to sample size, particularly when relying exclusively on measured weather data that may not capture extreme conditions.

Figure 36 demonstrates that parameter variability produces a distribution of simulated rail temperatures while generally tracking measured values. Although the simulated temperatures exhibit faster cooling rates compared to field measurements, the model successfully captures peak temperature values, confirming its adequacy for threshold exceeding analysis despite minor discrepancies in temporal evolution. This behavior is also stressed by Piloto *et al.* (2022).

In summary, this approach outputs very conservative results and relies heavily on the input weather data extend. The more diverse the input dataset, more reliable are the probability estimation.

Figure 36 – Sample of simulated and field measured values of rail temperatures for hybrid Monte Carlo approach

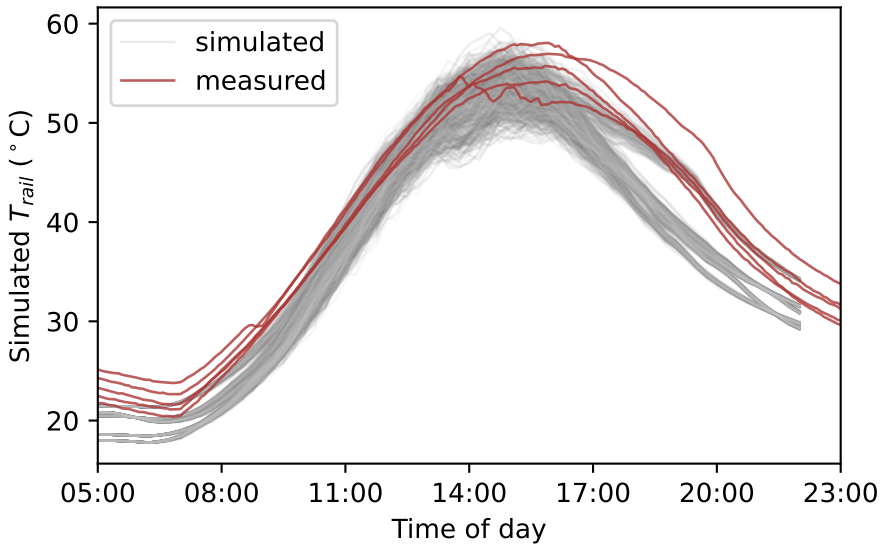

Source: Author (2026)

5.2.3 Synthetic dataset generation

Before analyzing the synthetic Monte Carlo simulation results, it is necessary to validate the synthetically generated weather dataset. Due to insufficient sample size, the months of July and August were merged for distribution fitting, as July contained only 7 days of collected data, inadequate for reliable statistical characterization of an entire month. The synthetic weather data generation follows the methodology described in Section 5.1.4, where distributions are fitted independently for each 15-minute time step and each month to capture temporal and seasonal variations in solar radiation, wind speed, and ambient temperature.

Figures 37, 38, and 39 present histograms comparing measured and synthetic weather parameters for August and September, demonstrating that the generated data preserve the statistical characteristics of the observed measurements while extending the range to include extreme values not present in the historical record. The comparison for all other months can be found in Section B.1.

The generated weather parameters follow the behavior of the collected data, although differences arise due to inherent approximations in the statistical models. Notably, the ambient temperature model (Fig. 37) extends beyond $40\,^{\circ}\mathrm{C}$, which is desirable for rail temperature analysis as it enables the capture and prediction of extreme thermal events not present in the historical dataset. For solar radiation, a noticeable difference appears in the histograms, particularly for August (Fig. 39a). This arises because the generation package (Salazar-Peña; Tabares; González-Mancera, 2023) emulates cloud coverage intensity to cover diverse scenarios, which is not observed in the measured data due to temporal limitations (192 days). This difference represents a broader scenario spectrum rather than a methodological concern. Overall, the syn-

thetic generation methodology preserves statistical characteristics while providing the broader range of conditions necessary for comprehensive probabilistic analysis.

Additionally, Figure 40 presents a time series comparison of generated and measured weather data for August. The synthetic data inherit the temporal behavior of the measured data without producing physically impossible values, particularly in consecutive time steps, demonstrating that the generation methodology maintains temporal coherence.

Figure 37 – Generated and measured ambient temperature distribution by month

(a) August (b) September

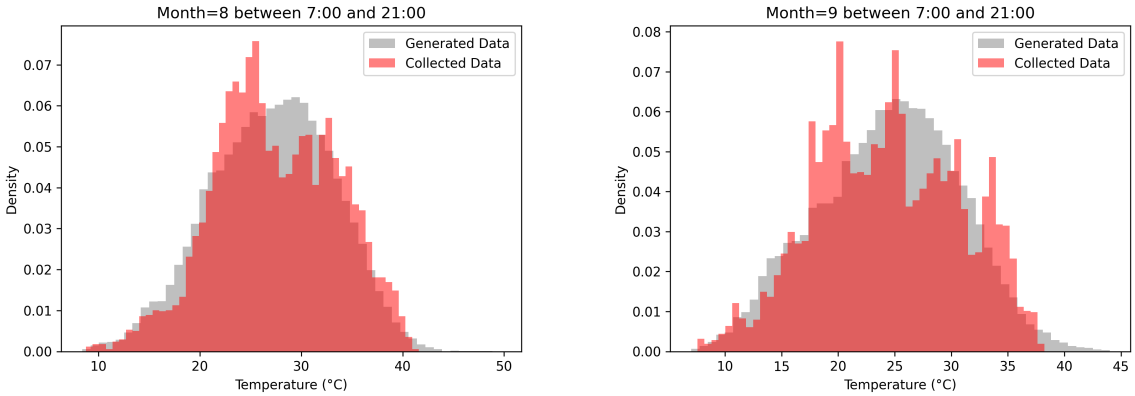

Source: Author (2026)

Figure 38 – Generated and measured wind speed distribution by month

(a) August (b) September

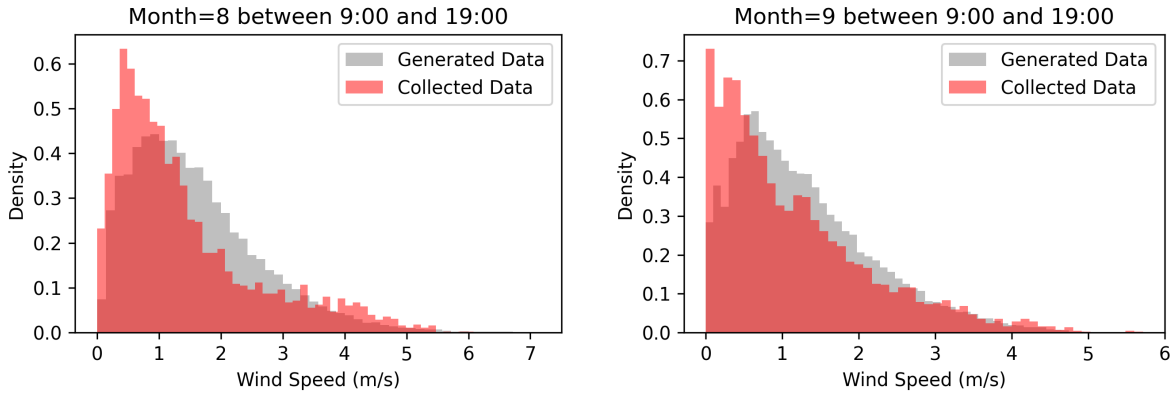

Source: Author (2026)

Figure 39 – Generated and measured solar radiation distribution by month

(a) August (b) September

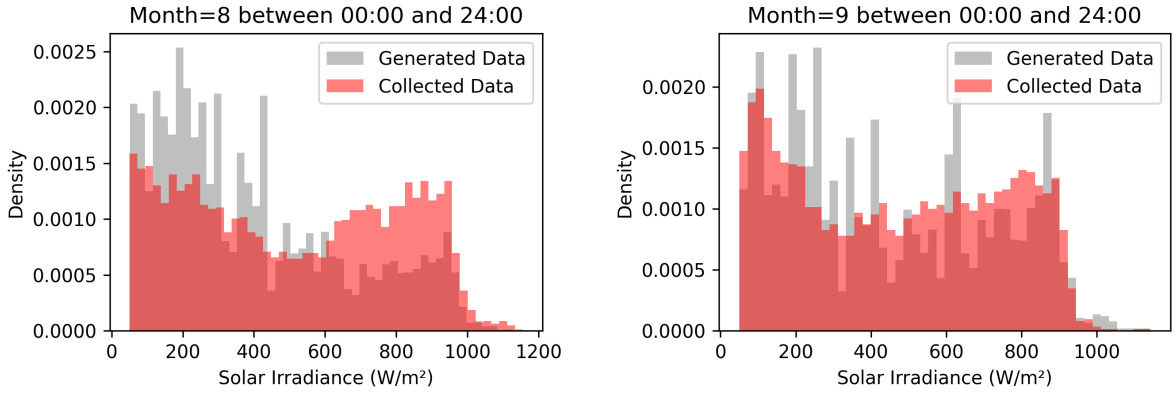

Source: Author (2026)

Figure 40 – Time series of generated and measured weather parameters for August

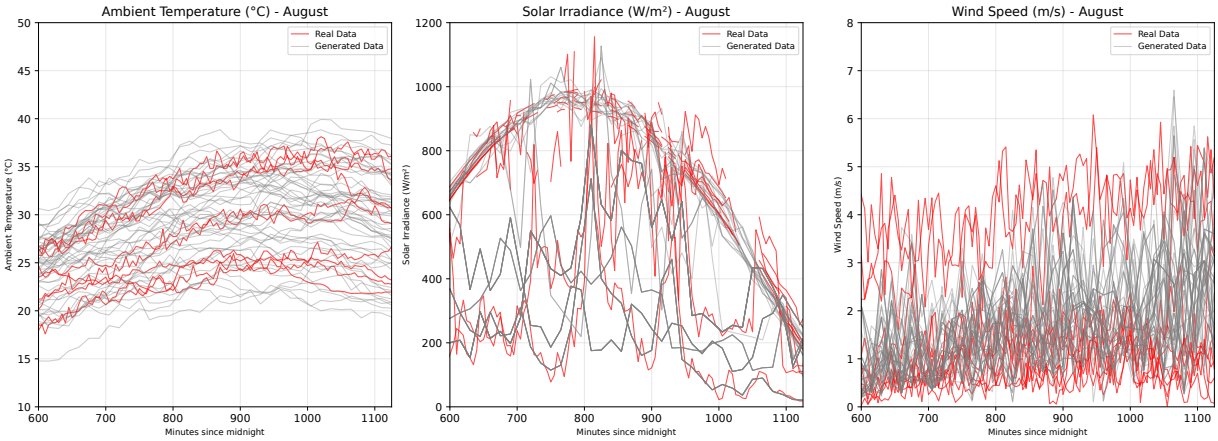

Source: Author (2026)

5.2.4 Synthetic approach

The methodology described in Section 5.1.4 and the generated weather data discussed in Section 5.2.3 enable a fully randomized Monte Carlo simulation approach. By generating synthetic weather data, the analysis can produce extreme events that are not observed in temporally limited measured datasets. Unlike the hybrid approach using measured data, this method imposes no practical limits on simulation quantity. While the hybrid approach can also generate numerous parameter variations, the fixed weather input creates a virtual ceiling where extreme event outcomes are not easily captured. In contrast, the synthetic approach varies both weather scenarios and model parameters simultaneously, with computational cost and synthetic weather generation uncertainty remaining the sole practical limitation.

Based on the computational performance analysis of the Monte Carlo simulations using the *railtemp* package discussed in Section 5.2.1, the present analysis follows the specifications

shown in Table 12. Random values for each parameter were sampled at every time step, using the distributions parameters described in Table 9, except weather parameters, which are generated synthetically. The distribution of simulations across months is deliberately non-uniform. August and September each received $1\,500\,000$ simulations using 3000 synthetic datasets, while the remaining months received fewer simulations ($50\,000$ each) from 1500 synthetic datasets. This allocation prioritizes August and September as critical months when rail temperatures reach their highest values, a characterization supported by both measured data and the hybrid approach simulation outcomes discussed in Sections 5.1.2 and 5.2.2. Finally, additional synthetic days were generated focusing to increase the dataset density in the region around $40\,^{\circ}$C, thereby improving probability estimation accuracy in this domain. In total, $3\,300\,000$ simulations were performed, requiring approximately 28 hours to complete.

Table 12 – Summary of Monte Carlo simulations scenarios generation

	Ago, Set	**Others**
# Months	2	4
Generated days	3000	1500
Monte Carlo variations	500	50
Subtotal input files	6000	6000
Subtotal # simulations	3 000 000	300 000

Source: Author (2026)

- Bin analysis

Figure 41 presents a bin analysis, as described by Equation 26. For example, at $35\,^{\circ}$C, the probability of rail temperature reaching or exceeding $52\,^{\circ}$C is $10\,\%$ for simulations in which the maximum T_{air} falls between $34\,^{\circ}$C to $36\,^{\circ}$C. This analysis addresses the question: *"For a specific ambient temperature intensity range, what is the probability of rail temperature exceeding critical thresholds?"*.

Comparing with the field-measured weather data analysis (Fig. 34) reveals a notable difference in the ambient temperature axis: the hybrid approach terminates at $41\,^{\circ}$C due to insufficient collected data at higher temperature ranges, whereas the synthetic approach extends beyond $45\,^{\circ}$C through synthetic scenario generation.

Significant differences also emerge in probability responses. For instance, the synthetic approach do not exhibit the sudden drops in the P55 curve, for ambient air temperatures in the range $34\,^{\circ}$C to $35\,^{\circ}$C. This happens due to the fact that now, the amount of simulations is increased, which might yield a more robust fragility estimation for the given intensity intervals.

Initially, for $T_{\text{air}} \geq 42\,^{\circ}$C, probability fluctuations similar to those in the hybrid approach occurred (see Fig. 34), characterized by sudden drops. This behavior arises from an insufficient number of scenarios satisfying the filter criteria. The issue was addressed by generating additional synthetic scenarios constrained to higher maximum ambient air temperatures in this range, as mentioned previously. This refinement enabled smoother probability curves and im-

Figure 41 – Fragility curves for synthetic Monte Carlo approach

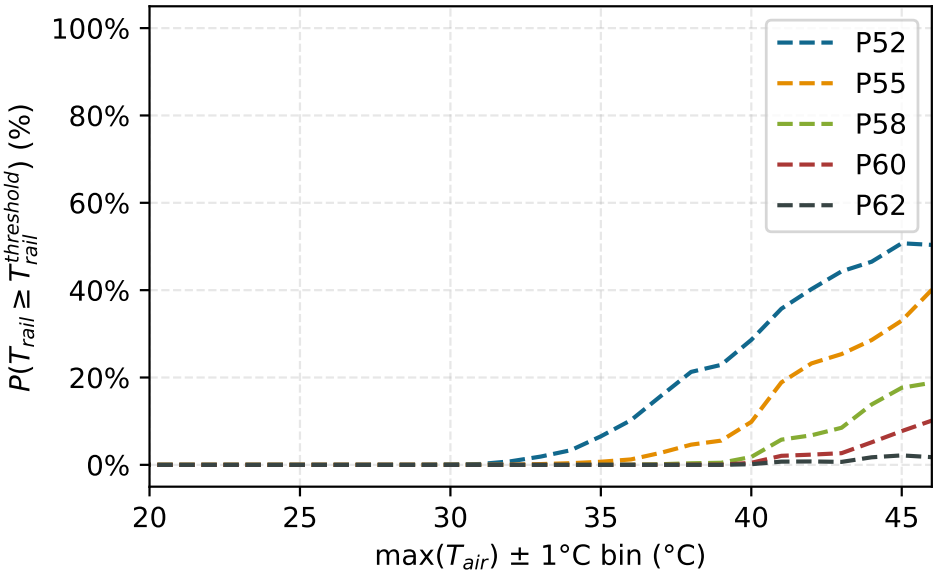

Source: Author (2026)

proved estimation accuracy. Figure 42 illustrates the distribution of simulation counts matching each ambient air temperature bin.

Additionally, Figure 43 shows the distribution of simulations based on their maximum ambient air temperature bin. This demonstrates that the majority of scenarios are concentrated around $30\,^{\circ}$C, with skewness toward the lower bound around $5\,^{\circ}$C and a maximum of $48\,^{\circ}$C in the upper bound. Such high temperatures may not be realistic at present but could be relevant when analyzing climate change scenarios. This topic is discussed further in Section 6.

Figure 42 – Daily aggregated distribution of maximum simulated rail temperatures (T_{rail}) for different ambient temperature (T_{air}) intensity

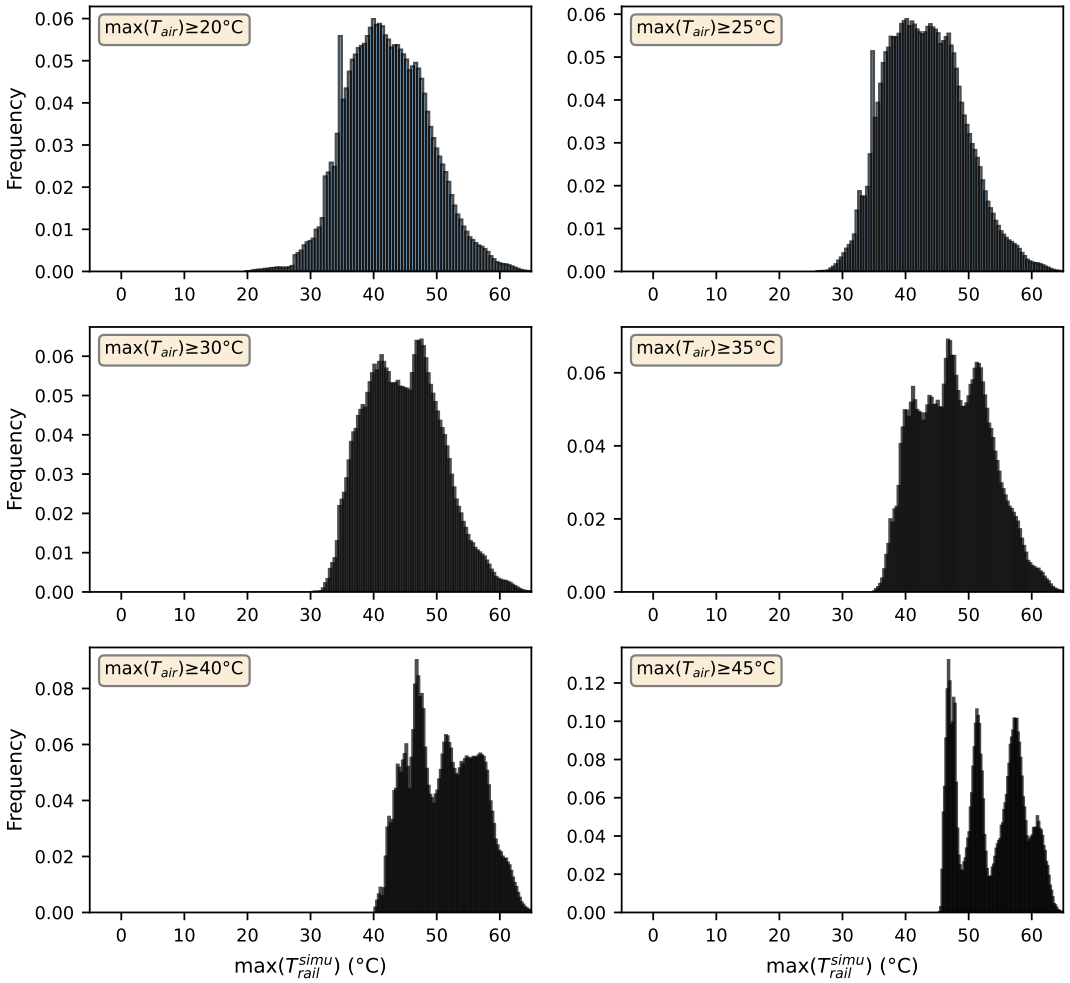

Source: Author (2026)

Figure 43 – Count of simulations for given T_{air} bins

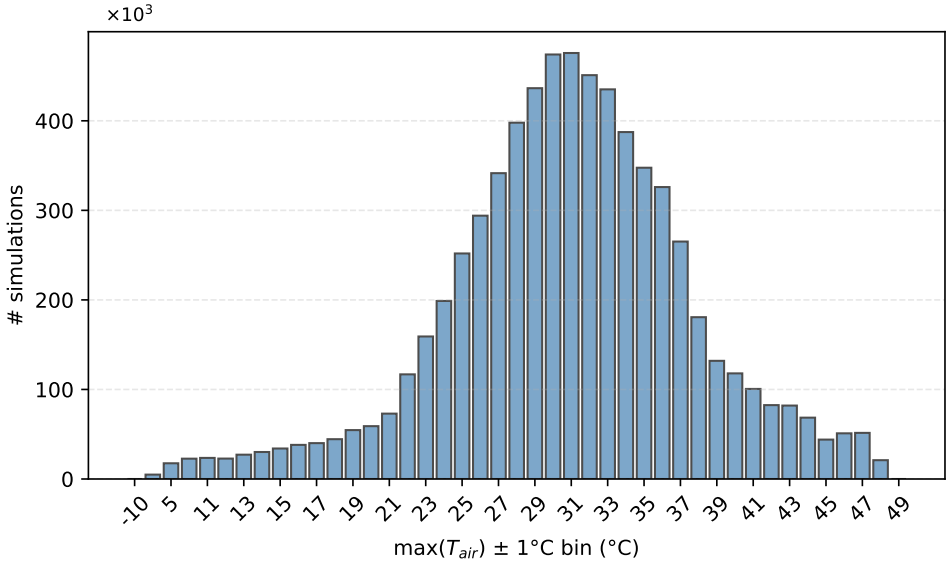

Source: Author (2026)

- Extra analysis

Figure 44 presents a sample of simulated and measured rail temperatures for August. The figure demonstrates scenario variability under similar initial conditions and confirms that the model exhibits faster cooling rates than measured values, consistent with the behavior observed in the hybrid approach (Fig. 36). Additionally, the figure illustrates the substantial spread in simulated values resulting from parameter and weather scenario variations.

Figure 44 – Time series example of measured and scenario variations of simulated rail temperatures

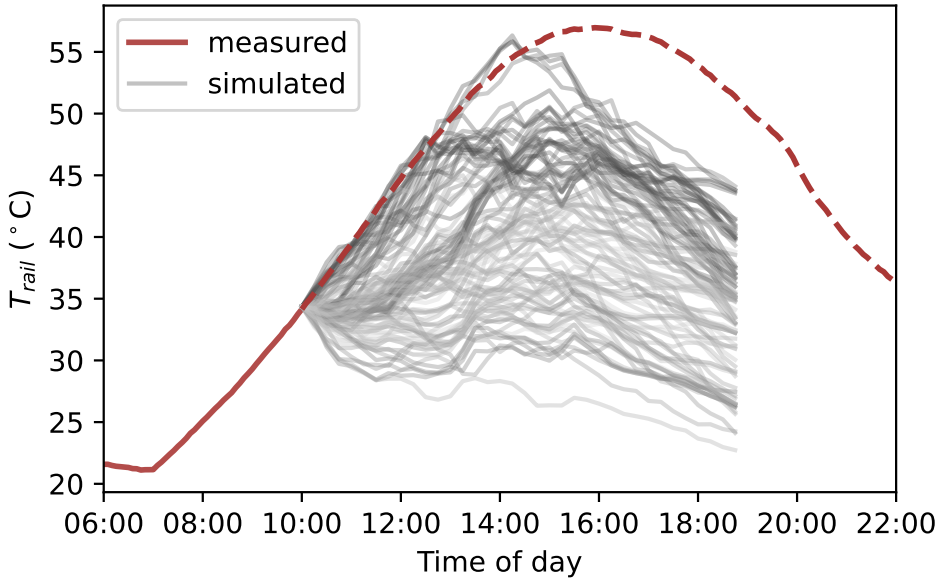

Source: Author (2026)

It is also worth analyzing the behavior of the simulations across months, since the generated scenarios differentiate between them. Figure 45 shows the spread of the generated ambient air temperatures and the simulated rail temperatures for all simulated months. Among the simulated months, only August and September exceed $60\,°\text{C}$, which are in fact the critical months. It is worth mentioning that the existing data for July was merged with August when fitting models for synthetic generation, as explained in Section 5.2.3. This suggests that, for a buckling analysis, it is worthwhile to concentrate efforts only on critical months, since other months will have virtually null risk of reaching critical temperatures.

In summary, the hybrid and synthetic approaches yield substantially different probability estimates. The hybrid approach, constrained by limited measured data (192 days, $96\,000$ simulations), produces higher probabilities at extreme temperature thresholds, while the synthetic approach ($3\,300\,000$ simulations) provides more conservative estimates through broader scenario coverage. For the synthetic approach, at $40\,°\text{C}$ ambient temperature, the probabilities of rail temperature reaching or exceeding $55\,°\text{C}$ (*P55*) and $60\,°\text{C}$ (*P60*) are $10\,\%$ and $0.6\,\%$, respectively. In contrast, the hybrid approach yields probabilities of $51\,\%$ and approximately $0.6\,\%$ for the same temperature thresholds, reflecting the limited range of extreme weather scenarios in the measured dataset.

Figure 45 – Boxplot of simulated and measured air and rail temperatures

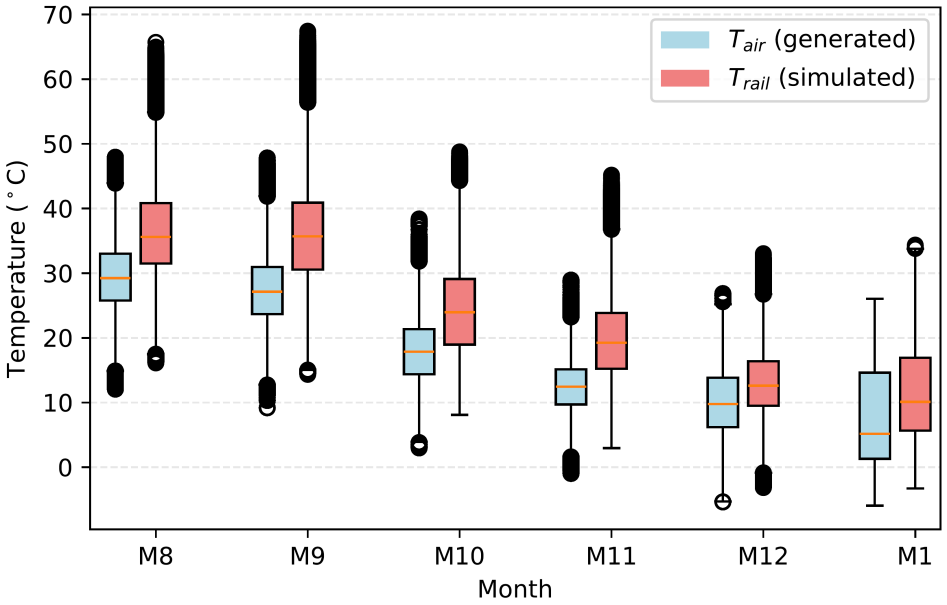

Source: Author (2026)

The synthetic approach extends the analysis beyond $45\,^{\circ}\mathrm{C}$ ambient temperature (compared to the $40\,^{\circ}\mathrm{C}$ limit in the hybrid approach), enabling probability estimation for extreme conditions not present in the historical record. Among the simulated months, only August and September exhibit rail temperatures exceeding $60\,^{\circ}\mathrm{C}$, identifying them as critical months for buckling risk assessment. This suggests that thermal analysis efforts should concentrate on these months, as others present virtually null risk of reaching critical temperatures.

Both approaches confirm that the model exhibits faster cooling rates compared to field measurements, although peak temperature predictions remain accurate. This behavior, also observed by Piloto *et al.* (2022), validates the model's adequacy for threshold exceedance analysis despite minor temporal evolution discrepancies. Temporal analysis of simulation runs (Figures 44 and 36) reveals substantially greater variability in the synthetic approach due to simultaneous variation of both weather scenarios and model parameters, whereas the hybrid approach exhibits narrower variation around the measured values.

Finally, the distributed computing framework (*Ray*) successfully enabled the execution of $3\,300\,000$ simulations within approximately 28 hours using a cloud-based cluster configuration, demonstrating the computational feasibility of large-scale probabilistic rail temperature analysis.

6 CONCLUSION AND FUTURE WORKS

This work successfully accomplished its objectives of characterizing the probability distribution of railway temperatures under diverse weather conditions and quantifying the influence of input parameters on rail temperature predictions. Through systematic sensitivity analysis and extensive Monte Carlo simulations, the present work provides valuable insights for thermal-related risk assessment in railway tracks.

The sensitivity analysis, conducted using Sobol indices and Morris methods, identified the most influential parameters affecting rail temperature predictions. When all parameters are treated as random variables, the convection coefficient, ambient temperature, and solar radiation emerge as the dominant factors. However, in scenarios where weather parameters can be reliably measured, the solar absorption coefficient and solar absorption area become the critical parameters requiring careful characterization. Material properties such as density, specific heat, and volume demonstrate negligible influence on model predictions.

The fragility curves calculated with Monte Carlo simulation, comprising over 3.3 million scenarios executed using distributed computing with the Ray framework, enabled comprehensive probabilistic analysis extending beyond historically observed conditions. The synthetic weather generation approach successfully addresses the limitations of the hybrid method by enabling probability estimation for extreme temperature events not present in the 192-day measured dataset. The analysis identifies August and September as critical months when rail temperatures exceed $60\,^{\circ}$C, suggesting that thermal buckling risk assessments should concentrate efforts on these periods.

Key probabilistic findings reveal substantial differences between hybrid and synthetic approaches. At $40\,^{\circ}$C ambient temperature, the synthetic approach estimates $10\,\%$ and $0.6\,\%$ probabilities for rail temperatures reaching or exceeding $55\,^{\circ}$C and $60\,^{\circ}$C, respectively, while the hybrid approach yields $51\,\%$ and approximately $0.6\,\%$. These discrepancies underscore the importance of comprehensive scenario coverage for robust probability estimation.

Despite these achievements, the synthetic weather generation approach treats meteorological parameters as independent variables, whereas in reality they exhibit mutual dependencies (e.g., solar radiation correlates with ambient temperature, wind speed influences convection). This simplification may affect the realism of generated extreme weather scenarios and consequently impact probability estimates. Additionally, the limited temporal span of the measured dataset (192 days) constrains the statistical robustness of the distribution fitting process. Future work incorporating multivariate weather generation models and extended measurement campaigns would address these limitations.

6.1 Future Works

Based on the findings and limitations of this research, the following topics worth exploring on future works.

- **Climate change scenarios**: Investigating rail temperature behavior under projected climate change scenarios, particularly for ambient temperatures exceeding $45\,^{\circ}\mathrm{C}$, would provide valuable insights for long-term infrastructure planning and adaptation strategies;
- **Improved synthetic scenario generation**: To address the limitation that weather parameters do not interact with each other, an improved approach for synthetic scenario generation incorporating multivariate dependencies would enhance calculation accuracy and reduce the observed variability;
- **Enhanced convection coefficient modeling**: Given that the convection coefficient emerges as the most influential parameter in the all-parameters scenario, and it is itself a sub-model, refining its estimation through improved empirical correlations or computational fluid dynamics modeling could substantially enhance prediction accuracy;
- **Extended temporal coverage with additional field measurements**: Expanding the measured dataset to encompass a full annual cycle across multiple years would improve statistical robustness of distribution fitting and might reduce the differences in the probability curves calculated using synthetic and measured data.

BIBLIOGRAPHY

American Railway Engineering and Maintenance-of-way Association. **Manual for Railway Engineering**. USA: [*s.n.*], 2010. v. 1 - Track.

BIROLINI, A. **Reliability Engineering: Theory and Practice**. 3 rd ed. ed. Berlin: Springer, 1999. ISBN 978-3-540-66385-0.

BONNETT, C. F. **Practical Railway Engineering**. 2. ed. ed. [*S.l.*]: Imperial College Press, 2005. ISBN 1-86094-515-5.

BORGONOVO, E.; PLISCHKE, E. Sensitivity analysis: A review of recent advances. **European Journal of Operational Research**, v. 248,n. 3,p. 869–887,fev. 2016. ISSN 0377-2217.

BOSSE, R. M. **Curvas de Fragilidade e Modelos de Colapso Baseados Em Dano Para Pórticos de Concreto Armado Sujeitos à Ação Sísmica**. 2022. Tese (Doutorado) — USP São Carlos, Brazil 2022.

BRANCO, J. E. S. C. **A Segregação Da Infra-Estrutura Como Elemento Reestruturador Do Sistema Ferroviário Brasileiro**. 2008. Tese (Doutorado) — UFRJ/COPPE 2008.

CANNAVÓ, F. Sensitivity analysis for volcanic source modeling quality assessment and model selection. **Computers & Geosciences**, v. 44,p. 52–59,jul. 2012. ISSN 0098-3004.

CARVALHO, J. F. C. V. de. Estabilidade estrutural da via ferroviária, 2010.

CHAPMAN, L. *et al.* Modelling of rail surface temperatures: A preliminary study. **Theoretical and Applied Climatology**, Springer Wien v. 92,n. 1-2,p. 121–131,2008. ISSN 14344483.

Directorate-General for Mobility and Transport. **EU Transport in Figures : Statistical Pocketbook 2019**. [*S.l.*]: Office for Official Publications of the European Communities, 2019. ISBN 978-92-76-03843-6 978-92-76-03842-9.

DITLEVSEN, O. D.; MADSEN, H. O. **Structural Reliability Methods**. 1. ed. Chichester New York Brisbane [etc.]: J. Wiley & sons, 1996. ISBN 978-0-471-96086-7.

ESVELD, C. **Modern Railway Track**. 2. ed. ed. Zaltbommel: MRT-Productions, 2001. ISBN 90-800324-3-3.

FORTUNATO, E. M. C. **Renovação de plataformas ferroviárias : estudos relativos à capacidade de carga**. 2005. Tese (Doutorado) 2005.

FRIGERI, A. V. N. **Thermal and Mechanical Behavior of Railway Tracks**. 2021. Tese (M.S. Thesis) — Polytechnic Institute of Bragança Bragança 2021.

GROENENDAAL, W. J. V.; KLEIJNEN, J. P. Deterministic versus stochastic sensitivity analysis in investment problems: An environmental case study. **European Journal of Operational Research**, v. 141,n. 1,p. 8–20,ago. 2002. ISSN 03772217.

GÜNAY, S.; MOSALAM, K. M. PEER Performance-Based Earthquake Engineering Methodology, Revisited. **Journal of Earthquake Engineering**, v. 17,n. 6,p. 829–858,ago. 2013. ISSN 1363-2469, 1559-808X.

HALLBERG, M. **Railroads in North America**. [*S.l.*]: 2009.

HONG, S. U. *et al.* Prediction of a representative point for rail temperature measurement by considering longitudinal deformation. **Proceedings of the Institution of Mechanical**

Engineers, Part F: Journal of Rail and Rapid Transit, SAGE Publications Ltd v. 233,n. 10,p. 1003–1011,nov. 2019. ISSN 20413017.

HONG, S. U. *et al.* A Rail-Temperature-Prediction Model Considering Meteorological Conditions and the Position of the Sun. **International Journal of Precision Engineering and Manufacturing**, SpringerOpen v. 20,n. 3,p. 337–346,mar. 2019. ISSN 20054602.

HUNT, GA. **An Analysis of Track Buckling Risk**. [*S.l.*], 1994.

IANTAS, G. B. **Estudo da confiabilidade estrutural de sapatas submetidas a cargas centradas dimensionadas pelo CEB-70**. jun. 2021. Tese (Doutorado) — Universidade Tecnológica Federal do Paraná jun. 2021.

Joint Commitee On Structural Safety. **Probabilistic Model Code Part 2: Load Models**. [*S.l.*]: 2001.

KAUFMANN, A.; GROUCHKO, D.; CRUON, R. (Ed.). **Mathematical Models for the Study of the Reliability of Systems**. New York: Academic Press, 2010. (Mathematics in Science and Engineering, v. 124). ISBN 978-0-12-402370-3 978-0-08-095633-6.

KERR, A. D. Analysis of thermal track buckling in the lateral plane. **Acta Mechanica**, v. 30,n. 1-2,p. 17–50,mar. 1978. ISSN 0001-5970, 1619-6937.

Kevin Kesler and Yu-Jiang Zhang. **System and Method for Predicting Future Rail Temperature**. 2007. US 20070265780A1.

KISH, A.; SAMAVEDAM, G. **Track Buckling Prevention: Theory, Safety Concepts, and Applications Track Systems Safety**. Cambridge: , 2013. 168 p.

LEITE, M. R. S. V. D. **Especificações Técnicas da Via-Férrea**. 2017. Tese (M.S. thesis) 2017.

LEWIS, M. Railway in the greek and roman world, 2001.

LICHTE, U. **Klimatische Temperatureinwirkungen Und Kombinationsregeln Bei Brückenbauwerken**. 2004. Tese (Doutorado) — Universiät der Bundeswehr München 2004.

LIM, N.-H.; PARK, N.-H.; KANG, Y.-J. Stability of continuous welded rail track. **Computers & Structures**, v. 81,n. 22,p. 2219–2236,set. 2003. ISSN 0045-7949.

MARELLI, S. *et al.* **UQLab User Manual – Sensitivity Analysis**. Switzerland: , 2022.

MARMASH, B.; RYAN, M. **Management of Stressed Continuously Welded Track. Rail Stress Free Temperature Measurement Techniques (T359 Report)**. UK: , 2006.

MELCHERS, R. E.; BECK, A. T. **Structural Reliability Analysis and Prediction**. Third edition. Hoboken, NJ: John Wiley & Sons Ltd, 2018. (Engineering Professional Collection). ISBN 978-1-119-26610-5 978-1-119-26607-5.

MICHALSKY, J. The Astronomical Almanac's algorithm for approximate solar position (1950–2050). **Solar Energy**, v. 40,p. 227–235,dez. 1988.

MORALES, M. S. T. **ANÁLISE DE CONFIABILIDADE DE TALUDES EM CONDIÇÕES SATURADAS-NÃO SATURADAS VIA ANÁLISE LIMITE NO ESPAÇO CÔNICO QUADRÁTICO**. set. 2013. Tese (DOUTOR EM CIÊNCIAS DE ENGENHARIA CIVIL) — PONTIFÍCIA UNIVERSIDADE CATÓLICA DO RIO DE JANEIRO Rio de Janeiro, Brazil set. 2013.

MOREIRA, A. S. C. **Métodos de dimensionamento de vias-férreas**. 2014. Tese (M.S. thesis) 2014.

MORITZ, P. *et al.* Ray: A Distributed Framework for Emerging AI Applications. *In*: 13TH USENIX Symposium ON Operating Systems Design AND Implementation (OSDI 18). 2018. [*S.l.*: *s.n.*], 2018. p. 561–577. ISBN 978-1-939133-08-3.

MORRIS, M. D. Factorial sampling plans for preliminary computational experiments. **Technometrics**, v. 33,n. 2,p. 161–174,1991. ISSN 0040-1706.

MUNRO, P. **Management of Track Infrastructure in Hot Weather: A Practical Application**. [*S.l.*]: 2009.

PANDROL. **Wikipedia**, mar. 2020.

PILOTO, P. A. *et al.* Validation of a rail temperature model with experimental measurements. **Proceedings of the Institution of Mechanical Engineers, Part F: Journal of Rail and Rapid Transit**, v. 236,n. 9,p. 095440972210747,fev. 2022. ISSN 0954-4097, 2041-3017.

PILOTO, P. A. G.; FRIGERI, A. V. N.; MINHOTO, M. Thermal Buckling of Railways. **ce/papers**, v. 5,n. 2,p. 31–40,2022. ISSN 2509-7075.

PROFILLIDIS, V. **Railway Management and Engineering**. 4th edition. ed. Farnham, Surrey, England: Routledge, 2016. ISBN 978-1-4094-6463-1.

Salazar-Peña, N.; TABARES, A.; González-Mancera, A. Sequential stochastic and bootstrap methods to generate synthetic solar irradiance time series of high temporal resolution based on historical observations. **Solar Energy**, v. 264,p. 112030,nov. 2023. ISSN 0038-092X.

SALTELLI, A. (Ed.). **Sensitivity Analysis in Practice: A Guide to Assessing Scientific Models**. Reprinted. Chichester Weinheim: Wiley, 2007. ISBN 978-0-470-87093-8.

SALTELLI, A. *et al.* **Global Sensitivity Analysis: The Primer**. [*S.l.*]: John Wiley, 2008. ISBN 978-0-470-05997-5.

SAMAVEDAM, G. *et al.* **Parametric Analysis and Safety Concepts of CWR Track Buckling**. Springfield, VA 22161: , 1993. 120 p.

SciPy 1.0 Contributors *et al.* SciPy 1.0: Fundamental algorithms for scientific computing in Python. **Nature Methods**, v. 17,n. 3,p. 261–272,mar. 2020. ISSN 1548-7091, 1548-7105.

SOBOL, I. M. **A Primer for the Monte Carlo Method**. Boca Raton: CRC Press, 1994. ISBN 978-1-315-13644-8.

SOBOL′, I. M. Global sensitivity indices for nonlinear mathematical models and their Monte Carlo estimates. **Mathematics and Computers in Simulation**, v. 55,n. 1,p. 271–280,fev. 2001. ISSN 0378-4754.

THORNES, J. E. **The Prediction of Ice Formation on Motorways in Britain**. 1984. Tese (Doctoral) — University of London 1984.

TORII, A. J. *et al.* Global sensitivity analysis for mathematical models comparison. **Computational and Applied Mathematics**, v. 42,n. 8,p. 345,dez. 2023. ISSN 2238-3603, 1807-0302.

VAN, M. A. Buckling analysis of continuous welded rail track. **Heron**, v. 41,n. 3,p. 175–186,1996.

WU, Y. *et al.* A Review on Recent Developments in Rail Temperature Prediction for use in Buckling Studies. *In*: CONFERENCE ON Railway Engineering. 2010, Wellington. Wellington: [*s.n.*], 2010.

ZHANG, Y.-J.; LEE, S. Modeling Rail Temperature with Real-Time Weather Data. *In*: TRANSPORTATION Research Circular. 2008–Nineteenth century, Indianapolis, Indiana. Indianapolis, Indiana: [*s.n.*], 2008–Nineteenth century. ISSN 0097-8515.

APPENDIX A – Code Examples

A.1 Example of *railtemp* monte carlo simulation

Source Code 2 – Example of monte carlo simulation using *railtemp* package

```
# create Rail and Material objects
def create_rail_object_variable() -> Rail:
    # Random parameters
    SolarAbsD = BetaParameterValue(alpha=5, beta=2)
    ConvectionAreaD = ClippedNormalParameterValue(
        mean=0.43046, std=0.05, low=0, high=0.43046
    )
    RadiationAreaD = ClippedNormalParameterValue(
        mean=0.43046, std=0.05, low=0, high=0.43046
    )
    RailEmiss = BetaParameterValue(alpha=14.7, beta=6.3)
    AmbientEmiss = BetaParameterValue(alpha=14.4, beta=9.6)
    DensityD = NormalParameterValue(mean=7850, std=78.5).set_mode(
        RandomParameterMode.VARIABLE
    )
    VolumeD = NormalParameterValue(mean=7.16e-3, std=0.0716e-3)

    steel = RailMaterial(
        density=DensityD,
        solar_absort=SolarAbsD,
        emissivity=RailEmiss,
        specific_heat=SpecificHeatWrapper().get,
    )

    rail = Rail(
        name="UIC54",
        azimuth=93,
        lat=41.482628,
        long=-7.183741,
        elev=220,
        cross_area=VolumeD,
        convection_area=ConvectionAreaD,
        radiation_area=RadiationAreaD,
        ambient_emissivity=AmbientEmiss,
        material=steel,
    )
    return rail

# Create and run montecarlo simulation
rail_model_variable: Rail = create_rail_object_variable()
weather_file_list: List[str] = ["input1.csv","input2.csv","input3.csv" ]


mt_carlo = Montecarlo(
    rail_object=rail_model_variable,
    weather_input_list=weather_file_list,
    num_variations=100,
    name=f"montecarlo-example",
)
# prepare the simulation run objects
simu_objs = mt_carlo.generate_simulation_objects()

# start simulation in sequence
[sr.run() for sr in simu_objs]
```

Source: Author (2026)

APPENDIX B – Complementary plots

B.1 Synthetic weather data generation

Figure 46 – Generated and measured ambient temperature distribution by month

(a) August

(b) September

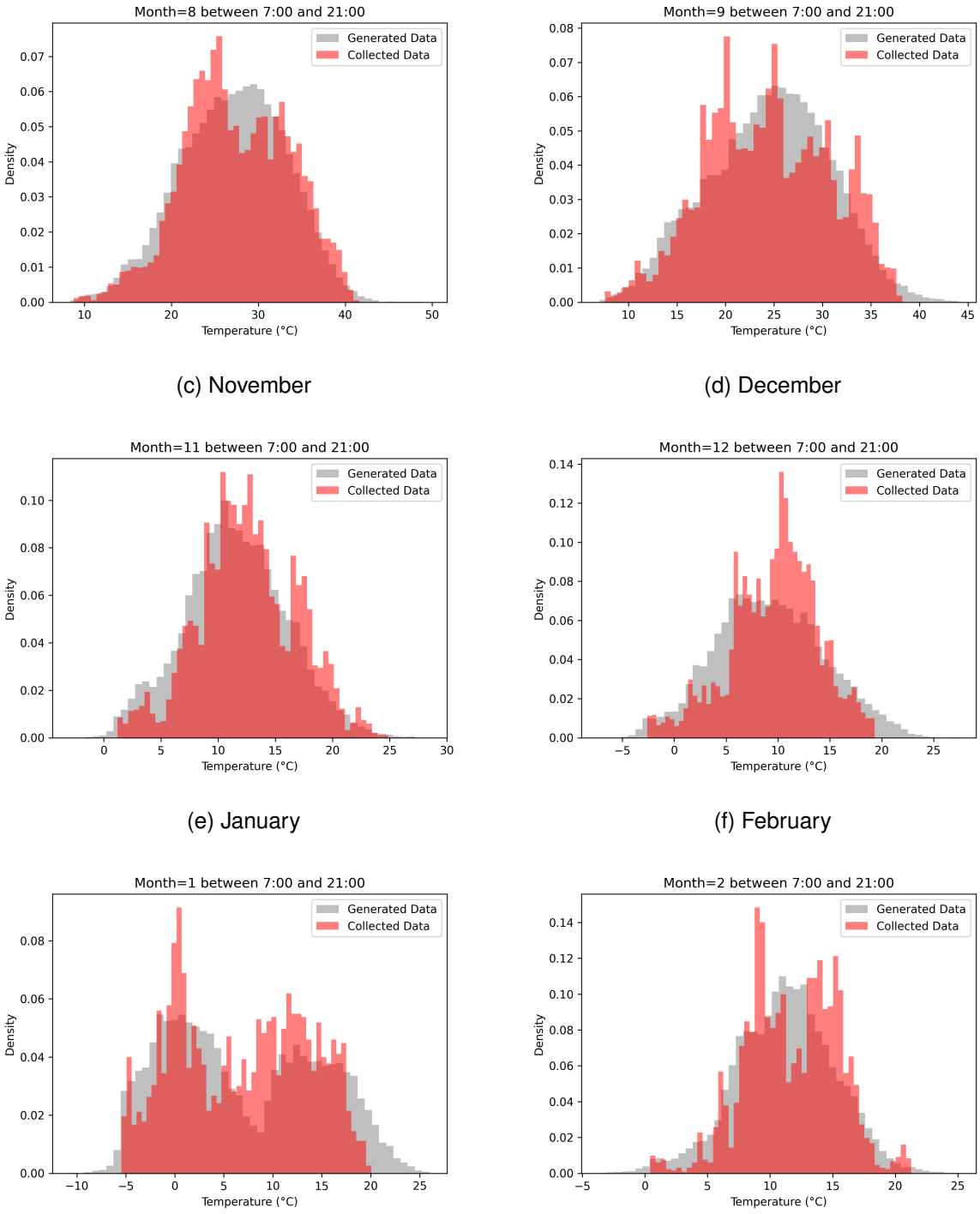

(c) November

(d) December

(e) January

(f) February

Source: Author (2026)

Figure 47 – Generated and measured wind speed distribution by month

(a) August

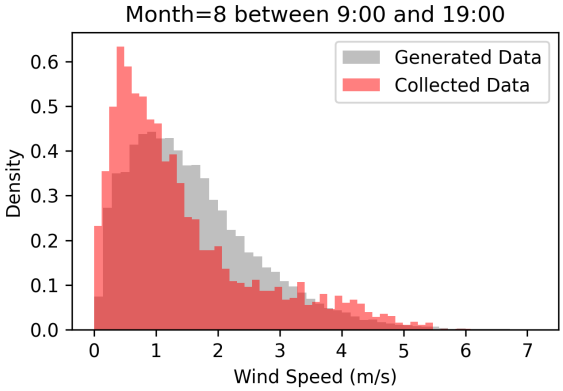

(b) September

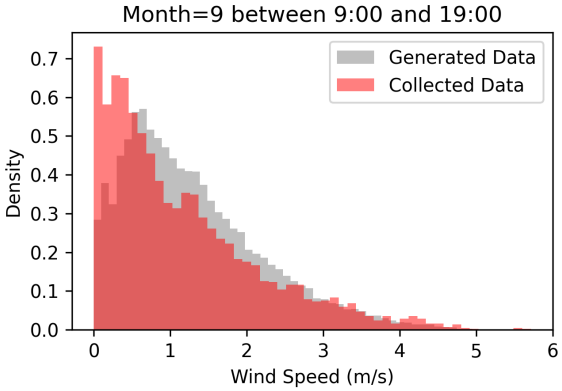

(c) November

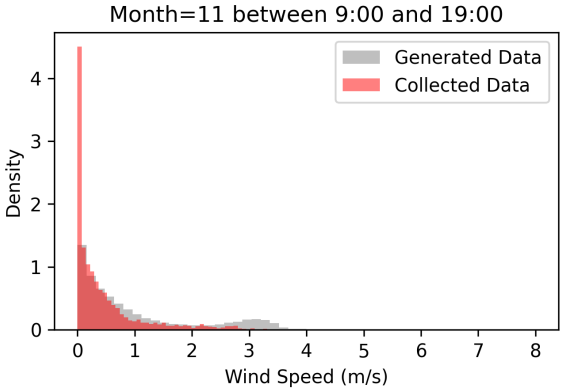

(d) December

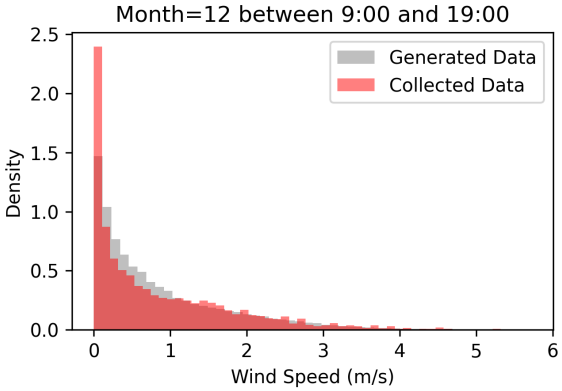

(e) January

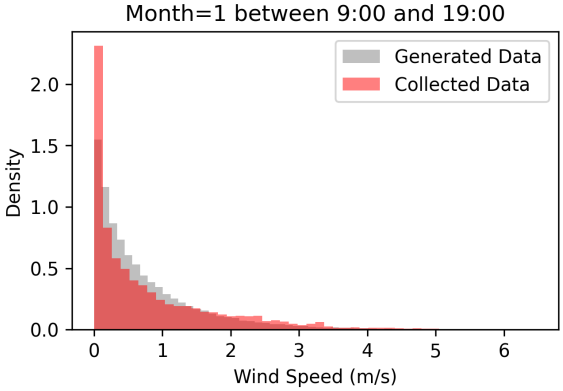

(f) February

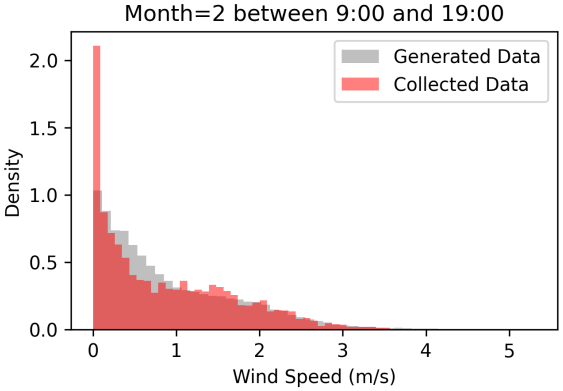

Source: Author (2026)

Figure 48 – Generated and measured solar radiation distribution by month

(a) August

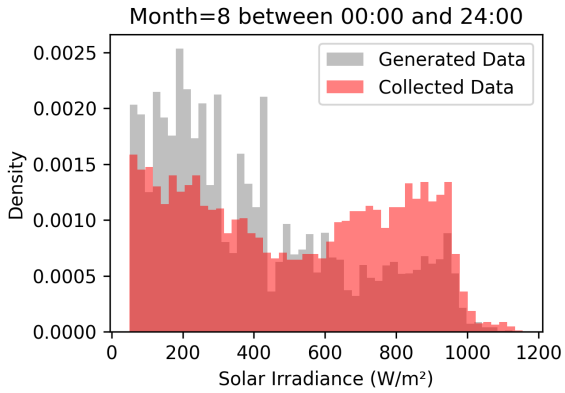

(b) September

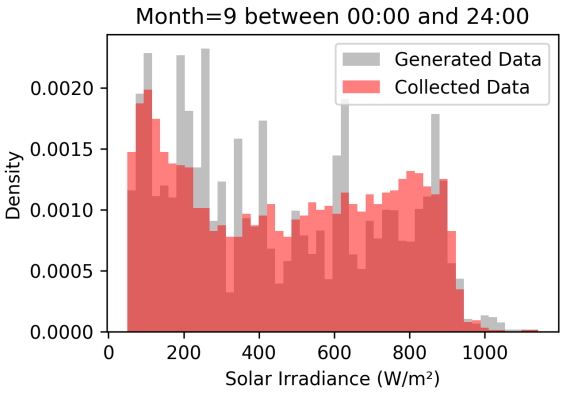

(c) November

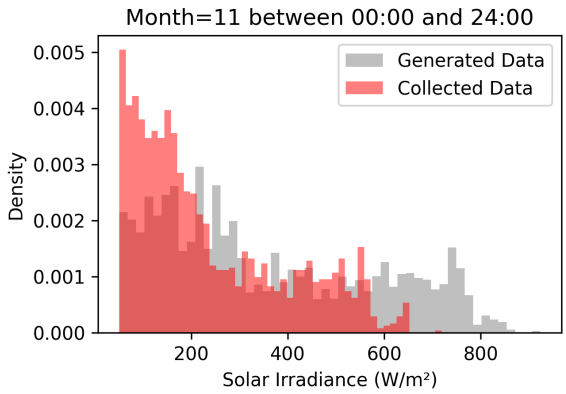

(d) December

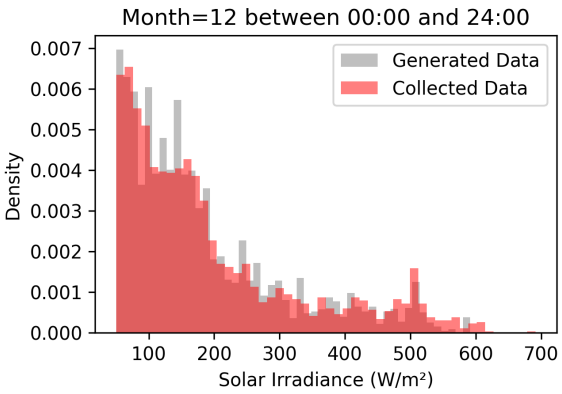

(e) January

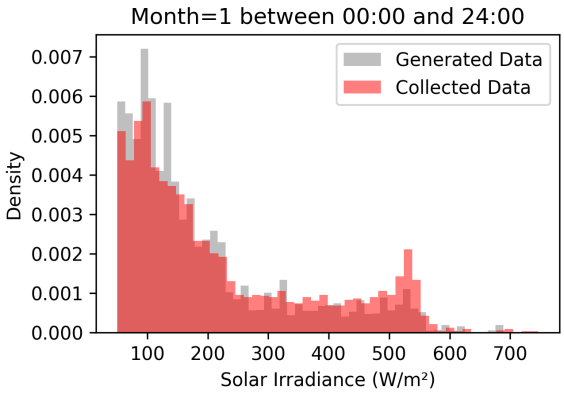

(f) February

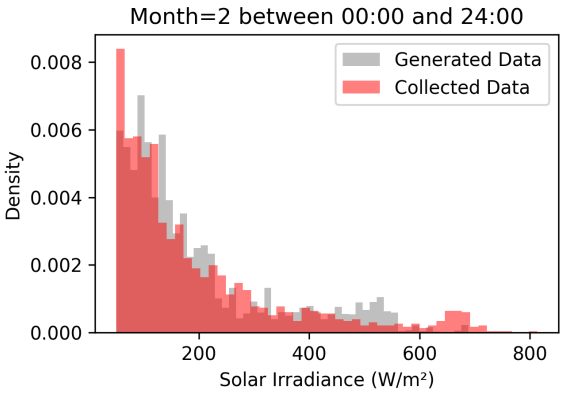

Source: Author (2026)

Figure 49 – Boxplot of the generated and measured data for ambient temperature by month and 15-min intervals

(a) August

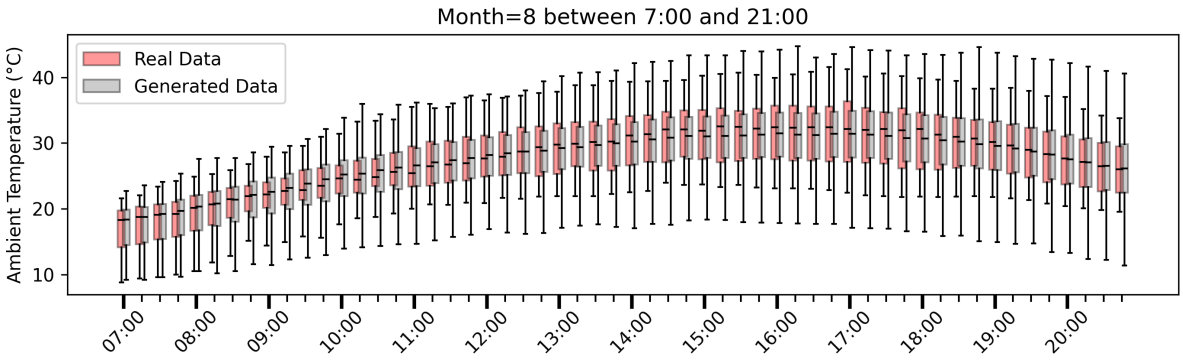

(b) September

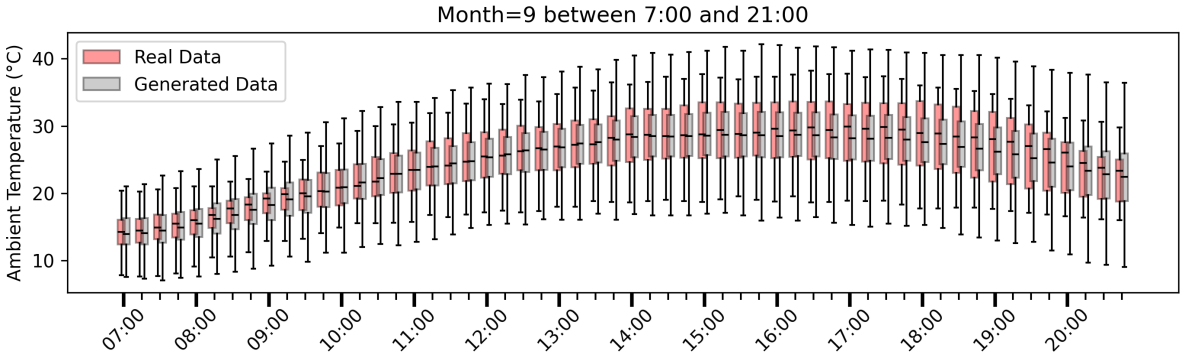

(c) November

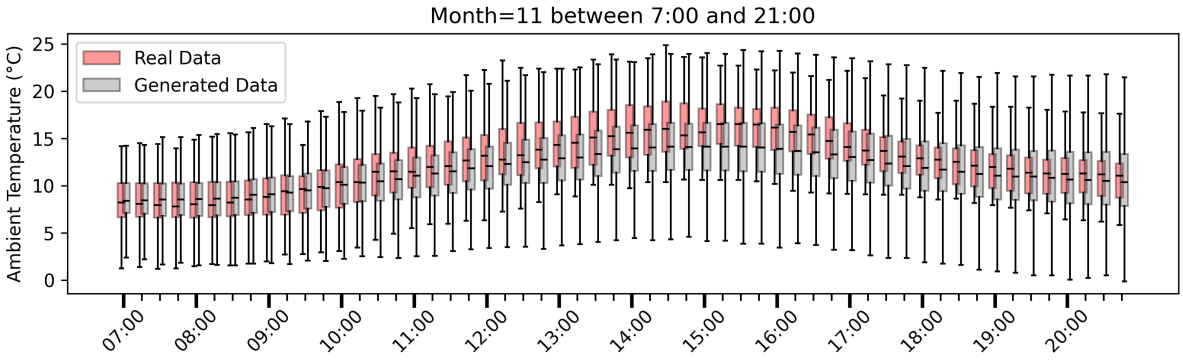

(d) December

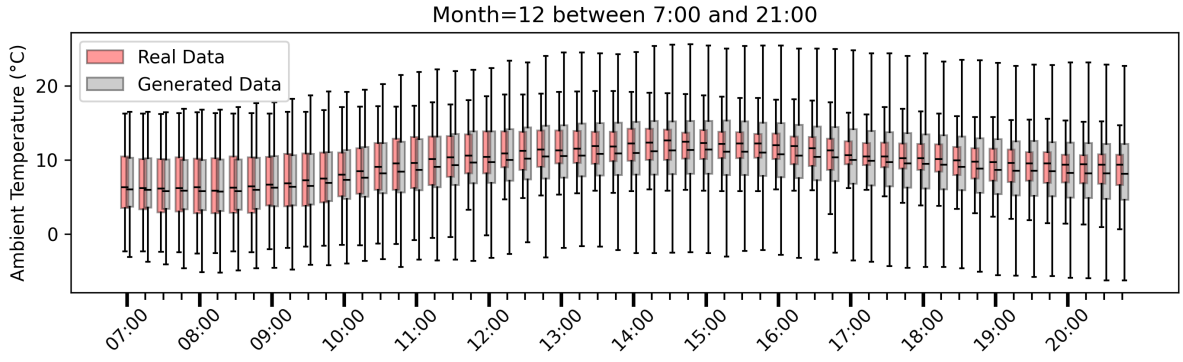

Source: Author (2026)

Figure 49 – Boxplot of the generated and measured data for ambient temperature by month and 15-min intervals (continued)

(e) January

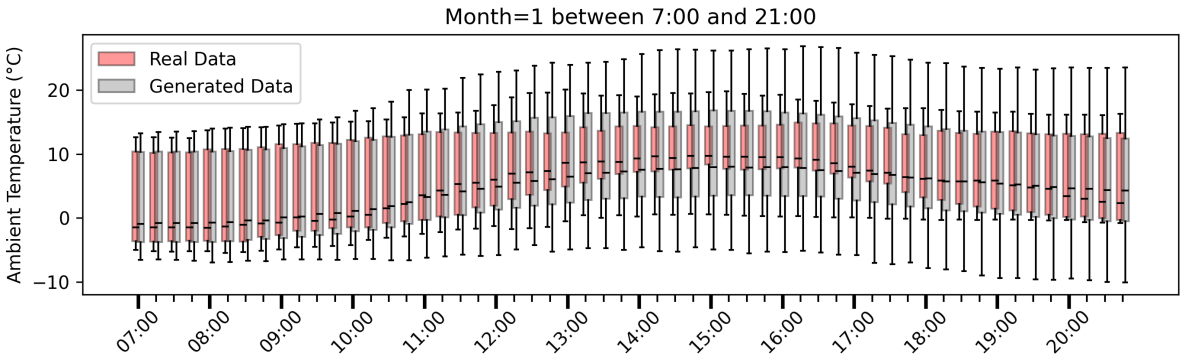

(f) February

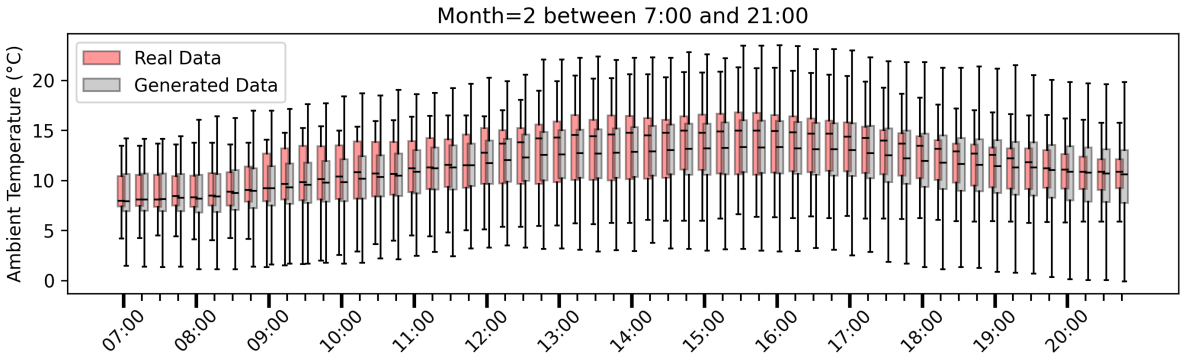

Source: Author (2026)